CONFOCAL MICROSCOPY OF FLUID ARGON UNDER PRESSURE

By

GABRIEL JOSEPH HANNA

A dissertation submitted in partial fulfillment
of the requirements for the degree of

DOCTOR OF PHILOSOPHY

WASHINGTON STATE UNIVERSITY
Department of Physics and Astronomy

DECEMBER 2009

To the Faculty of Washington State University:

The members of the Committee appointed to examine the dissertation of GABRIEL JOSEPH HANNA find it satisfactory and recommend that it be accepted.

Matthew D. McCluskey, Ph.D., Chair

Yogendra M. Gupta, Ph.D.

Choong-Shik Yoo, Ph.D.

CONFOCAL MICROSCOPY OF FLUID ARGON UNDER PRESSURE

Abstract

by Gabriel Joseph Hanna, Ph.D.
Washington State University
December 2009

Chair: Matthew D. McCluskey

Confocal microscopy is a technique used in mainly in the life sciences for producing three-dimensional images of cellular structures. We have adapted the technique to measure volumes and refractive indices of fluids in a diamond anvil cell. While high-precision techniques, such as X-ray diffraction and neutron scattering, exist for measuring lattice volumes of solids, the measurement of fluid volumes is much more difficult. This new technique will allow for quick, inexpensive, and non-destructive measurements of the equation of state of fluids at high pressure. In addition, we have explored the use of carbon dioxide as a probe of the structure of fluid argon and nitrogen, using Fourier transform infrared spectroscopy. New experimental results presented here include: procedures for measuring volume and refractive index with the confocal microscope; the equation of state and refractive index of argon water along the 300 K isotherm up to about 5 GPa; the dependence on density and pressure of the asymmetric stretching mode of carbon dioxide dissolved in argon and nitrogen at 300 K; and the IR absorption frequency of Ge:O as a function of pressure at 10 K.

Dedication

To my beloved wife, Jing Jing Wang, this dissertation is affectionately dedicated.

Who can find a virtuous woman? for her price is far above rubies.

Acknowledgement

First, my parents, Andrea Green and Glenn Hanna; and Margaret and Roger Catlow, who are also my parents. Whatever is good in my character they instilled in me, and whatever is bad, they didn't put it there.

My sisters, Autumn, Sara, and Jessica. We are, as far as I know, the only four people for whom the subject of pigs eating people is appropriate Christmas Eve conversation. My stepfather, Jim Green, who introduced me to sailing.

My extended family of Benjamins, Risleys and Friesens, which currently consists of five living generations. It is a wonderful thing to have people to belong to; especially such smart and fun people as they are. Ronnie Crum, in particular, whose eyes never glaze over when I talk about physics.

Doerte Blume, Fred Gittes, Mark Kuzyk, and Mike Miller are the best instructors I have ever had. If I know anything about physics, I learned it from them; and from Steve Tomsovic, who helped me at a very critical time when I needed it most.

Matt McCluskey and Doerte Blume taught me how to be a working scientist, which is quite different from being a student. They also supplied encouragement, second thoughts, and beer.

Slade Jokela and Bobbie Riley taught me almost everything I know about diamond anvil cells and FTIR spectroscopy.

My committee, Matt McCluskey, Yogendra Gupta, and Choong-Shik Yoo, for their time and trouble in reviewing this manuscript; and the Institute of Shock Physics, for provding me with support.

My dear wife, Jing Jing Wang. There is not space here to give her the credit she deserves; but I have the rest of my life in which to try.

Financial support for this work was provided by the Department of Energy and

NSF.

Contents

List of Figures

List of Tables

Chapter 1

Introduction

1.1 History of argon

1.1.1 Discovery

In 1894, Lord Rayleigh noticed that nitrogen produced from chemical reactions seemed to be less massive than nitrogen gas extracted from the atmosphere. The difference was small, less than one-half of one percent, but the precision of the experiments implied that the difference was significant, and unexplained [1].

Impurities in atmospheric nitrogen were suspected, but all known elements were eliminated by one test or another, and in 1895 Lord Rayleigh and William Ramsay [2] presented to the Royal Society their evidence of a new atmospheric component. They isolated it from nitrogen by several methods, and found that it would react with no known substance. They called it *argon*, which is Greek for "it does no work."

In recreating the experiments of Henry Cavendish in 1785, on what was then called "dephlogisticated air," Rayleigh and Ramsay showed that argon had demonstrably been isolated even then. But chemistry was not far enough advanced in 1785 for Cavendish to realize what he was seeing.

The mass of argon was determined by Rayleigh and Ramsay to be, in modern units, about 40 u, and to compose about 1 % of the atmosphere. William Crookes [2, 3] measured its visible emission spectrum and determined that it corresponded with no known element. Rayleigh and Ramsay also determined, from the velocity of sound in argon, the ratio of specific heats (C_p/C_v); they found this ratio to be about 5/3, indicating a monatomic gas [2].

At the request of Rayleigh and Ramsay, Olszewski [2, 4] successfully liquefied and solidified argon. Among other things, he measured the critical point to be at (in modern units) 5 MPa, 152 K; current accepted values are 4.86 MPa, 150.7 K [5–9] . Hartley [10] showed that the argon spectrum was present in the spectrum of air, and Newall [11] showed that the argon spectrum had been measured previously in 1894, though of course not identified as argon at that time. Further, MacDonald and Kellas [12], at the request of Rayleigh and Ramsay, showed that argon, though found along with nitrogen in the atmosphere, was not present along with nitrogen in the tissues of plants and animals. This ruled out argon as possibly being a form of nitrogen.

The evidence, then, pointed to a newly discovered element, abundant in the environment, which did not engage in any known chemical reaction.

1.1.2 Argon and the periodic table

Argon presented a serious challenge to the periodic table [13–15].

The periodic table of 1895 was not, like that of today, based on quantum mechanics. It was a list of elements arranged by atomic mass. The chemical properties of elements were thought to be periodic with respect to atomic mass, though what atomic mass had to do with chemical properties was unknown. Furthermore, it was not even yet accepted by all chemists whether such things as atoms really existed, though almost all chemists accepted the atomic model as useful for understanding chemical reactions

Periods:	Groups:	I	II	III	IV	V	VI	VII	VIII (transition)			
0		H										
	Series:	Li	Be	B	C	N	O	F				
1	1	Na	Mg	Al	Si	P	S	Cl				
	2	K	Ca	–	Ti	V	Cr	Mn	Fe	Co	Ni	Cu
2	3	Cu	Zn	–	–	As	Se	Br				
	4	Rb	Sr	Y?	Zr	Nb	Mo	–	Ru	Rh	Pd	Ag
3	5	Ag	Cd	In	Sn	Sb	Te	I				
	6	Cs	Ba	–	Ce	–	–	–	–	–	–	–
4	7	–	–	–	–	–	–	–				
	8	–	–	–	–	Ta	W	–	Os	Ir	Pt	Au
5	9	Au	Hg	Ti	Pb	Bi	–	–				
	10	–	–	–	Th	–	U	–	–	–	–	–

Table 1.1: Mendeleev's periodic table of 1870 [16]. Atomic mass increases from left to right and from top to bottom. "–" indicates empty slots for elements yet to be discovered. "Y?" refers to the doubtful location of yttrium. Note that the last element in Group VIII is the first element of Group I in the next period.

[13–15].

The most successful periodic table was Mendeleev's, but his was only the latest in a long line of systems of classification of elements, and his table was published nearly contemporaneously with those of five other authors. While Mendeleev's table had held up well over twenty years, the periodic system had no theoretical justification [13–17]. A periodic table of Mendeleev's that may well be the one referred to by Rayleigh and Ramsay [2] is shown in Table 1.1.

Mendeleev's Group VIII contained the "transition elements;" these were the elements of multiple valency that were thought to have chemical properties "intermediate" with respect to Group VII and Group I. The last-listed element in Group VIII of a period is the first-listed element in Group I of the next period [16].

Mendeleev used his table to correct erroneously measured atomic masses of known elements, and to predict chemical properties and atomic masses of those yet to be discovered. In a few cases atomic masses stubbornly refused to obey the periodic law; for example, no matter how many times they were measured, the atomic mass of tellurium came out greater than that of iodine. But their respective chemical properties required that tellurium come before iodine in the table [13–15].

While there was room for more elements in the table–it was this very feature that made Mendeleev's table so widely accepted among chemists–there was no place for argon, unless some major finding of chemistry or physics were wrong. The properties which made argon so difficult to fit into the periodic system were these: it reacted with no known chemical, it had an atomic mass of 40 u, and it was a monatomic gas.

There was no reason to suppose that such a thing as an inactive element should exist. As suggested by Rayleigh and Ramsay [2], argon's chemical inactivity might be only apparent, and the conditions required for it to react might yet be discovered. Until they were discovered it would be impossible to definitively assign argon its place in the table, or to definitively say that the table must be wrong.

None of Mendeleev's groups were characterized by chemical inactivity, but Rayleigh and Ramsay [2] suggested that argon might go in Group VIII, after chlorine, as a transition to potassium. Unfortunately the atomic mass of argon was the same as that of calcium. It seemed too *ad hoc* to just assume that argon could be that far out of order with respect to atomic mass, or that the periodic table would put argon between two elements with properties so dissimiliar to its own.

Another possibility, suggested by Rayleigh and Ramsay [2], was that "argon" could be a mixture of two gases; "argon" of atomic mass 37 u, and "krypton" of atomic mass 82 u. If the mixture consisted of 93 % argon and 7 % krypton, this would explain the measured atomic mass of 40 u. Argon and krypton would both be inert, and argon could go in Group VIII between chlorine and postassium while krypton could go in Group VIII between bromine and rubidium. However, it seemed that such a relatively large fraction of krypton should have been detected when the argon-krypton mixture was liquefied, and the diffusion experiments of Rayleigh and Ramsay should have isolated a measurable quantity of krypton.

Other than mercury vapor, no monatomic gases were known in 1895. If argon were a diatomic molecule, then its atomic mass would be, at 20 u, just right to go in Group VIII as a transition from fluorine to sodium. Alternatively, argon might just be a compound of nitrogen; as Mendeleev suggested [13–15], it might be N_3. In both cases the kinetic theory of gases must be wrong, and atoms must not really exist.

Several other possibilities were suggested by other researchers, but all were unsatisfactory enough that none was accepted. It seemed, in 1895, that chemists must either abandon the periodic table, abandon the atomic theory and the kinetic theory of gases, or just ignore argon altogether [13–15]. As Lord Rayleigh said,

> The facts were too much for us; and all that we can do now is to apologise for ourselves and for the gas.[13]

All that could be definitively said about argon was that it was a newly discovered element which didn't seem to make any sense in relation to the others. Furthermore, it was quite abundant and had been "under everyone's nose" at least as far back as 1785.

The work previously done on argon enabled Ramsay, in the next few years, to isolate helium, neon, krypton, and xenon (from Greek for "sun," "new," "secret," and "strange," respectively). These had the same chemical inactivity as argon, but also had atomic masses that made sense in the periodic table, and were eventually regarded as a group in their own right, either coming before Group I or after Group VII.

The periodic table was vindicated–although it had not predicted a new class of elements characterized by chemical inactivity, it was able to accomodate them; and the new class of elements, in general, obeyed the periodic law. Argon was considered just one more exception to the general rule of increasing atomic mass [13–15].

Within a few decades, the periodic table was put on a solid theoretical foundation. Largely due to the experimental work of Moseley on X-rays and K-shell electrons [15], the role of electrons in chemistry was worked out according to quantum mechanical theories. The elements of the periodic table were then arranged by atomic number, rather than atomic mass, which eliminated the exceptions. Argon at 18 fits perfectly between chlorine at 17 and potassium at 19.

Lord Rayleigh and William Ramsay received the Nobel Prizes for Physics and Chemistry (respectively) in 1904 for their discovery of argon and the other noble gases.

1.2 Characteristics

1.2.1 Physical and chemical properties

The atomic number of argon is 18. It has three stable isotopes: ^{36}Ar, ^{38}Ar, ^{40}Ar. The first two are more abundant in the universe at large. However, on Earth ^{40}Ar, which is produced by the decay of ^{40}K, makes up 99.6 % of argon and is found in rocks, the atmosphere (1 % by volume), and dissolved in the oceans [5–9].

At ambient pressure, argon liquefies at 87.3 K and solidifies at 83.8 K [5–9]. At ambient temperature argon solidifies at 1.35 GPa [20]. Its triple point is at 83.81 K, 68.95 kPa. Its critical point is at 150.7 K, 4.86 MPa [5–9]. Figure 1.1 shows the phase diagram up to 10 GPa and 800 K.

Solid argon is face-centered cubic (fcc). Figure 1.2 shows the structure. Around 30 GPa hexagonal close-packed (hcp) structures begin to form. The fcc and hcp phases are predicted to coexist up to around 300 GPa, at which point the solid should be hcp. Body-centered cubic phases and metallization are predicted at much higher pressures but have not so far been observed [21–24].

Our experimental work was done at ambient temperature. For the lowest pressures

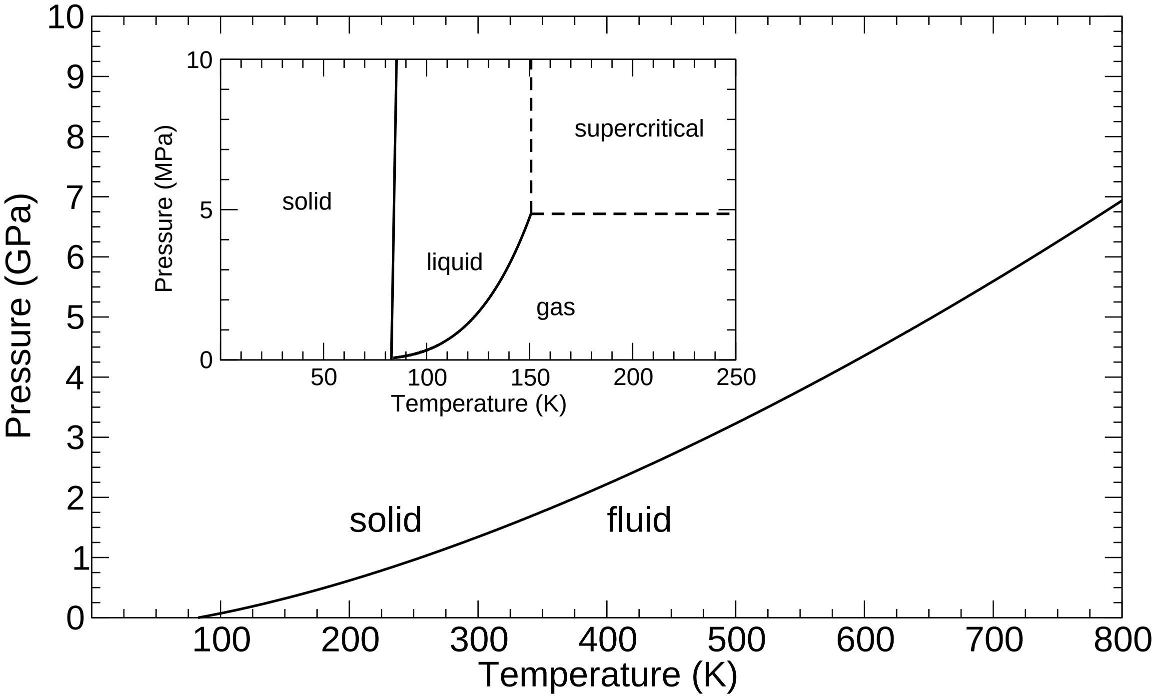

Figure 1.1: Phase diagram for argon, showing the melting line to 800 K [18]. Inset: the liquid-gas phase boundary [19], encountered at far lower pressures and temperatures than were achieved in this work.

we can achieve in a diamond anvil cell (about 0.2 GPa) argon is a supercritical fluid. The highest pressures we achieved in this work were under 10 GPa.

1.2.2 In theory and experiment

Only one chemical compound of argon is known, argon fluorohydride (HArF), discovered only in 2000 and stable only under unusual conditions [25]. The heavier noble gases, xenon and radon, can be induced to form a few compounds, and helium and neon are not known to form any [26, 27].

The noble gases are chemically inactive due to their filled valence shells; reminding us that Argan, in 1673, found that opium puts people to sleep due to its dormitive virtue [28]. A better explanation can be found in the spherical symmetry of their electronic wavefunctions [29–31], as will be detailed later (section 2.1).

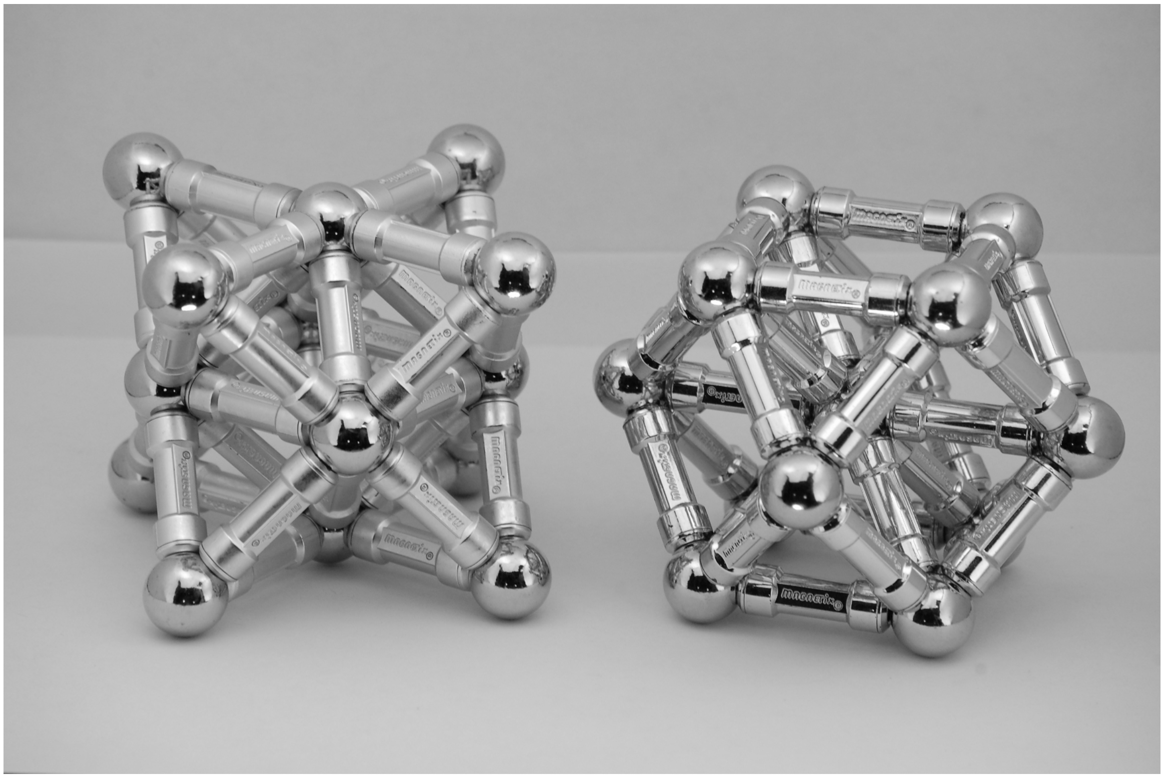

Figure 1.2: Face-centered cubic structure (fcc). Left: fcc unit cell. The length of the side of the unit cell, L, and the interatomic distance a, are related by $L = a\sqrt{2}$. Right: atom-centered view of fcc structure. The central atom has 12 nearest neighbors, all at the same interatomic distance a. There are 3-fold as well as 4-fold symmetry axes.

The interatomic forces between noble gas atoms are isotropic and very weak, and as gases they show nearly ideal behavior. Their deviations from ideality provide important clues to the details of their interatomic interactions [20, 32, 33].

Noble gas atoms can be treated to high accuracy as interacting through purely atomic potentials (without considering interactions between electrons and nuclei) [20, 32, 33]. The atoms repel at short distances and attract at longer ones, with a potential minimum between, as will be derived later (section 2.2) from the Schrödinger equation and the Pauli exclusion principle. This was first done in the 1920s and 1930s by Lennard-Jones [29, 30], London [34], Slater [35], Pauling [36], and others and was an early success for quantum mechanics.

For substances interacting by hard-sphere two-body potentials, the equation of state can be worked out exactly and analytically [37]. The computers of the 1940s and 1950s could carry out numerical calculations for more complicated potentials such as that of Lennard-Jones, but for many years calculations involving anisotropy or many-body forces were computationally prohibitive [38]. In noble gases these effects are very small, so they were the first substances for which chemical and macroscopic propertes could be worked out from first principles.

Within the noble gases argon occupies a "sweet spot"–massive enough to be treated classically or semiclassically to good accuracy, unlike helium and neon; but small enough that its electrons hardly interact with other elements, unlike the electrons of xenon and radon [26, 27]. Argon has the added virtues of being cheap, abundant, and easy to handle [20].

In summary, argon is a model substance for fundamental atomic and condensed matter physics.

1.3 Applications

Argon is interesting in its own right for what it can tell us about fundamental atomic physics, but it also has practical applications.

Argon is by far the cheapest and most abundant of the noble gases [20]. It is produced by fractional distillation of air, usually as a byproduct of oxygen production. This has the interesting consequence that when demand for steel drops, the price of argon goes up [39].

Due to its relative cheapness, commercial and industrial applications of argon are widespread. Argon is generally used in circumstances when an inert gas is needed and nitrogen will not work. Nitrogen may not be unreactive enough, or nitrogen may be too thermally conductive.

Some examples of commercial and industrial applications are: inert atmospheres for welding, glove boxes, electronics manufacture, crystal growth, incandescent and fluorescent lighting, and as a thermal insulator in double-pane windows [20, 39–41].

Some examples of scientific applications of argon are: as a carrier gas for mass spectrometry, as a hydrostatic pressure medium in diamond anvil cells, and as a method of dating rocks and fossils [20, 41, 42].

1.4 Subject of and motivation for this work

In this work we study the equation of state of fluid argon at 300 K in a diamond anvil cell, and we use the vibrational modes of dissolved carbon dioxide to probe the fluid argon structure.

From the experimental data we collect, we hope to draw some conclusions about the interatomic interactions of argon, and the structure of the fluid state. This will be useful to theorists who wish to work from first principles to understand macroscopic and chemical properties. It will also be useful to researchers in the static high pressure field who wish to use argon as a hydrostatic pressure medium and as a pressure standard.

Our experimental techniques include: confocal microscopy, used to obtain equation of state data for fluids, which will be developed in this work; and Fourier transform infrared spectroscopy, used to measure the localized modes of carbon dioxide in argon.

To our knowledge, this is the first time that confocal microscopy has been used to measure the volume of a fluid under pressure. Fluid volumes are difficult to measure. Argon is a model system that provided a good test of this novel experimental technique.

There are other techniques of measuring fluid volumes. One is Fabry-Perot interference, which yields the product of refractive index and sample thickness. Consequently some other method must be used to find one of those two quantities separately. The reflection of the laser between the culets of the diamonds forms monochromatic rings, which may be imaged, and the index of refraction calculated from the radii of successive rings. [43, 44]. Another method is that described in section 4.2.8, which does not require a confocal microscope [45], but is much more easily done with one [46].

Another method is X-ray tomographic microscopy, which produces 3D images of samples at high pressure with a spatial resolution of about 1 μm [47]. This requires advanced, specialized, and expensive technology.

The virtues of confocal microscopy are that it is inexpensive, quick, non-destructive, and uses commercially available equipment found at many universities.

1.5 Bibliography

[1] Lord Rayleigh. On an anomaly encountered in determinations of the density of nitrogen gas. *Proceedings of the Royal Society of London*, 55:340–344, 1894.

[2] Lord Rayleigh and William Ramsay. Argon, a new constituent of the atmosphere. *Philosophical Transactions of the Royal Society of London. A*, 186:187–241, 1895.

[3] William Crookes. On the spectra of argon. [abstract]. *Proceedings of the Royal Society of London*, 57:287–289, 1895.

[4] K. Olszewski. The liquefaction and solidification of argon. [abstract]. *Proceedings of the Royal Society of London*, 57:290–292, 1895.

[5] David R. Lide, editor. *CRC Handbook of Chemistry and Physics.* CRC Press, Boca Raton, FL, 90th edition, 2009.

[6] R. Bruce King, editor. *Encyclopedia of inorganic chemistry.* John Wiley and Sons, 1994.

[7] J. J. Lagowski, editor. *Chemistry: foundations and applications.* Thomson-Gale, 2004.

[8] Glenn D. Considre, editor. *Van Nostrand's encyclopedia of chemistry.* John Wiley and Sons, 2005.

[9] Hans-Dieter Jakubke and Hans Jeschkeit, editors. *Concise encyclopedia of chemistry.* Walter de Gruyter and Co, 1993.

[10] W. N. Hartley. On the spark spectrum of argon as it appears in the spark spectrum of air. *Proceedings of the Royal Society of London*, 57:293–296, 1895.

[11] H. F. Newall. Note on the spectrum of argon. *Proceedings of the Royal Society of London*, 57:346–350, 1895.

[12] George W. MacDonald and Alex. M. Kellas. Is argon contained in vegetable or animal substances? *Proceedings of the Royal Society of London*, 57:490–492, 1895.

[13] Carmen J. Giunta. Argon and the periodic system: the piece that would not fit. *Foundations of Chemistry*, 3:105–128, 2001.

[14] Michael D. Gordin. *A well-ordered thing: Dmitrii Mendeleev and the shadow of the periodic table.* Basic Books, 2004.

[15] Eric Scerri. *The periodic table: its story and significance.* Oxford University Press, 2007.

[16] Edward G. Mazurs. *Graphic representations of the periodic system during one hundred years.* The University of Alabama Press, 1974.

[17] T. R. Seshadri, editor. *Mendeleyev's periodic classification of elements and its applications.* Hindustan Publishing Corporation (India), 1973.

[18] F. Datchi, P. Loubeyre, and R. LeToullec. Extended and accurate determination of the melting curves of argon, helium, ice (H_2O), and hydrogen (H_2). *Physical Review B*, 61:6535–6546, 2000.

[19] S. Angus and B. Armstrong, editors. *International Thermodynamic Tables of the Fluid State, Argon, 1971,IUPAC*. Butterworth's, 1972.

[20] M. L. Klein and J. A. Venables, editors. *Rare gas solids*. Harcourt Brace Jovanovich, 1976.

[21] D Errandonea, R Boehler, S Japel, M Mezouar, and LR Benedetti. Structural transformation of compressed solid Ar: An x-ray diffraction study to 114 GPa. *Physical Review B*, 73:092106–1 – 092106–4, 2006.

[22] R Boehler, M Ross, P Soderlind, and DB Boercker. High-pressure melting curves of argon, krypton, and xenon: Deviation from corresponding states theory. *Physical Review Letters*, 86:5731–5734, 2001.

[23] A. K. McMahan. Structural transitions and metallization in compressed solid argon. *Physical Review B*, 33:5344 – 5349, 1986.

[24] I. Kwon, L. A. Collins, and J. D. Kress. First-principles study of solid Ar and Kr under high compression. *Physical Review B*, 52:15165 – 15169, 1905.

[25] L. Khriachtchev, M. Pettersson, N. Runeberg, J. Lundell, and M. Räsänen. A stable argon compound. *Nature*, 406:874–876, 2000.

[26] L. Pauling. The formulas of antimonic acids and the antimonates. *Journal of the American Chemical Society*, 55:1895 – 1900, 1933.

[27] John R. Holloway. *Noble-gas chemistry*. Richard Clay, Ltd., 1968.

[28] Moliere. The imaginary invalid, 1673.

[29] J. E. Lennard-Jones. Cohesion. *The Proceedings of the Physical Society*, 43:461 – 482, 1931.

[30] J. E. Lennard-Jones. The quantum mechanics of atoms and molecules. *Journal of the London Mathematical Society*, s1-6 (4):290 – 318, 1931.

[31] I. E. Dzyaloshinskii, E. M. Lifshitz, and L. P. Pitaevskii. General theory of van der Waals' forces. *Soviet Physics Uspekhi*, 73:153–176, 1961.

[32] H. Margenau and N. R. Kestner, editors. *Theory of intermolecular forces.* Pergamon Press, 1969.

[33] D. Tabor. *Gases, liquids and solids: and other states of matter.* Cambridge University Press, 3rd. edition, 1969.

[34] F. London. The general theory of molecular forces. *Transactions of the Faraday Society*, 33:8–26, 1937.

[35] J. C. Slater and G. J. Kirkwood. The van der Waals forces in gases. *Physical Review*, 37:682–692, 1931.

[36] L. Pauling and J. Y. Beach. The van der Waals interaction of hydrogen atoms. *Physical Review*, 47:686–692, 1935.

[37] William W. Wood. Note on the free volume equation of state for hard spheres. *The Journal of Chemical Physics*, 20:1334, 1952.

[38] N. Metropolis, A. Rosenbluth, M. Rosenbluth, and A. Teller. Equation of state calculations by fast computing machines. *The Journal of Chemical Physics*, 21:1087–1092, 1952.

[39] Kimberley Gilles. Gas prices rising higher than ever. *Welding Design & Fabrication*, 79(11):12 – 30, 2006.

[40] Y. S. Touloukian and C. Y. Ho, editors. *McGraw-Hill / Cindas data series on material properties, Volume III-2: properties of non-metallic fluid elements.* McGraw-Hill, 1981.

[41] Gerhard A. Cook, editor. *Argon, helium, and the rare gases.* John Wiley and Sons, 1961.

[42] L. W. Finger, R. M. Hazen, G. Zou, H. K. Mao, and P. M. Bell. Structure and compression of crystalline argon and neon at high pressure and room temperature. *Applied Physics Letters*, 39:892–894, 1981.

[43] A. Dewaele, J. Eggert, P. Loubeyre, and R. LeTouellec. Measurement of refractive index and equation of state in dense He, H_2, H_2O, and Ne under high pressure in a diamond anvil cell. *Physical Review B*, 67:094112–1–094112–8, 2003.

[44] M Grimsditch, R. Letoullec, A. Polian, and M. Gauthier. Refractive index determination in diamond anvil cells: results for argon. *Journal of Applied Physics*, 60:3479–3481, 1986.

[45] W. Evans and I. Silvera. Index of refraction, polarizability, and equation of state of solid molecular hydrogen. *Physical Review B*, 56:14105–14109, 1998.

[46] G. J. Hanna and M. D. McCluskey. Measuring the volume of a fluid in a diamond anvil cell using a confocal microscope. *Applied Optics*, 48:1758–1763, 2009.

[47] Y. Wang, T. Uchida, F. Westferro, M. Rivers, N. Nishimaya, J. Gebhardt, C. Lesher, and S. Sutton. High-pressure x-ray tomograpy microscope: synchrotron

computed microtomography at high pressure and temperature. *Review of Scientific Instruments*, 76:073709–1–073709–7, 2005.

Chapter 2

Interatomic interactions

It is extremely difficult to make argon react chemically with anything, and the phase diagram of argon (up to about 100 GPa) is very simple. What is it about argon (and the other noble gases) that is different from all other elements?

There are many different types of chemical "bonds". Ionic bonds form when an electron from one atom is transferred to another, as in the case of table salt. In covalent bonds electrons are shared between atomic nuclei, as in the cases of hydrogen, oxygen, and nitrogen. There are bonds intermediate in some degree, as covalent and ionic bonding represent extremes on a continuum [1, 2]. In metallic bonds, some electrons in the metal are not localized to any one atom. There are hydrogen bonds, where a hydrogen atom, covalently bonded to another atom, is made sufficiently non-polar to strongly attract a third atom. This type of bond is present in water and many proteins. Van der Waals bonds are responsible for the solid and liquid phases of the noble gases. They are present to some degree between all atoms and molecules, though nearly always weaker than any other bond that may be present [1–3].

Words mean what we want them to mean–it is a question of which is to be master [4]. In this work a "chemical bond" is when an electron from one atom is associated

Quantity	Atomic unit	Name	SI equivalent	Other equivalent
Mass	m_e	electron mass	$9.109\,38 \times 10^{-31}\,\mathrm{kg}$	$\frac{1}{1823}$ u
Charge	e_c	electron charge	$1.602\,18 \times 10^{-19}\,\mathrm{C}$	—
Angular momentum	$\hbar$	$\hbar$	$1.054\,57 \times 10^{-34}\,\mathrm{J\,s}$	—
Length	a_0	Bohr radius $\left(\frac{4\pi\epsilon_0\hbar^2}{m_e e_c^2}\right)$	$0.052\,917\,7\,\mathrm{nm}$	$0.529\,177\,\mathrm{Å}$
Energy	E_h	hartree $\left(\frac{e_c^2}{4\pi\epsilon_0 a_0}\right)$	$4.359\,74 \times 10^{-18}\,\mathrm{J}$	$27.2114\,\mathrm{eV}$

Table 2.1: Atomic units and their SI equivalents, along with equivalents in other commonly used units. Bohr radius and hartrees are calculated assuming infinite nuclear mass, which simplifies comparisons between atoms of differing masses.

with the nucleus of another. While it is not unknown in the literature to refer to, for example, two helium atoms at low temperature as a “molecule” [5], in this work we do not. Of the various types of bonds only covalent, ionic, and metallic bonds are “chemical bonds” by this definition. The other kinds could be called “atomic bonds”, if it is necessary to name them.

We choose this definition so that we can characterize the difference between noble gases and the other elements in terms of their electronic structures, which are determined by the number of protons Z in their nuclei. Using this approach we can show why noble gases are so reluctant to form chemical bonds and what sort of interatomic interactions they do exhibit.

In dealing with electrons and nuclei, it is most convenient to work in atomic units, which are defined in table 2.1 [6].

2.1 The argon atom

The chemical behavior of any atom is determined by the structure of its electrons, which in turn is determined by its atomic number [3].

A bare atomic nucleus has the Coulomb potential

$$V(r) = -Z\frac{E_h}{e_c}\frac{a_0}{r}, \tag{2.1}$$

and one-electron atoms can be solved exactly and analytically (neglecting spin). The solutions are well-known [6, 7] and will not be restated here, but a few details are worth reviewing.

Each eigenfunction is a product of a radial function and a spherical harmonic, characterized by the quantum numbers n, l, m. The eigenenergies are given by

$$E_n = -\frac{1}{2}\frac{Z^2}{n^2}E_h. \tag{2.2}$$

Each eigenfunction has an associated angular momentum $l(l+1)\hbar^2$. For each value of l the associated eigenfunction has a particular symmetry, with $l = 0$ corresponding to spherical symmetry. The orientation along the z axis is associated with m. The possible values of the quantum numbers are determined by n; l ranges from 0 to $n-1$ and m ranges from $-l$ to l. Each set of eigenfunctions with the same n are called *shells*; those with the same l are called *subshells*. There is a characteristic length scale given by $\frac{n}{Z}a_0$, which is the exponential decay constant of the radial function and can serve as a measure of the size of the shell [6, 7].

The structures of many-electron atoms may be calculated to great precision. There are several techniques for working them out, depending on the desired accuracy and which effects one wishes to include. In this section, we are concerned with demonstrating that (1) some atoms have high spherical symmetry in their ground states, and (2) a subset of these atoms, the noble gases, are chemically unreactive [8].

Imagine assembling an atom, starting with a bare nucleus of Z protons and adding one electron at a time until the atom is neutral. The first electron goes into the ground state hydrogenic orbit ($n = 1, l = 0$), giving a spherically symmetric distribution of radius $\frac{1}{Z}a_0$. Bringing in a second electron, it can be argued, should not disturb the other electron significantly. If the two electrons do not interact at all, then they can be in the same spatial eigenstate if their spins are opposite, by the Pauli exclusion principle. In this case, we treat the electron-electron interaction as a small perturbation, and consider them both in the $n = 1$ shell. Of course, the radius, energy and associated properties will be slightly different from those calculated from the one-electron atom.

The two electrons are distributed in space over the spherical shell they occupy, a bit like a cloud. Treating the electrons like an extended charge distribution,

$$\begin{aligned} \rho(r) &= -2\rho_0 e^{-2Z\frac{r}{a_0}}, && (2.3) \\ \rho_0 &\equiv \frac{2}{\pi}\left(\frac{Z}{a_0}\right)^3 e_c, && (2.4) \end{aligned}$$

then by Gauss's Law a third electron brought to this atom should experience a Coulomb-like electrical field

$$\begin{aligned} \vec{E}(r) &= -\left(Z - 2\left(1 - e^{-2Z\frac{r}{a_0}}\right)\right)\frac{E_h}{e_c}\frac{a_0}{r^2}\hat{r}, \\ \vec{E}(r)\Big|_{r>>a_0/z} &\approx -(Z-2)\frac{E_h}{e_c}\frac{a_0}{r^2}\hat{r}, \end{aligned} \qquad (2.5)$$

outside the shell. This is called "shielding". However, the model presented here is far too simple. Electrons are point particles and it is fundamentally wrong to treat them as charge distributions [2]. To obtain reasonable results, one must calculate the electron density using numerical techniques.

One approach is the Hartree-Fock self-consistent field method [9], which replaces the electron-electron interactions with an effective central potential

$$V(r) = -Z_{eff}(r)\frac{E_h}{e_c}\frac{a_0}{r}. \qquad (2.6)$$

This potential and its associated eigenfunctions and eigenenergies are calculated numerically. The details of such a calculation do not concern us here. Regardless of how one obtains the effective potential, its spherical symmetry implies that the angular part of the eigenfunctions are the spherical harmonics. Thus, there are shells and subshells corresponding to n and l. However, one important difference from the one-electron atom is that the eigenenergies are no longer functions of n alone, but also l.

What stays the same is the angular distribution of the spherical harmonics. This has implications for chemical properties. Each subshell has room for $2(2l+1)$ electrons, by the exclusion principle. If a subshell is entirely full, the overall distribution of electrons is spherically symmetric. Electrons outside the last filled subshell experience only a weak attraction to their own atom due to screening. Their lack of spherical symmetry implies a multipole moment which will attract other atoms, bringing them close enough together so that their electrons will interact. If the electron configurations interact so that some of the electrons can be associated with the opposite nucleus, we refer to this as a chemical bond [1, 3].

Neutral, spherical atoms, on the other hand, have no multipole moments, and hence little attraction to each other. The subshells of noble gases are already filled, so when they are brought close together, their electrons do not interact with each other except by repulsion. Furthermore, the electrons in one atom are not significantly affected by the nucleus of the other. At very high pressures or temperatures, their electronic configurations may distort somewhat. Nonetheless, the electrons remain associated with their own atoms and do not form chemical bonds, as the term is used in this work.

Spherical symmetry, though necessary, is not sufficient to explain chemical inactivity. The electron distributions of the IA and IIA elements are also spherical, and IIA elements also have filled subshells.

The difference between the chemical inactivity of noble gases and the chemical activity of the other spherical atoms is explained by the l dependence of the energy of the subshell. A purely Coulombic potential has no l dependence (this is peculiar to the Coulomb potential, as can be seen by writing the Hamiltonian in parabolic coordinates) [6]. In multielectron atoms, the energy difference between $l = 0$ and $l = 1$ is small. Electrons are easily excited from one to the other, so the $l = 0$ subshell is unstable for $n > 1$. Hence, beryllium and magnesium are not noble gases but neon is. The difference between $l = 1$ and $l = 2$ is more pronounced. Argon is a noble gas despite not filling the $n = 3$ shell, but it must fill both its $l = 0$ and $l = 1$ subshells just as neon does.

Higher atomic numbers have more complicated electronic structures. The energy of subshells of lower n shells begins to overlap the subshells of higher n shells, and so nickel, at atomic number 28, is not a noble gas; its $3d$ shell is partially filled. Were it not for the overlap, nickel might fill the $3d$ shell and thus be one of the noble gases. The next noble gas is krypton at atomic number 36, which fills the $l = 0$ and $l = 1$ subshells of the $n = 4$ shell, and all the subshells of the lower shells. Xenon at 54 does not fill the $l = 3$ subshell of the $n = 4$ shell, but rather fills the first two subshells of $n = 5$ [1].

Of course, chemical properties are not entirely explained by “filling subshells;” this is why we have to talk about “shells overlapping.” The idea nonetheless has value. Even if one can solve the full Hamiltonian of each and every atom as precisely as one likes, deriving atomic properties *ab initio*, there still needs to be some way of organizing the results. The rules for filling shells are easy to remember even if they get more complicated and arbitrary as atomic number increases [1].

In summary, the inactivity of the noble gases is explained by the spherical symmetry and stability of their electronic configurations. The symmetry and stability can be demonstrated approximately by comparison with the hydrogenic eigenfunctions.

2.2 Two-body interactions

2.2.1 Van der Waals attraction

Neutral atoms and molecules exert attractive forces on one another. Some of these attractions, like those between water molecules which have permanent dipole moments, are "obvious" from a classical physics standpoint. But even spherically symmetric neutral atoms attract one another. This is not obvious. Given a spherically symmetric charge distribution, with a decaying exponential dependence, there should be practically no field a few atomic radii from the nucleus [2]. In this work, we reserve the term *van der Waals attraction* for this particular effect.

If one thinks of a cloud of electrons orbiting a nucleus, something like the stars orbiting the center of mass of a globular cluster, it is easy to see that the spherical symmetry of the charge distribution is only a time-averaged property of the atom. One can then think of neutral spherical atoms as instantaneously fluctuating dipoles, which would attract each other: one dipole would form instantaneously, and polarize the other atom briefly [2]. However, the solutions to the time-independent Schrödinger equation are distributions in space which do not vary with time. It should therefore be possible to explain van der Waals attraction without invoking fluctuating dipoles [2].

Van der Waals forces necessarily exist between all neutral atoms, but in noble gases they are the leading term in the interatomic potential. Since noble gases all contain more than one electron, and solving their Schrödinger equations is a large undertaking, as shown in the previous section, we will derive the functional form of the van der Waals equation from the hydrogen atom [10].

Consider two hydrogen atoms, the nuclei of which are separated by a distance R, which will serve to define the z-axis. We consider the nuclei to be fixed in space (the Born-Oppenheimer approximation), so that R is a parameter, not a variable of the

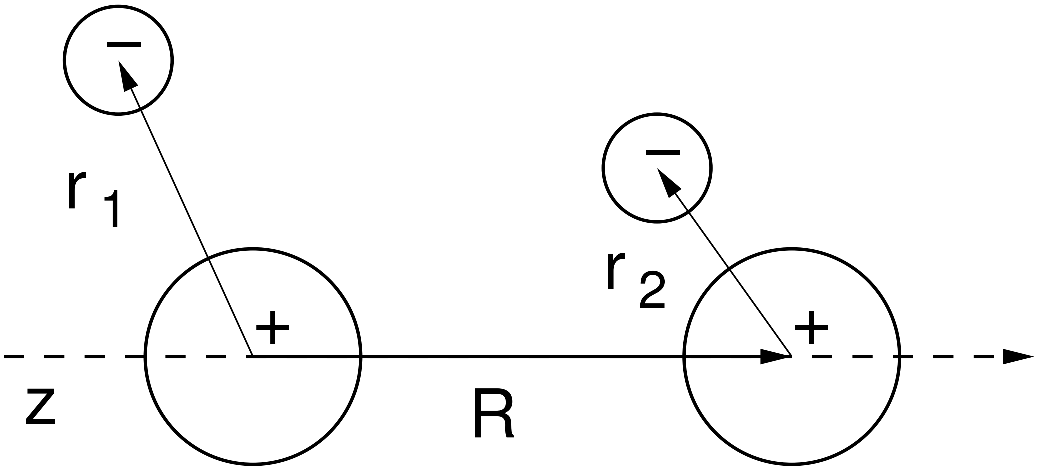

Figure 2.1: Coordinate system for van der Waals potential calculation.

system. The variables are $\vec{r_1}$, the position of electron 1 with respect to nucleus 1, and $\vec{r_2}$, the position of electron 2 with respect to nucleus 2, as shown in figure 2.1. We write the Hamiltonian:

$$\begin{aligned}\hat{H} &= -\frac{\hbar^2}{2m_e}\nabla^2_{r_1} - \frac{\hbar^2}{2m_e}\nabla^2_{r_2} - E_h\frac{a_0}{r_1} - E_h\frac{a_0}{r_2} \\ &\quad +E_h\frac{a_0}{R} - E_h\frac{a_0}{|\vec{R}-\vec{r_1}|} - E_h\frac{a_0}{|\vec{R}+\vec{r_2}|} + E_h\frac{a_0}{|\vec{R}+\vec{r_2}-\vec{r_1}|}.\end{aligned} \tag{2.7}$$

The first four terms are the Hamiltonians of two hydrogen atoms that do not interact. If $R >> r_1, r_2$ then the last four terms can be treated as a perturbation, and the eigenfunctions of the hydrogen atom can be used as a basis set:

$$\Psi(r_1,\theta_1,\phi_1,r_2,\theta_2,\phi_2) = |\Psi_{n_1,l_1,m_1,n_2,l_2,m_2}\rangle = |n_1,l_1,m_1\rangle \otimes |n_2,l_2,m_2\rangle\,. \tag{2.8}$$

Each hydrogen atom, in its ground state, has an energy $E_0 = -\frac{1}{2}E_h$, with a_0 being the Bohr radius, and we rewrite the perturbing potential as

$$\lambda V = \frac{a_0}{R}2E_h\left(\begin{array}{ll} 1 & -\left(1+\frac{r_1^2}{R^2}-2\frac{\vec{R}\cdot\vec{r_1}}{R^2}\right)^{-1} \quad -\left(1+\frac{r_2^2}{R^2}+2\frac{\vec{R}\cdot\vec{r_2}}{R^2}\right)^{-1} \\ & +\left(1+\frac{r_1^2}{R^2}+\frac{r_2^2}{R^2}+2\frac{\vec{R}\cdot\vec{r_1}}{R^2}-2\frac{\vec{R}\cdot\vec{r_2}}{R^2}-2\frac{\vec{r_1}\cdot\vec{r_2}}{R^2}\right)^{-1}\end{array}\right). \tag{2.9}$$

Using the binomial theorem we can expand the denominators, and almost everything cancels:

$$\lambda\hat{V} = \frac{a_0}{R}\frac{2E_h}{R^2}(\vec{r_1}\cdot\vec{r_2}). \tag{2.10}$$

Consider the hydrogen atoms in their ground state, represented by Ψ_0, with an unperturbed energy $2E_0$. The effect of the perturbation on the ground state of the hydrogen atoms is, to first order, zero. This is because $\langle\Psi_0|\,\vec{r_1}\cdot\vec{r_2}\,|\Psi_0\rangle$ is a measurement of the dipole moments of the hydrogen atoms perpendicular and parallel to the z-axis. Since the ground state is spherically symmetric, neither atom has a dipole moment in any direction. Consequently, we must evaluate the second order term

$$E^{(2)} = \lambda^2 \sum_n^g \sum_g \frac{\left|\left\langle \Psi_n^g \left| \hat{V} \right| \Psi_0 \right\rangle\right|^2}{2E_0 - E_n} = -\frac{a_0^2}{R^2}\frac{4E_h^2}{R^4}\sum_n^g \sum_g \frac{\left|\left\langle \Psi_n^g \middle| \vec{r_1}\cdot\vec{r_2} \middle| \Psi_0 \right\rangle\right|^2}{2E_h + E_n}, \tag{2.11}$$

where n is the index over the energy levels of the unperturbed Hamiltonian and g the index over the degeneracies of those levels. We don't actually have to carry out the calculation to see that

$$E^{(2)} \propto -\frac{1}{R^6} = -\frac{C_6}{R^6}, \tag{2.12}$$

and it was never necessary to invent instantaneous fluctuations in charge density. The attraction exists because the perturbing potential distorts the spherical charge densities, making them slightly multipolar.

Of course we have only kept the leading order term. Other terms exist, and there are van der Waals attractions proportional to R^{-8}, R^{-10}, and so forth [10]. Since the R^{-6} term is the most important it is more or less synonymous with "van der Waals attraction".

Naturally the numerical value of the proportionality constant is important if one wishes to deal with real atoms. For the Lennard-Jones model

$$V(R) = 4\epsilon\left[\left(\frac{\sigma}{r}\right)^{12} - \left(\frac{\sigma}{r}\right)^{6}\right], \tag{2.13}$$

the proportionality constant is $4\epsilon\sigma^6$. For argon $\epsilon = 3.82 \times 10^{-4} E_h, \sigma = 6.43 a_0$ [11], which yields $C_6 = 108 E_h a_0^6$.

2.2.2 Exchange repulsion

In the last section we showed that neutral spherical atoms should attract one another despite having very little field, of any kind. We demonstrated this attraction by assuming the electrons in the atoms can be approximated by their normal ground state.

As the atoms get closer, however, the perturbation, which depends on R, is no longer small. All of the electrons begin to feel the effects of both nuclei.

Electrons are identical fermions, and their overall state must be antisymmetric with respect to exchange. The electrons of the two atoms are in identical spin states (there is only one way to completely fill a subshell). Consequently, their overall wavefunction must be antisymmetric. If one thinks of the spatial distribution of the electrons, it must be zero between the atoms, which translates into a repulsive potential at short distances. Another way to think of this is that the Pauli exclusion principle forces them to resist being brought together, increasing the potential energy.

Again we should like to use the hydrogen atom to demonstrate the functional form of the effect. Perturbation theory, as used in section 2.2.1, will not work because it does not account for exchange. Instead we use the Rayleigh-Ritz variational method:

$$\frac{\left\langle \psi_T \middle| \hat{H} \middle| \psi_T \right\rangle}{\left\langle \psi_T \mid \psi_T \right\rangle} = E_T \geq E_0, \tag{2.14}$$

where ψ_T is a trial solution, which might contain parameters which may be adjusted to minimize E_T. E_T is the upper-bounded estimate of E_0, which in turn is the ground-state solution for $\hat{H}$ [6, 7].

The four possible spins states of two electrons are

$$\begin{array}{ll} \text{triplet} & \left\{ \begin{array}{c} |\uparrow\uparrow\rangle \\ |\downarrow\downarrow\rangle \\ \frac{1}{\sqrt{2}}(\,|\uparrow\downarrow\rangle + |\downarrow\uparrow\rangle\,) \end{array} \right. \\ \text{singlet} & \left\{ \ \frac{1}{\sqrt{2}}(\,|\uparrow\downarrow\rangle - |\downarrow\uparrow\rangle\,) \right. \end{array} \tag{2.15}$$

If the electrons are in the singlet state, then their overall spatial wavefunction must be symmetric under exchange, and this would constitute a covalently bonded H_2 molecule. In order to exhibit repulsion, they must be in the triplet state. Consequently, following Heitler and London [12], we use the antisymmetrized ground states of the two separated hydrogen atoms as the trial solution to the very same Hamiltonian that we used to demonstrate the van der Waals attraction,

$$\begin{aligned} \hat{H} &= -\frac{\hbar^2}{2m_e}\nabla^2_{r_1} - \frac{\hbar^2}{2m_e}\nabla^2_{r_2} - E_h\frac{a_0}{r_1} - E_h\frac{a_0}{r_2} \\ &+ E_h\frac{a_0}{R} - E_h\frac{a_0}{|\vec{R}-\vec{r_1}|} - E_h\frac{a_0}{|\vec{R}+\vec{r_2}|} + E_h\frac{a_0}{|\vec{R}+\vec{r_2}-\vec{r_1}|}, \qquad (2.16) \\ \psi_T &= \frac{1}{\sqrt{2}}\left(\phi(r_1)\phi(r_2) - \phi(|\vec{R}-\vec{r_1}|)\phi(|\vec{R}+\vec{r_2}|)\right), \qquad (2.17) \\ \left\langle \psi_T \middle| \hat{H} \middle| \psi_T \right\rangle &= E_h\left(1 + \frac{a_0}{R} + \frac{\left\langle \psi_T \middle| \frac{a_0}{|\vec{R}-\vec{r_1}|} + \frac{a_0}{|\vec{R}+\vec{r_2}|} + \frac{a_0}{|\vec{R}+\vec{r_2}-\vec{r_1}|} \middle| \psi_T \right\rangle}{\langle \psi_T \mid \psi_T \rangle}\right). \qquad (2.18) \end{aligned}$$

Since E_h is the energy of two separated hydrogen atoms we can subtract it from the energy, so that the energy of the two-atom system goes to zero at infinite separation.

We can then rewrite the energy (following Slater [13]) as

$$\left\langle \psi_T \left| \hat{H} \right| \psi_T \right\rangle = E_T = E_h \frac{H_0 - H_1}{1 - I^2}. \tag{2.19}$$

An explanation of H_0, H_1, and I follows.

H_0 is the *Coulomb integral*

$$\int\int \phi^2(r_1)^2 \phi^2(r_2) \left(\frac{a0}{R} + \frac{a0}{\left|\vec{R} - \vec{r_1} + \vec{r_2}\right|} - \frac{a0}{\left|\vec{R} - \vec{r_1}\right|} - \frac{a_0}{\left|\vec{R} + \vec{r_2}\right|} \right) dV_1 \, dV_2. \tag{2.20}$$

This integral can be interpreted as electrostatic energy. If the ϕ^2 are interepreted as charge distributions, H_0 is the energy of the repulsion of the nuclei, the repulsion of each electronic charge distribution for the other, and the attraction for each electronic charge distribution to the other nucleus. This energy is repulsive at short distances and attractive at long distances.

I is the *overlap integral*

$$I = \int \phi(r_1) \phi\left(\left|\vec{R} - \vec{r_1}\right| \right) dV_1 = \int \phi(r_2) \phi\left(\left|\vec{R} + \vec{r_2}\right| \right) dV_2, \tag{2.21}$$

which can be interpreted as the charge density for an electron shared between two nuclei. It is at a maximum of 1 when the nuclei are at zero separation, and goes to zero at infinite separation.

H_1 is the *exchange integral*

$$H_1 =$$
$$\int\int \phi(r_1) \phi\left(\left|\vec{R} - \vec{r_1}\right| \right) \phi(r_2) \phi\left(\left|\vec{R} + \vec{r_2}\right| \right) \left(\frac{a0}{R} + \frac{a0}{\left|\vec{R} - \vec{r_1} + \vec{r_2}\right|} - \frac{a0}{\left|\vec{R} - \vec{r_1}\right|} - \frac{a_0}{\left|\vec{R} + \vec{r_2}\right|} \right) dV_1 \, dV_2. \tag{2.22}$$

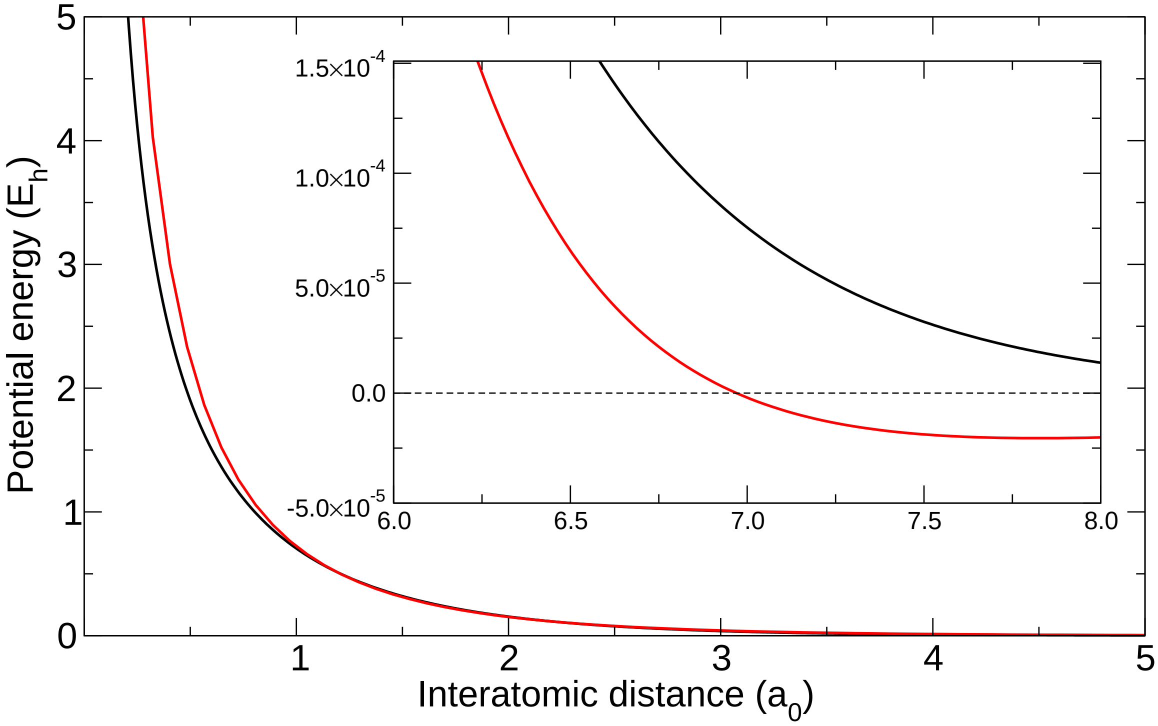

Figure 2.2: Exchange repulsion energy E_T. Black: Result of the Heitler-London calculation. Red: Fit to $\frac{A}{R}\exp(-kR)$, where $A = 1.725\,E_h$ and $k = 0.870\,a_0^{-1}$. Inset: Comparison of Heitler-London energy (black) to Lennard-Jones potential for the hydrogen triplet, $\sigma = 6.97\,a_0$, $\epsilon = 2.047 \times 10^{-5}\,E_h$ [14].

If the two electrons are considered charge distributions as described by I, H_1 is the energy of the repulsion of the two nuclei, the repulsion of the two charge distributions for each other, and the attraction of the charge distributions to both nuclei. This energy is repulsive at short range and attractive at long range; but at long range its attraction is much larger than that produced by H_0, and at short range its repulsion is smaller.

Because the energy depends on $H_0 - H_1$, the energy is repulsive for all R. The denominator, $1 - I^2$, expresses the fact that the electrons do not "want" to overlap, and so the potential becomes much more strongly repulsive at short range. The energy is plotted in figure 2.2. At very short ranges ($R < 0.2\,a_0$), the Taylor expansion about $R = 0$

$$E_T \approx \frac{a_0}{R} + 0.5 - 2\frac{R}{a_0}, \tag{2.23}$$

is a good approximation; for longer ranges

$$E_T \approx A\frac{e^{-kR}}{R} \tag{2.24}$$

is adequate. In the Lennard-Jones potential repulsion is approximated by

$$E_T \approx 4\epsilon\left(\frac{\sigma}{R}\right)^{12} \tag{2.25}$$

A major deficiency in the Heitler-London result is that at long range the potential is not attractive, as we saw that it should be in 2.2.1. In fact, experiments and more exact calculations [14] show that the potential has a minimum at about $7.8\,a_0$, as shown in figure 2.2. This minimum is too shallow to support a bound state for an atom of the mass of hydrogen, but it is just deep enough that atomic hydrogen can be condensed to a liquid, and that three tritium atoms (which interact with essentially the same potential) form a bound state [15]. While the Heitler-London result is far from perfect, it is accurate enough to demonstrate the nature of the effect.

The combination of exchange repulsion and van der Waals attraction accounts for nearly all of the two-body argon potential, and an accurate Ar-Ar potential from the literature [16] is shown in figure 2.3.

2.3 Many-body interactions

The Coulombic potential energy of a system of charged particles, such as electrons and nuclei, is the sum of potential energies between pairs of particles. However, in noble gases electrons are strongly associated with their own nucleus. Treating atoms as units, rather than charged particles, vastly simplifies the expression of the overall potential energy, as we have seen in section 2.2. The price of this simplification is that terms in

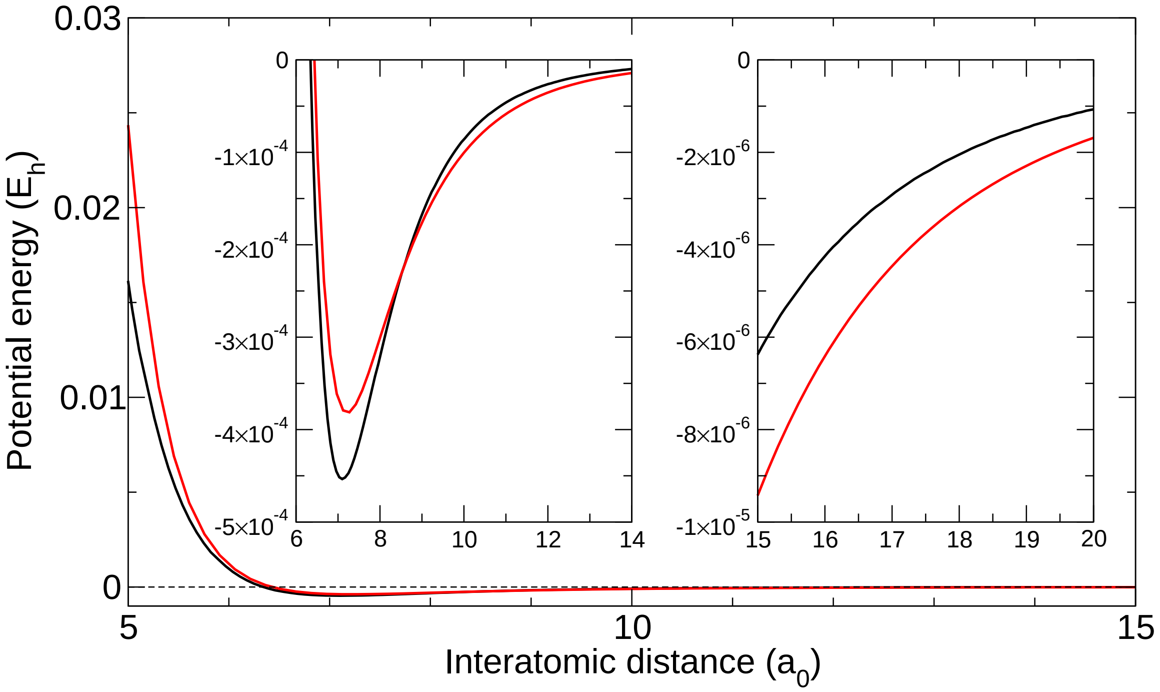

Figure 2.3: Black: Ar-Ar two-body potential. This is the HFD-C potential of Aziz and Chen [16], which combines the results of Hartree-Fock self-consistent field calculations with parameters determined by experiment. Red: Lennard-Jones potential [11]. Insets: differences at the minimum and at long range.

the overall potential energy depend not only on the configurations of pairs of atoms but of triple, quadruples and so forth.

It is easiest to understand this effect for a triple of atoms. The electronic configurations of two atoms will be distorted by each other, producing a two-body potential as described previously. Bringing in a third atom will distort the configurations of the other two, as well as its own, in ways not accounted for by the two-body potential. For example, two atoms very close together will look like two dipoles, and the potential experienced by the third atom will not be isotropic. But two atoms far apart will not distort each other much, and a third atom will expeience a potential very close to the sum of pair potentials, as illustrated in figure 2.4.

In a system of N atoms, there will be $\frac{1}{2}N(N-2)$ pairwise interactions. There

n N	1	2	3	4	5	6	7	8	9	10
1	1									
2	2	1								
3	3	3	1							
4	4	6	4	1						
5	5	10	10	5	1					
6	6	15	20	15	6	1				
7	7	21	35	35	21	7	1			
8	8	28	56	70	56	28	8	1		
9	9	36	84	126	126	84	36	9	1	
10	10	45	120	210	252	210	120	45	10	1

Table 2.2: Number of n-tuple interactions for system of N atoms.

will be $\frac{1}{6}N(N-1)(N-2)$ triple interactions, $\frac{1}{24}N(N-1)(N-2)(N-3)$ quadruples, and in general the number M of n-tuple particle interactions is given by the binomial coefficient:

$$M(n,N) = \frac{N!}{n!(N-n)!} = \frac{1}{n!}\prod_{1}^{n}(N-n+1) \tag{2.26}$$

The calculation up to $N = 10$, $n = 10$ is given in table 2.2. It is easy to see that the greatest number of interactions, M, is for the $N/2$-tuple. At this point we might despair of ever being able to calculate the potential energy of any but the smallest clusters of atoms. This is not the case for two reasons. First, potentials fall off with interatomic distance; second, atoms can only be brought so close together. The consequence is that only a tiny fraction of a given n-tuple need to be calculated for a cluster of N atoms; in the vast majority of cases at least one atom in the n-tuple will be too far away from the others to significantly affect them.

In practice, for neutral, spherical atoms, the typically significant n-body potential is the three-body potential. An example is the Axilrod-Teller three-body potential

$$V_{ijk} = C_{AT}\left(\frac{1 + 3\cos\gamma_i\cos\gamma_j\cos\gamma_k}{(r_{ij}r_{jk}r_{ik})^3}\right), \tag{2.27}$$

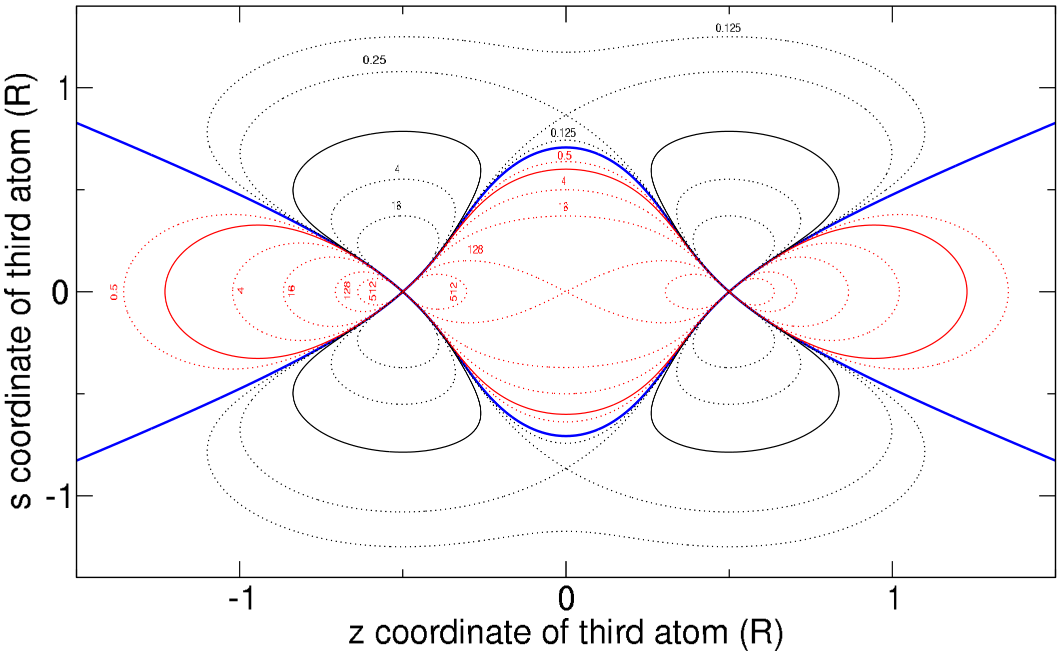

Figure 2.4: Contour plot of Axilrod-Teller potential. Contour lines indicate potential energy in units of C_{AT}/R^9, where R is the distance between atoms 1 and 2 (located at $z = \pm\frac{1}{2}R$). Blue line: zero energy. Red lines: attractive region, with the solid line indicating an energy of 1 C_{AT}/R^9. Black lines: repulsive region, with the solid line indicating an energy of 1 C_{AT}/R^9.

where i, j, k represent three atoms, r_{ij} the distance between atoms i and j, and γ_i the angle formed by the three atoms with atom i at the vertex [17]. It is calculated analogously to the two-body van der Waals interaction, using second-order perturbation theory (section 2.2.1). Note that this potential is not isotropic and is not always attractive (figure 2.4). Including a three-body potential typically lowers the energy of a system on the order of one percent. It often improves the accuracy of theoretical results, the effects becoming more important at higher pressures [18].

2.4 Bibliography

[1] L. Pauling. *The chemical bond*. Cornell University Press, 1967.

[2] J. E. Lennard-Jones. Cohesion. *The Proceedings of the Physical Society*, 43:461 – 482, 1931.

[3] J. C. Speakman. *A valency primer.* Edward Arnold (Publishers) Ltd., 1968.

[4] M. Gardener. *The annotated Alice: Alice's adventures in Wonderland & Tthrough the looking-glass by Lewis Carroll.* W. W. Norton and Company, 2000.

[5] J. Leonard, M. Walhout, A. P. Mosk, T. Müller, M. Leduc, and C. Cohen-Tannoudji. Giant helium dimers produced by photoassociation of ultracold metastable atoms. *Physical Review Letters*, 91:073203–1 – 073203–4, 2003.

[6] B. H. Brandsen and C. J. Joachain. *Physics of atoms and molecules.* Prentice-Hall, 2003.

[7] A. Messiah. *Quantum mechanics.* Dover Publications, Inc., 1999.

[8] J. E. Lennard-Jones. The quantum mechanics of atoms and molecules. *Journal of the London Mathematical Society*, s1-6 (4):290 – 318, 1931.

[9] C. Fischer. *The Hartree-Fock method for atoms: a numerical approach.* John Wiley and Sons, 1977.

[10] L. Pauling and J. Y. Beach. The van der Waals interaction of hydrogen atoms. *Physical Review*, 47:686–692, 1935.

[11] M. Marder. *Condensed matter physics.* John Wiley and Sons, 2000.

[12] W. Heitler and F. London. Wechselwirkung neutraler Atome und homopolare Bindung nach der Quantenmechanik. *Zeitschrift für Physik*, 44:455, 1927.

[13] J. C. Slater. *Quantum theory of molecules and solids.* McGraw-Hill Book Company, 1963.

[14] W. Stwalley and L. Nosanow. Possible “new” quantum systems. *Physical Review Letters*, 36:910–913, 1976.

[15] D. Blume, B. Esry, C. Greene, N. Klausen, and G. J. Hanna. Formation of atomic tritium clusters and bose-einstein condensates. *Physical Review Letters*, 89:163402–1 – 163402–4, 2002.

[16] R. Aziz and H. Chen. An accurate intermolecular potential for argon. *Journal of Chemical Physics*, 67:5719–5726, 1977.

[17] B. M. Axilrod and E. Teller. Interactions of the van der Waals type between three atoms. *Journal of Chemical Physics*, 11:299–300, 1943.

[18] E. Pechenik, I. Kelson, and G. Makov. Many-body model of rare gases at high pressures. *Physical Review B*, 78:134109–1 – 134109–15, 2008.

Chapter 3

Fluid argon

Chapter 2 describes the nature of the interatomic interaction of argon. The principal features are that argon atoms repel at close range, attract at long range, and have no meaningful orientation with respect to one another. Furthermore, argon undergoes no chemistry except under extreme conditions not encountered in this work.

In principle, the behavior of a substance in bulk can be deduced from precise knowledge of its interatomic interactions [1–4]. In practice, the problem is mathematically intractable, even if the interatomic interactions are very well known. Furthermore, interatomic interactions are not directly observable. However, in the case of argon many simplifying approximations and assumptions exist, due to the simple nature of its interatomic interactions. In this chapter we indicate how the interatomic interactions are connected with bulk properties of the fluid, so that knowledge of one can shed light on the other.

3.1 Classical or quantum mechanics?

One of the first simplifying assumptions for argon is that of classical behavior. While all of the noble gases share a similarly-shaped potential, helium and neon show more

Element	Mass (m_e)	ϵ (E_h)	σ (a_0)	η (0 K)	$\Lambda/\bar{a}$ (300 K)
Helium	7297	3.16×10^{-5}	4.84	0.430	0.0146
Neon	36790	1.14×10^{-4}	5.18	0.094	0.0065
Argon	72820	3.82×10^{-4}	6.43	0.030	0.0046

Table 3.1: Comparison of the quantumness of noble gases. Lennard-Jones parameters taken from Marder [5].

pronounced quantum behavior; in the case of helium spectacularly so. There is more than one way of characterizing the "quantumness" of a system.

One estimate of quantumness is given by calculating the quantum parameter η. If we assume a pairwise Lennard-Jones interaction for helium, neon, and argon, then we can write the quantum Hamiltonian for N atoms as

$$\hat{H} = -\frac{\hbar^2}{2m}\sum_{i=1}^{N}\nabla_i^2 + \sum_{i\neq j}^{N} 4\epsilon\left[\left(\frac{\sigma}{r_{ij}}\right)^{12} - \left(\frac{\sigma}{r_{ij}}\right)^{6}\right]; \tag{3.1}$$

where r_{ij} is the distance between atoms i and j, and σ and ϵ are the range and well depth of the Lennard-Jones interaction. We can rewrite the Hamiltionian dimensionlessly by replacing the Cartesian coordinates q_i with with $\tilde{q}_i\sigma$ and dividing through by the well depth:

$$\frac{1}{\epsilon}\hat{H} = -\frac{1}{2}\eta^2\sum_{i=1}^{N}\nabla_i^2 + \sum_{i\neq j}^{N} 4\left(\tilde{r}_{ij}^{-12} - \tilde{r}_{ij}^{-6}\right) \tag{3.2}$$

$$\eta^2 \equiv \frac{\hbar^2}{m\epsilon\sigma^2} \tag{3.3}$$

The quantum parameter η is a measure of the ratio of the kinetic energy at zero temperature to potential energy, and as $\eta \to 0$ the system exhibits classical behavior. Values of η for helium, neon and argon are given in table 3.1.

Another estimate of quantumness is given by calculating the *thermal de Broglie* *wavelegth* Λ, defined as [2]:

$$\frac{1}{\Lambda} \equiv \frac{1}{h} \int_{-\infty}^{\infty} \exp\left(-\frac{p^2}{2mkT}\right) dp = \left(\frac{2\pi mkT}{h^2}\right)^{1/2}; \tag{3.4}$$

where h is Planck's constant, used here to make the integral dimensionless (first used for this purpose by Josiah Willard Gibbs, years before Planck [1]). We can compare this wavelength to a crude measure of interatomic separation

$$\bar{a} \equiv \rho(T)^{-1/3} = \left(\frac{V}{N}\right)^{1/3}, \tag{3.5}$$

where $\rho(T)$ is the number density; we require that

$$\frac{\Lambda}{\bar{a}} << 1 \tag{3.6}$$

for classical behavior. Values of $\frac{\Lambda}{\bar{a}}$ for helium, neon, and argon at 300 K are found in table 3.1.

3.2 The partition function

The partition function is the bridge between statistical mechanics and thermodynamics. Once we have decided that we have a classical substance of N atoms described by the classical Hamiltonian $\hat{H}(p_{x_1}, p_{y_1}, p_{z_1}, x_1, y_1, z_1, \ldots, , p_{xN}, p_{yN}, p_{zN}, x_N, y_N, z_N)$ all that remains is to calculate the partition function [1]

$$Z = \frac{1}{h^{3N} N!} \int \int e^{-\frac{1}{kT}\hat{H}} \prod_{i=1}^{N} dx_i\, dy_i\, dz_i\, dp_{x_i}\, dp_{y_i}\, dp_{z_i}, \tag{3.7}$$

where h is Planck's constant and $N!$ accounts for classical indistiguishability of atoms. Because the potential energy of the system is velocity independent we can integrate over the momenta:

$$Z = \frac{1}{N!\Lambda^{3N}} \int e^{-\frac{1}{kT} V(x_1,y_1,z_1,\ldots,,x_N,y_N,z_N)} \prod_{i=1}^{N} dx_i\, dy_i\, dz_i = \frac{1}{\Lambda^{3N}} Z_Q; \tag{3.8}$$

where Λ is the thermal de Broglie wavelength defined in equation 3.4, $V(x_1, y_1, z_1, \ldots, , x_N, y_N, z_N)$ is the potential energy of the system, and Z_Q is the *configurational partition function.*

This is of course where it gets hard; if we assume the potential is zero we recover the ideal gas equations. However, in considering real gases, as well as liquids and solids, we have to incorporate the short-range repulsion and long-range attraction of real atoms. This implies that we must find some way of dealing with equation 3.8.

In the gas phase, the potential energy term can be considered a small correction to the kinetic energy term. In the solid phase, the kinetic energy term is considered a small correction to the potential energy term; usually by considering atoms in a solid to vibrate harmonically in a crystal lattice. Gases are disordered, and solids exhibit large-scale order. Liquids are characterized by order at atomic scales, and disorder at large scales. Each atom feels mostly repulsion from its nearest neighbors, with the attractive force it feels averaged over the volume. Thus the microscopic picture of a liquid is much like carelessly packing spheres, and in fact careless packing of spheres has been used to study the structure of liquids [6]. Liquids have the worst of both worlds, and are poorly approximated by solid-like and gas-like models [2–4].

This work is primarily concerned with supercritical argon. We take the behavior of solid argon as given, and are especially interested in the fluid as it condenses to the solid. Because there is no phase transition in the fluid region, we can think of it as behaving at low densities like a gas and at high densities like a liquid, with a smoothly-varying transition from low density to high density.

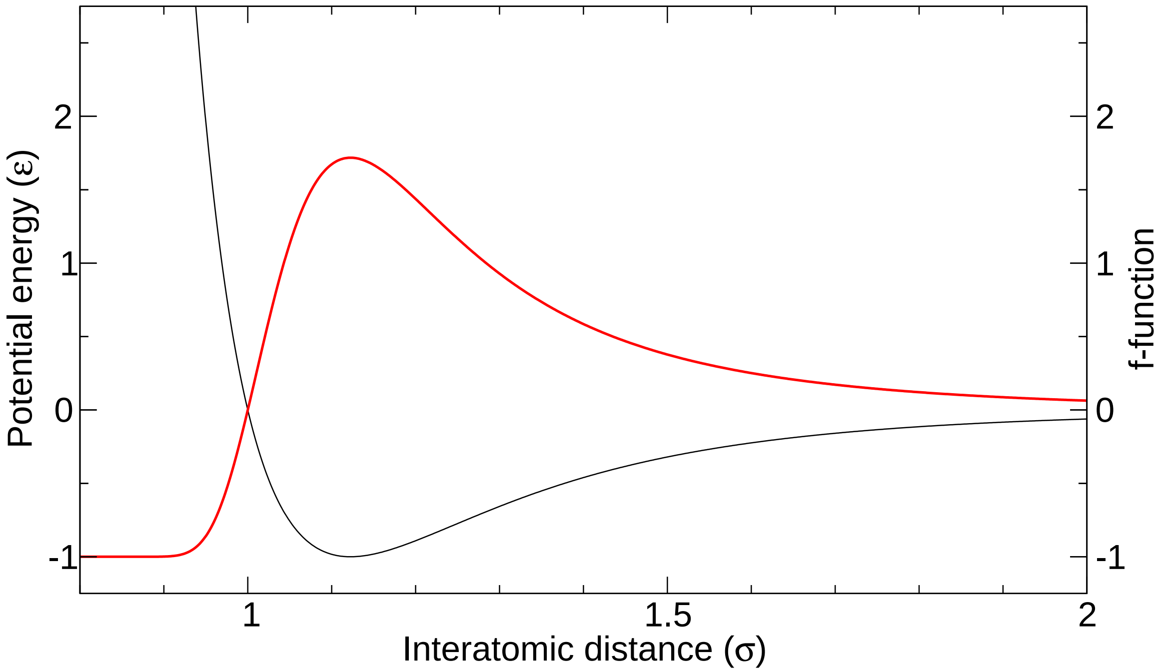

Figure 3.1: Lennard-Jones potential (black) and Mayer f-function (red). The f-function is temperature dependent; the one shown here is $kT = \epsilon$.

3.3 The virial equation of state

One simplification, appropriate for argon and the heavier noble gases, is to assume that the total potential energy is the sum of pairwise interactions. Rewriting equation 3.8 accordingly yields

$$Z = \frac{1}{N!\Lambda^{3N}} \int \exp\left(\frac{1}{kT} \sum_{i=1}^{N-1} \sum_{j=i+1}^{N} V(r_{ij})\right) \prod_{i=1}^{N} d\tau_i, \tag{3.9}$$

where $V(r_{ij})$ represents the pair potential, $r_{ij}^2 = (x_i - x_j)^2 + (y_i - y_j)^2 + (z_i - z_j)^2$ is the interatomic distance between atoms i and j, and $d\tau_i = dx_i dy_i dz_i$.

Now we introduce the *Mayer f-function* [2], shown for the Lennard-Jones potential in figure 3.1:

$$f_{ij} = \exp\left(-\frac{V(r_{ij})}{kT}\right) - 1 \tag{3.10}$$

This is the sort of thing we are looking for; it describes atoms as refusing to get very close together, and at the same time indifferent to atoms that are far away, which is one of the properties of liquids. Rewriting the partition function in terms of the f-function gives

$$Z = \frac{1}{N!\Lambda^{3N}} \int \prod_{i=1}^{N-1} \prod_{j=i+1}^{N} (f_{ij} + 1) \prod_{i=1}^{N} d\tau_i, \tag{3.11}$$

We can expand the integrand into a series:

$$\prod_{i=1}^{N-1} \prod_{j=i+1}^{N} f(r_{ij}) + 1 = 1 + \sum_i \sum_j f_i j + \sum_i \sum_j \sum_k \sum_l f_{ij} f_{kl} + \ldots \tag{3.12}$$

If we treat all atoms as being in the bulk, and not on the surface, then this series can be rearranged into terms that represent pairs, triples, quadruples, and so on:

$$Z = \frac{1}{N!\Lambda^{3N}} \int 1 + \frac{1}{2}\frac{N!}{(N-2)!} \text{ pairs } + \frac{1}{6}\frac{N!}{(N-3)!} \text{ triples } + \ldots \frac{1}{n!}\frac{N!}{(N-n)!} \text{ n-tuples } \ldots \prod_{i=1}^{N} d\tau_i \tag{3.13}$$

We can carry out this integral termwise:

$$Z = \frac{1}{N!\Lambda^{3N}} \left(V^N + \frac{1}{2}\frac{N!}{(N-2)!} V^{N-1} I_2 + \frac{1}{6}\frac{N!}{(N-3)!} I_3 + \ldots \frac{1}{n!}\frac{N!}{(N-n)!} V^{N-n} I_n \ldots \right) \tag{3.14}$$

where the terms I_n represent the *cluster integrals.* Of course, evaluating the cluster integrals is the hard part. They are not even straightforward to write down, except for the pair and the triple:

$$I_2 = \int f_{12}\, d\tau_2, \tag{3.15}$$

$$I_3 = \int \int f_{12} f_{23} f_{31} d\tau_2 d\tau_3, \tag{3.16}$$

with higher n-tuples classified and described according to a pictorial notation reminiscent of Feynman diagrams.

Once we have calculated as many terms of the partition function as we decide we require, we use the thermodynamic relation

$$P = kT \left(\frac{\partial \log Z}{\partial V} \right)_T , \tag{3.17}$$

and this, coupled with the Stirling approximation for large N, produces the *virial equation of state*

$$P = \frac{NkT}{V} \left(1 - \frac{N}{V} B_2(T) - \frac{N^2}{V^2} B_3(T) ... \right) \tag{3.18}$$

with $B_n(T) = \frac{1}{n!} I_n$ is the *virial coefficient.* One can immediately see that if they are negligible we recover the ideal gas law, and the van der Waals equation of state can be written in this form by expanding it in powers of N/V.

Our triumph is not yet complete, as there are two serious concerns to address. First is the difficulty of calculating the virial coefficients; in practice six or seven is the limit. Second is the problem of convergence; it is not known under what conditions the series defined by the coefficients will converge. All that one can do is keep the density small, and the virial equation of state is not very accurate except for gas-like fluids. To extend the virial equation of state to liquid-like densities would require calculating a large number of coefficients, which cannot be done in practice [2–4].

It is instructive nonetheless to calculate some of the simpler virial coefficients for simple, realistic potentials such as the Lennard-Jones potential. Then the virial coefficients can be measured experimentally and used to work out the values of σ and ϵ for the Lennard-Jones potential. This is useful because interatomic potentials are not directly observable.

$$B_2(T) = -\frac{1}{2} \left\{ 4\pi \int_0^\infty r^2 \left[\exp \left(- \frac{4\epsilon \left(\frac{\sigma^{12}}{r^{12}} - \frac{\sigma^6}{r^6} \right)}{kT} \right) - 1 \right] dr \right\} \tag{3.19}$$

The Lennard-Jones potential is positive for $r < \sigma$ and negative for $r > \sigma$, which provides a natural place at which to break the integral. For $r < \sigma$ the f-function is very closely approximated by -1, as shown in figure 3.1, yielding

$$B_2(T) \approx \frac{1}{2}\left\{\frac{4}{3}\pi\sigma^3 + 4\pi\int_\sigma^\infty r^2\left[\exp\left(-\frac{4\epsilon\left(\frac{\sigma^{12}}{r^{12}} - \frac{\sigma^6}{r^6}\right)}{kT}\right) - 1\right] dr\right\}. \tag{3.20}$$

Another approximation, that of high temperature, is useful here. For argon, ϵ/k is 120 K [3], and so for temperatures above that we can approximate the integrand:

$$B_2(T) \approx \frac{1}{2}\left\{\frac{4}{3}\pi\sigma^3 - 4\pi\int_\sigma^\infty r^2\frac{4\epsilon\left(\frac{\sigma^{12}}{r^{12}} - \frac{\sigma^6}{r^6}\right)}{kT}\, dr.\right\}, \tag{3.21}$$

which is easy enough to evaluate:

$$B_2(T) \approx \frac{1}{2}\left(\frac{4}{3}\pi\sigma^3 - \frac{32}{9}\pi\sigma^3\frac{\epsilon}{kT}\right) = \frac{1}{2}V_0\left(1 - \frac{8}{3}\frac{\epsilon}{kT}\right), \tag{3.22}$$

where $V_0 = \frac{4}{3}\pi\sigma^3$ can be thought of as the volume of one atom.

We can see from this expression that there is a temperature at which we recover ideal gas behavior, the *Boyle temperature*, T_B, at which $B_2(T) = 0$. The estimate of $B_2(T)$ given by equation 3.22 yields $T_B = \frac{8}{3}\frac{\epsilon}{k}$, corresponding to 320 K for argon, but more accurate evalutions of equation 3.19 give $T_B = 3.42\frac{\epsilon}{k}$ for the Lennard-Jones potential [3]. This corresponds to about 400 K for argon.

Since most interatomic and intermolecular potentials have some kind of attractive well and some kind of repulsive radius, this gives rise to the *law of corresponding states* for gases [1], which allows one to scale the estimates of $B_n(T)$ by the appropriate parameters for the particular gas one is interested in, and get approximately accurate results for the equation of state.

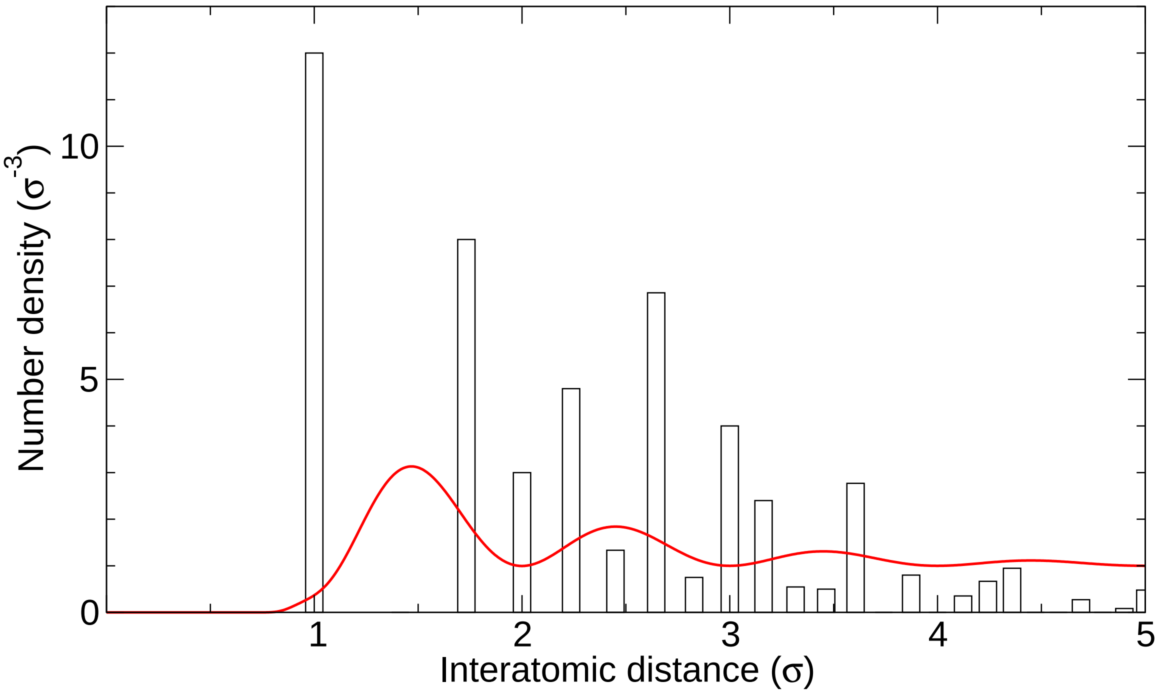

Figure 3.2: Schematic pair distribution function for a liquid (red line) compared to the analogous construction for an fcc solid (black bars). The height of the bars is the number of neighbor atoms a distance r from one atom at zero; divided by r^2, so that integration yields the total atoms in the volume around the central atom. Ideally the solid pair distribution function would be a set of delta functions. The liquid pair distribution function is normalized to 1 as $r \to \infty$, describing the lack of correlation at long range.

3.4 The pair distribution function

If the *pair distribution function* is also known, the equation of state of pairwise-interacting atoms can be written more simply [2–4]:

$$P = \rho kT - \frac{4\pi\rho^2}{6}\int_0^\infty g(r)\frac{dV}{dr}r^3\,dr, \tag{3.23}$$

where ρ is the number density N/V, $V(r)$ is the pair potential, and $g(r)$ is the pair distribution function. A schematic of a pair distribution function for a liquid is given in figure 3.2, along with an analogous construction for an fcc solid.

The pair distribution function, when integrated over the whole volume, is related to the density by

$$\frac{4\pi}{N-1}\rho\int_0^\infty g(r)r^2\,dr = 1. \tag{3.24}$$

But the pair distribution function is accessible experimentally, as the Fourier transform of the structure factor, $S(k)$, determined from scattering and diffraction experiments.

The calculation of $g(r)$ from an interatomic potential, however, is no more tractable than the calculation of the virial coefficients. $g(r)$ can be derived through the configurational partition function, Z_Q (equation 3.8):

$$\rho^2 g(r) = \frac{1}{(N-2)!Z_Q}\int \exp\left(-\frac{V(x_1,y_1,z_1,\ldots,x_N,y_N,z_N)}{kT}\right)\prod_{i=3}^{N} d\tau_i, \tag{3.25}$$

which involves two intractable integrals. Another approach is to write the pair distribution function in terms of an integral over the *triple distribution function*, which in turn can be written over an integral over the *quadruple distribution function*, and so on unto the *N-tuple distribution function.* This approach works by assuming something simple for the triple or quadruple distribution function and truncating the recursion [2].

3.5 The hard-sphere model

Unlike atoms in a solid, which sit in a potential minimum produced by the interactions of their nearest neigbors, the atoms in a liquid have enough kinetic energy that their interactions with their neighbors are primarily repulsive. The attractive forces that make the collection of atoms liquid-like rather than gas-like are smeared out over the entire volume. Consequently, the *hard-sphere model*, where atoms have no attractive interaction at all, produces surprisingly accurate results for the bulk; however, hard spheres do not show a transition between liquid and gas [2–4].

The hard sphere model represents the interatomic potential, $V(r)$, by

$$V(r) = \begin{cases} \infty, & r \; < \; \sigma \\ 0, & r \; \geq \; \sigma \end{cases} . \tag{3.26}$$

Of course this is analytically much more tractable, and at least eight virial coefficients have been calculated for hard spheres [7].

The structure of hard-sphere fluids is characterized by approximately five-fold symmetry [6], which of course cannot fill space the way regular lattices can. Although hard spheres do not have any attractive forces built in, they do exhibit an effective attraction due to collisional shielding [2–4].

A semi-empirical equation of state for the hard sphere fluid, the Carnahan-Starling equation of state, is given by

$$\frac{PV}{NkT} = \frac{1 + \eta + \eta^2 - \eta^3}{(1 - \eta)^3} \tag{3.27}$$

where $\eta = \frac{1}{6}\pi\rho\sigma^3$, which for a close-packed structure would be $\frac{\sqrt{2}}{6}\pi$.

3.6 Numerical and experimental results

Argon may be the most extensively studied substance in existence. We hope that the references given below constitute a representative sample.

The equation of state of argon has been calculated by a variety of methods for a wide range of temperatures and pressures. These include Monte Carlo simulation [8, 9]; molecular dynamics simulation [10, 11], directly from the interatomic potential via significant structure theory [12], the embedded atom method [13], and the configurational

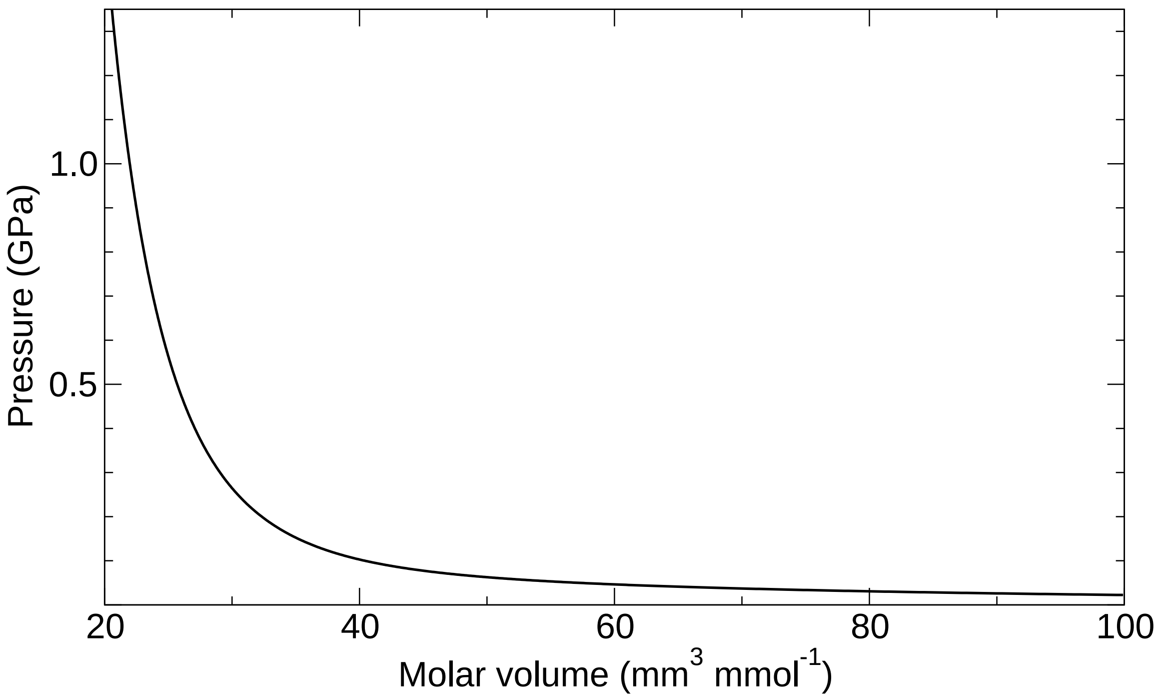

Figure 3.3: Experimentally derived equation of state for fluid argon at 300 K.

partition function [14]; from total energy calculations [15]; from the corresponding states principle [16]; from density functional theory [17], from mean-field theory [18].

There have been many experimental measurements of the equation of state. For the solid, X-ray diffraction [19–22]. For the fluid, using metal bellows [23] and piston-cylinder apparatus [24, 25], and through Brillouin scattering if properties such as refractive index are known [26].

Empirical equations of state are also generated from experimental results, from thermodynamic properties such as pressure, density, temperature, isothermal compressibility, triple and critical points, heat capacities, etc. IUPAC produced a book-length set of tables for argon up to pressures of 0.1 GPa [27] in 1972. A more recent one for fluid argon [28] at 300 K is shown in figure 3.3; it draws on about 180 references.

Other thermodynamic properties such as elastic moduli, melting lines, structural properties, along with those listed above, have been calculated from the interatomic potential; and the interatomic potential has in turn been calculated from measurements of those properties [11, 17, 29–37].

3.7 Bibliography

[1] H. Callen. *Thermodynamics and introduction to thermostatistics.* John Wiley and Sons, 1985.

[2] Clive A. Croxton. *Introduction to liquid state physics.* John Wiley and Sons, 1975.

[3] Jean P. Hansen and Ian R. McDonald. *Theory of simple liquids.* Academic Press, Inc., 1986.

[4] N. H. March and M. P. Tosi. *Atomic dynamics in liquids.* The Macmillan Press Ltd., 1976.

[5] M. Marder. *Condensed matter physics.* John Wiley and Sons, 2000.

[6] J. D. Bernal. The structure of liquids. *Proceedings of the Royal Society of London A*, 280:299–322, 1962.

[7] E. J. Janse van Rensburg. Virial coefficients for hard disks and hard spheres. *Journal of Physics A*, 26:4805–4818, 1993.

[8] A. E. Nasrabad. Monte Carlo simulations of thermodynamic and structural properties of Mie(14,7) fluids. *Journal of Chemical Physics*, 128:154514–1 – 154514–7, 2008.

[9] J. Barker. High pressure equation of state for solid argon from interatomic potentials. *Journal of Chemical Physics*, 67:1509–1511, 1987.

[10] F. Cuadros and W. Ahumada. Accurate analytical expressions of thermodynamic properties of supercritical lennard-jones fluids. *Thermochimica Acta*, 297:109–116, 1997.

[11] A. Belonoshko. Equation of state and melting transition of argon up to 8000K and 4Mbar: a molecular dynamics study. *High Pressure Research*, 10:583–597, 1992.

[12] C. T. Tung, G. E. Duvall, and W. Band. Modification of the significant structure theory of liquids for argon at high pressures and temperatures. *Journal of Chemical Physics*, 52:5252–5260, 1970.

[13] E. Pechenik, I. Kelson, and G. Makov. Many-body model of rare gases at high pressures. *Physical Review B*, 78:134109–1 – 134109–15, 2008.

[14] M. Bobetic and J. Barker. Solid state properties of argon, krypton, and xenon near 0 K from an $[n(r)]$-6 potential. *Physical Review B*, 28:7317–7320, 1983.

[15] I. Kwon, L. A. Collins, and J. D. Kress. First-principles study of solid Ar and Kr under high compression. *Physical Review B*, 52:15165 – 15169, 1905.

[16] G. Ihm, Y. Song, and E. Mason. A new strong principle of corresponding states for nonpolar fluids. *Journal of Chemical Physics*, 94:3839–3848, 1991.

[17] J. Tse, D. Klug, V. Shpakov, and J. Rodgers. High pressure elastic properties of solid argon from first-principles density functional and quasi-harmonic lattice dynamic calculations. *Solid State Communications*, 122:557–560, 2002.

[18] K. Leonhard and T. Kraska. An equation of state describing the critical region: extension to high pressure. *Journal of Supercritical Fluids*, 99:1–10, 1999.

[19] D Errandonea, R Boehler, S Japel, M Mezouar, and LR Benedetti. Structural transformation of compressed solid Ar: An x-ray diffraction study to 114 GPa. *Physical Review B*, 73:092106–1 – 092106–4, 2006.

[20] A. Jephcoat. Rare gas solids in the earth's deep interior. *Nature*, 393:355–358, 1998.

[21] M. Ross, H. K. Mao, P. M. Bell, and J. Xu. The equation of state of dense argon: a comparison of shock and static studies. *Journal of Chemical Physics*, 85:1028–1033, 1986.

[22] L. W. Finger, R. M. Hazen, G. Zou, H. K. Mao, and P. M. Bell. Structure and compression of crystalline argon and neon at high pressure and room temperature. *Applied Physics Letters*, 39:892–894, 1981.

[23] S. Robertson, S. Babb, and G Scott. Isotherms of argon to 10000 bars and 400 C. *Journal of Chemical Physics*, 50:2160–2166, 1969.

[24] D. Liebenberg, R. Mills, and J. Bronson. Apparatus for compressibility measurements: Data on argon to 13 kbar. *Journal of Applied Physics*, 45:741–747, 1974.

[25] M. Anderson and C. Swenson. Experimental equations of state for the rare gas solids. *Journal of Physics and Chemistry of Solids*, 36:145–162, 1975.

[26] R. Jia, F. Li, M. Li, Q. Cui, Z. He, L. Wang, Q. Zhou, T. Cui, G. Zou, Y. Bi, S. Hong, and F. Jing. Brillouin scattering studies of liquid argon at high temperatures and pressures. *Journal of Chemical Physics*, 129:154503–1–154503–7, 2008.

[27] S. Angus and B. Armstrong, editors. *International Thermodynamic Tables of the Fluid State, Argon, 1971,IUPAC*. Butterworth's, 1972.

[28] Ch. Tegeler, R. Span, and W. Wagner. A new equation of state for argon covering the fluid region for temperatures from the melting line to 700 K at pressures up to 1000 MPa. *Journal of Physical Chemistry Reference Data*, 28:779–850, 1998.

[29] J. Eggert, G. Weck, P. Loubeyre, and M. Mezouar. Quantitative structure factor and density measurements of high-pressure fluids in diamond anvil cells by x-ray diffraction: argon and water. *Physical Review B*, 65:174105–1–174105–12, 2002.

[30] F. Datchi, P. Loubeyre, and R. LeToullec. Extended and accurate determination of the melting curves of argon, helium, ice (H_2O), and hydrogen (H_2). *Physical Review B*, 61:6535–6546, 2000.

[31] T. Pfleiderer, I. Waldner, H. Bertagnolli, K. Tödheide, B. Kirchner, H. Huber, and H. Fischer. The structure of fluid argon from high-pressure neutron diffraction and *ab initio* molecular dynamics simulations. *Journal of Chemical Physics*, 111:2641–2646, 1999.

[32] N. Wilding. Critical-point and coexistence-curve properties of the Lennard- Jones fluid: a finite-size scaling study. *Physical Review E*, 52:602–611, 1995.

[33] C. S. Zha, R. Boehler, D. Young, and M. Ross. The argon melting curve to very high pressure. *Journal of Chemical Physics*, 85:1034–1036, 1986.

[34] M. Ross. The repulsive forces in dense argon. *Journal of Chemical Physics*, 73:4445–4450, 1980.

[35] R. Teague and C. Pings. Refractive index and the Lorentz-Lorenz function for gaseous and liquid argon, including a study of the coexistence curve near the critical state. *Journal of Chemical Physics*, 48:4973–4984, 1968.

[36] I. Crivelli and F. Danon. The reduced equation of state of argon and xenon. *Journal of Physical Chemistry*, 71:2650–2653, 1967.

[37] J. S. Brown. Interatomic potential parameters of solid neon and argon. *Proceedings of the Physical Society*, 89:987–992, 1966.

Chapter 4

Experimental techniques

4.1 Diamond anvil cells

Diamond anvil cells (DACs) are used to apply high pressures [1]. Diamonds are very hard and also transparent to visible and infrared light [2, 3]. Consequently, not only can they be used to apply high pressures, but they are also well-suited for optical and spectroscopic measurements [1].

The diamonds used in a DAC, and typical DACs, are shown in figure 4.1. The DAC we used is a Merrill-Basset design [4]. The diamonds are attached to backing plates by five-minute epoxy. Setscrews hold the backing plates in the piston and cylinder; the setscrews allow for fine adjustment of the alignment of the diamonds. The diamonds apply pressure to a gasket, usually stainless steel. The gasket has a hole drilled in its center, typically half the diameter of the diamond culets. The sample goes in the hole, and if the sample is solid the hole is filled with a pressure medium such as water, argon, or an ethanol-methanol mixture. Typically a chip of ruby is also added to the hole for pressure measurements (section 4.1.5).

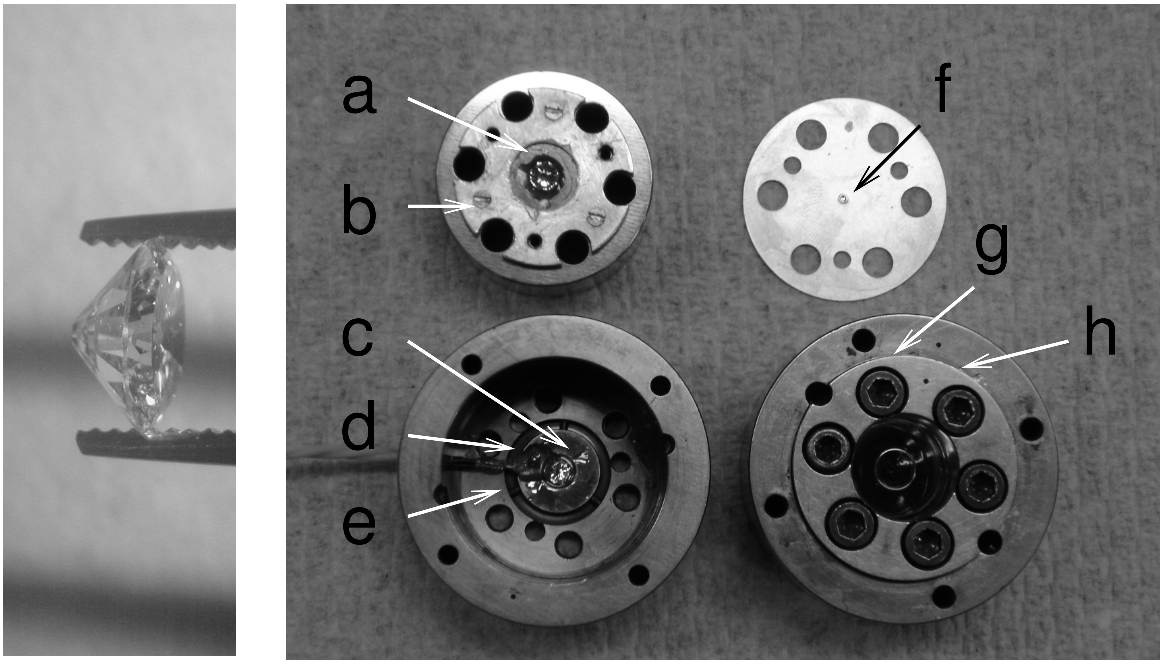

Figure 4.1: Left: Typical diamond, 600 μm diameter culet. Right: Parts of the DAC. Counterclockwise from top left: piston, cylinder, assembled DAC, gasket. a) Hemispherical backing plate with diamond. b) Setscrews for adjusting axial alignment. c) Disk backing plate with diamond. d) RTD for sensing temperature of DAC. e) Setscrew for adjusting alignment in plane. f) Preindentation in gasket. g) Allen screws for adjusting pressure. h) Reference marks.

4.1.1 Alignment

The backing plates and the tables of the diamonds were first cleaned, under a stereo microscope, with cotton swabs and methanol. It is critical that the tables and plates be smooth and clean, or the diamonds will shift under pressure and be more likely to fracture. The diamonds were then centered over the holes in the backing plates. Two small drops of five-minute epoxy were applied to opposite sides of the circumference of each diamond. Moderate pressure was applied to the culets, forcing the tables to make good contact with the backing plates. Then epoxy was applied all around the circumference of each diamond. Applied pressure kept the epoxy from seeping between the table and the plate. After twenty-four hours the diamonds and backing plates were

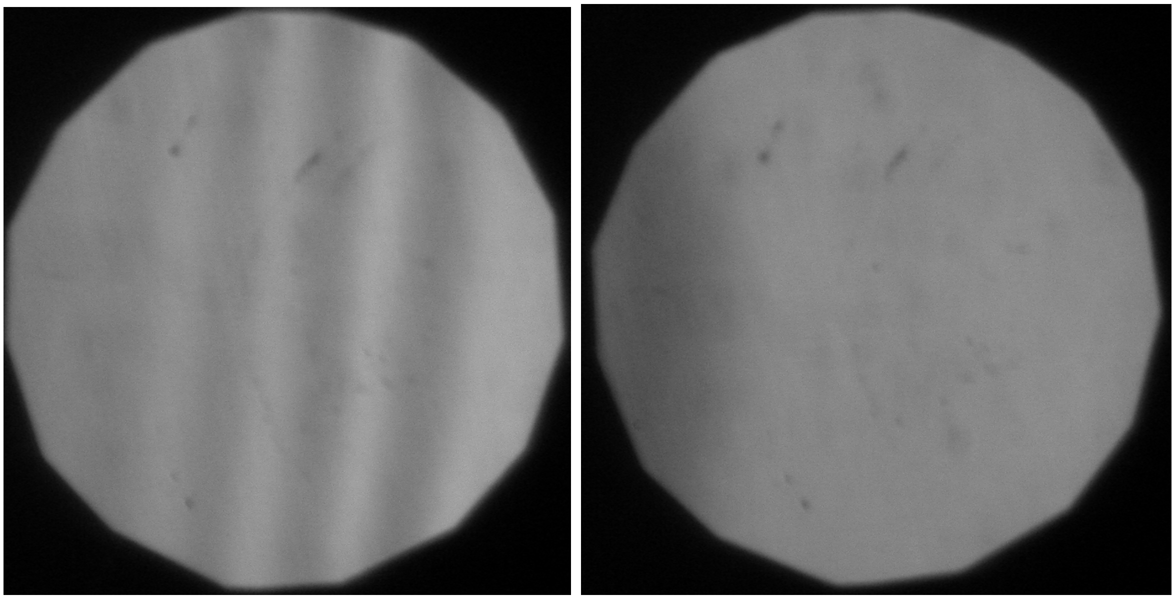

Figure 4.2: Left: Interference fringes due to slight misalignment of diamonds. Right: Corrected alignment.

removed and inspected. If epoxy had seeped in between the plate and the diamond, it would have been necessary to start over.

The receptacles for the backing plates, in the piston and cylinder, were then cleaned under the microscope with methanol and cotton swabs, as were the diamond culets. The backing plates were then inserted into the piston and cylinder. One plate is flat, and can move from side to side. The other plate is hemispherical, and can tilt. The setscrews were just tightened, and the piston was inserted into the cylinder, gently, so that the diamond culets were in contact. The reference marks on the piston and cylinder were then aligned. The Allen screws inserted and just tightened, taking care not to apply significant toruqe to the screw, and the alignment of the diamond culets was inspected under the microscope.

The circumferences of the culets must be aligned and the culets themselves made parallel. This was done by adjusting the setscrews. Interference fringes will be seen in the microscope if the culets are not parallel (figure 4.2). The setscrews were adjusted

	1	2	3	Δ_{12}	Δ_{13}
Aligned	107	105	109	-002	002
Goal	147	145	149	-002	002
Initial	247	242	251	-005	004
	242	241	243	-001	001
	238	236	240	-002	004
	...	...	...	...	...
	152	152	154	000	002
Final	148	145	150	-003	002

Table 4.1: A sample alignment and preindentation record. The units are ten-thousandths of an inch. Aligned: the measured thickness at three points when the diamonds are aligned. Goal: the desired measurements when the cell is preindented to the desired thickness (100 μm). Initial: the measurements when the gasket has been inserted but not preindented. Final: measurements after preindentation is completed.

until the circumferences matched up, and the fringes disappeared. Typically the fringes cannot be made entirely to disappear merely by adjusting setscrews. When the fringes were reduced to one or two very broad bands, they were eliminated entirely by very slight tightening of the Allen screws that push the piston against the cylinder. Excessive tightening of the Allen screws will of course break the diamonds.

After aligning the diamonds, the alignment was recorded. This was done by applying a dial indicator to three points on the piston, and recording the thickness of the cell to the ten-thousandth of an inch (figure 4.3). The relative differences between the measurements constitute the record of the alignment (table 4.1). (The absolute measurements were used when the gasket was preindented.) This alignment was maintained any time the Allen screws were adjusted. If the culets get significantly out of true while pressure is applied, the diamonds will fracture. If the differences between the measurements should be more than three or four ten-thousandths, then there may be something wrong with the cell, such as foreign material under a backing plate.

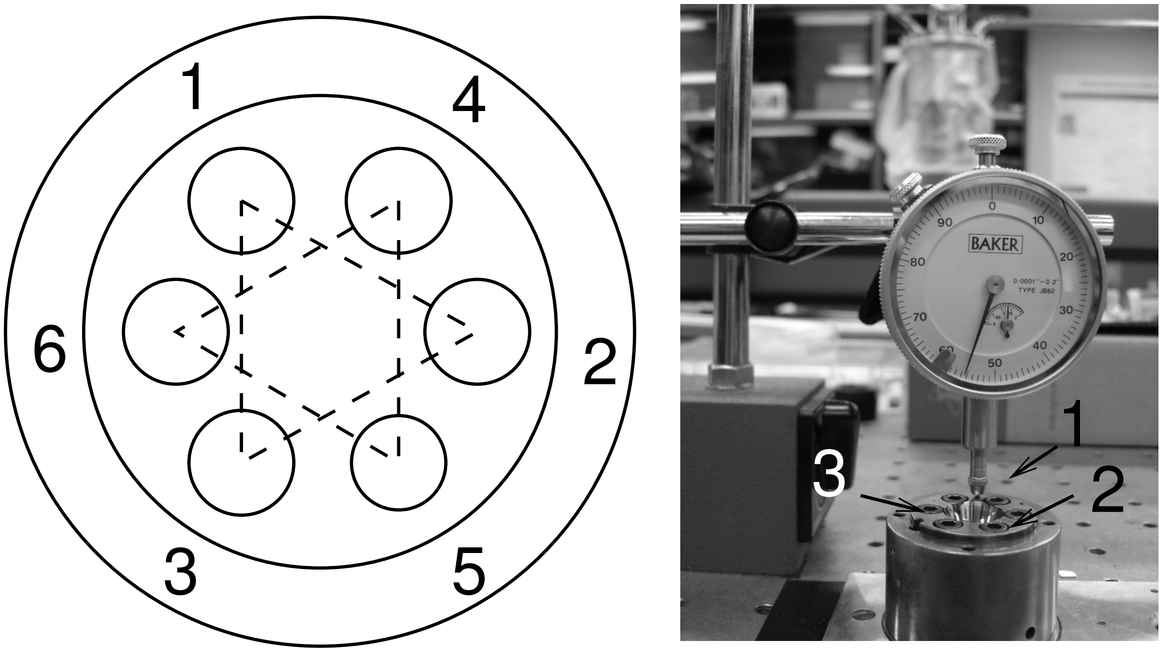

Figure 4.3: Left: Order in which Allen screws are tightened. Right: Measuring the thickness of the DAC in three locations using the dial indicator.

4.1.2 Gasket preparation

The gaskets used in these experiments were #304 stainless steel, 0.25 mm thick. Other materials can be used, depending on the desired pressures. In general, harder materials go to higher pressures, although very hard materials increase the risk of fracturing the diamonds.

The gasket was first preindented. The Allen screws were removed and the piston removed from the cylinder. The gasket was marked, so that it could be reoriented correctly. (If a resistance temperature detector, described in section 4.1.6, was affixed to the backing plate a wedge was out of the gasket to provide clearance.) The gasket was centered on the culet and clay somtimes used to help keep it in place. The piston was then inserted and both diamonds made contact with the gasket. The Allen screws were reinserted and just tightened. The alignment was measured, and compared to the recorded alignment. The Allen screws were tightened, in small increments, to bring the

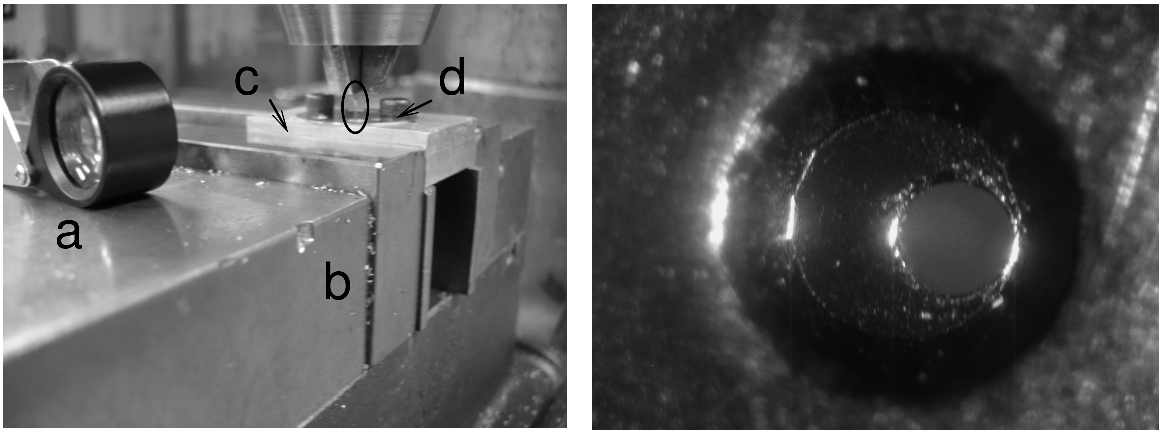

Figure 4.4: Left: Setup for drilling the hole in the preindented gasket. a) hand lens for alignment. b) vise of milling machine. c) jig. d) gasket clamped to jig with Allen screws. Circled: drill bit. Right: A barely adequate hole; it does not quite touch the sides of the indentation.

cell into the recorded alignment. When the cell was level again, the Allen screws were tightened in a “Magen David” pattern (figure 4.3). The alignment was checked, the cell was leveled again, and so forth, until the desired preindentation was reached. This was judged by comparing the dial indicator measurements of the aligned cell (section 4.1.1) with the dial indicator measurements of the preindented gasket.

Thinner gaskets will support higher pressures. For these experiments preindentations typically were between 100 microns and 150 microns. Because the gasket expands when pressure is released, a preindented gasket will be thicker than the dial indicator measurements would suggest.

The gasket was then drilled. The diameter of the hole was about half that of the diamond culets. (In this work 0.7 mm culets were drilled to 0.29 mm, and 1 mm culets to 0.45 mm.) The gasket was clamped in a jig, and the jig was placed in the vise of a milling machine. The drill bit was placed in the milling machine and brought down just above the preindentation. As shown in figure 4.4, using a 10X hand lens, the X position of the jig was adjusted until the bit appeared to be centered in the preindentation. This is most easily done if the bit is brought so close that its reflection can be seen in the preindentation; it then appears as a line bisecting an ellipse, as shown in the figure. Once the bit was centered in the X direction it was then centered in the Y direction. Once the bit was aligned in both directions, the hole was drilled by bringing the bit down very slowly (taking about one second to push through the gasket).

Once the hole was drilled it was examined under the microscope, and burrs removed by a needle. The hole need not be exactly centered but it must not touch the edges of the indentation (figure 4.4).

4.1.3 Loading at ambient temperature

DACs are often loaded with a pressure medium such as water. Loading at ambient temperature was as follows. First the gasket was placed on the cylinder diamond. The sample and ruby chip (if desired) were placed in the hole with a needle. The liquid is then placed in the gasket with a dropper. Air bubbles were removed with a needle. Sometimes the liquid did not get between the bottom diamond and the gasket, and air bubbles would appear after the piston was pressed onto the gasket. In this circumstance they were removed by raising the piston off the gasket and replacing it. In the most difficult cases it was necessary to lift the gasket off the bottom diamond and wiggle it to get all the air out. It was necessary that the gasket and culets be very clean because the liquid would spread out and pick up foreign material, and when the cell was sealed this foreign material could be trapped in the cell.

4.1.4 Cryogenic loading

Techniques and equipment exist to load argon at ambient temperature, but in this work we did not use them. Instead, liquid argon was used.

For Fourier transform infrared spectroscopy, carbon dioxide was introduced into the argon. This was done by running carbon dioxide vapor into the dewar that contains

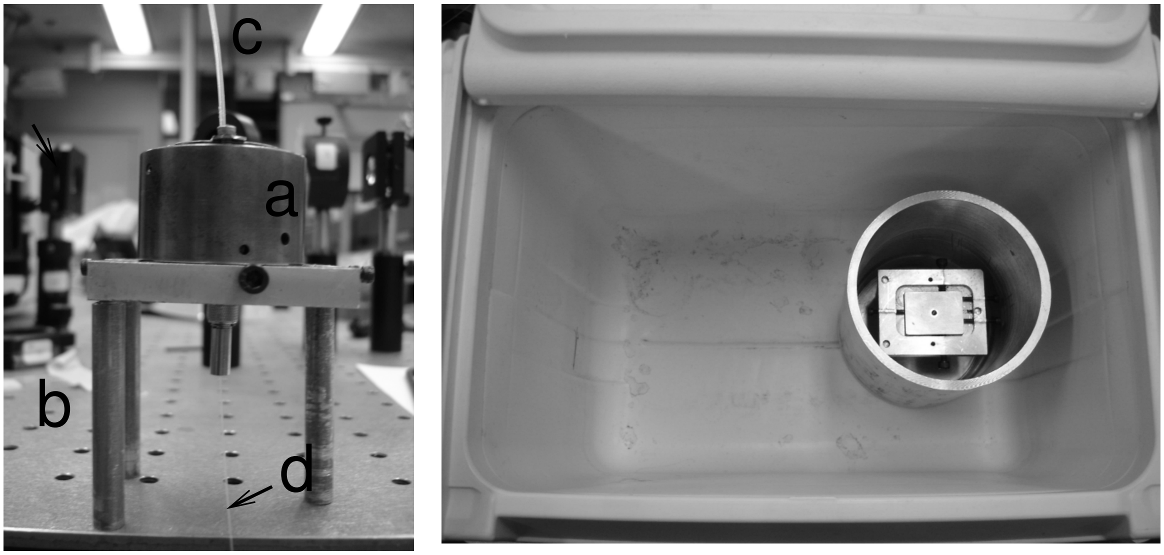

Figure 4.5: Left: Stage for cryogenic loading. a) DAC. b) stage. c), d) optical fibers for monitoring pressure *in situ* (optional). Right: Coleman cryogenic loading chamber and aluminum cylinder with stage inserted.

the liquid argon for at least one half hour, until the liquid argon had the appearance of milk. This was done before loading argon into the cell.

After the gasket was drilled and a ruby chip and sample placed in the hole, the piston was inserted and the Allen screws were just tightened. The cell was then inverted, so that the weight of the piston came off the gasket. The piston setscrews were tightened just enough to hold the piston in place. The cell was then attached to a stage we constructed specially, shown in figure 4.5. If it was desired to load the cell to a high pressure, a set of fibers was attached to the stage and cell to monitor the pressure while loading.

The stage was inserted in a specially constructed aluminum cylinder. The cylinder was placed in a cryogenic loading chamber manufactured by Coleman. The cylinder was placed near one side of the chamber. Liquid nitrogen was then slowly poured into the chamber, taking care not to splash nitrogen into the cylinder. When the level of the nitrogen was about halfway up the cylinder, and any nitrogen in the cylinder had boiled out, then liquid argon was poured into the cylinder until the cell was immersed to the depth of about half an inch. (Liquid nitrogen and liquid argon are miscible, so it is important to keep them separate to avoid contamination.) Argon boiled out as the cell and stage cooled, so more argon was poured in to keep the cell covered. After a minute or two the argon settled down, and small bubbles came out of the cell. At this time, the Allen wrench was placed in the argon, resting on the stage, to cool.

About five minutes after the last bubble, the Allen screws were tightened. Each screw was torqued until it just gaves. If low pressures were desired, 2 - 5 times around the pattern were sufficient. If higher pressures were desired, then we went around the pattern until the ruby peak had shifted by the desired amount (section 4.1.5). If at any time the ruby signal disappears, one must stop immediately; this indicates that no argon is in the hole and it has collapsed, and the diamonds are in danger of fracture.

Liquid nitrogen, at 77 K, is below argon's freezing point and the argon was freezing from the outside of the cylinder in. In practice there were at least ten to twenty minutes to work.

After tightening, the stage and cell are removed from the nitrogen and allowed to warm to ambient temperature.

4.1.5 Pressure measurement

Pressure in the DAC was measured by ruby fluorescence. Under green or blue light, the ruby fluoresces near 694.5 nm. The fluorescence is composed of two peaks, the stronger called R_1 and the weaker R_2. Both peaks shift with pressure and temperature. Below 30 GPa, the shift is linear with pressure and temperature [1, 5–7]. The pressure calibration for the R_1 peak shift is 2.70 GPa/nm, and the temperature calibration is 148 K/nm [6]. At ambient pressure and temperature the shift for the R_2 peak is not significantly different [5–7].

A small (50 microns - 100 microns) ruby chip is placed in the hole before loading. Naturally the size is kept as small as possible, so that the relative error in the measured volume introduced by the ruby chip is small. A bright source of green light will produce ample fluorescence for measuring pressure; we used a laser or a mercury lamp.

Taking the ratio of the two calibration parameters, one finds that a temperature uncertainty of 1 K implies a measured pressure uncertainty of 20 MPa. To measure pressure precisely, the temperature of the cell should be controlled.

It is possible to measure pressure to 1 MPa using ruby fluorescence if great care is taken with temperature and several ruby spectra are taken [6]. In this work we were satisfied with a precision of 20 MPa, given that the pressures we are interested in go up to 6 GPa. We control the temperature (section 4.1.6) to 0.5 K, which translates to an uncertainty of 10 MPa, if temperature were the sole source of uncertainty in the measurement.

The procedure for measuring pressure in the confocal microscope was as follows. First an unloaded cell with ruby chip was used establish the reference spectrum. Green light from the confocal microscope's mercury lamp was used to excite the fluorescence, and the spectrum was measured using an 0.5 mm diameter optical fiber and an Ocean Optics spectrometer, as shown in the figure. The spectrum was fitted to give the location of the R_1 peak. This yielded the "zero" of the pressure measurement (which is really 100 kPa). Then the cell was loaded, and further pressure measurements were done on the confocal microscope, just as described for the empty cell. Alternatively the loaded cell may be measured first, and the "zero" pressure measured afterward.

In situ pressure monitoring was sometimes used during the cryogenic loading of the cell. A 543 nm diode laser was shined into an 0.5 mm diameter optical fiber attached to the top of the cell. At the bottom of the stage a small optical fiber picked up the fluorescence and carried it to the spectrometer, as shown in figure 4.5. As the cell cooled the ruby peak shifted dramatically, and there was only one peak (R_1) visible at liquid argon temperatures [6]. While tightening the Allen screws the peak location was monitored. In our experience a peak shift just visible, at loading temperature, translates to a pressure at ambient temperature in excess of 1 GPa. Hence, the *in situ* setup was not used for the fluid argon study. Loading to 0.1 GPa was done as described in section 4.1.4.

4.1.6 Temperature control

The cell was heated by a 100 W mica band heater wrapped around the circumference of the cell. The temperature was measured by a platinum resistance temperature detector (RTD) glued to the bottom backing plate as shown in the figure. The temperature was controlled by a proportional integral derivative (PID) controller. All of these components were supplied by Omega.

RTDs are more stable and accurate (± 0.2 K at 273 K) [8] than thermocouples. While they do have a slower response time, a DAC has a large thermal mass which does not respond quickly to small changes in heater output or ambient temperature.

A PID controller adjusts the output of the heater using the PID algorithm [9]:

- Proportional parameter: The controller is set to a desired temperature (*setpoint*). The difference between the temperature of the cell and the setpoint (the *error*), divided by the proportional output parameter, is the fractional output of the heater. For example, if the proportional output parameter is 5 K and the cell is 1 K cooler than the setpoint, the 100 W heater will be run at 20 W. If the proportional parameter is too large then temperature oscillations are produced. When properly adjusted, the proportional parameter will cause the error to approach a constant non-zero value.

- Integral parameter: The temperature is sampled at a given rate. The error at a given time, multiplied by the sampling rate, is summed over some time period. The value of this integral is multiplied by the integral parameter and added to the output of the heater. This corrects for the tendency of the proportional parameter to produce a constant error, but the integral parameter has a tendency to produce overshoots and oscillations in temperature.

- Derivative parameter: The difference in error between sampling times, divided by the sampling rate, is multiplied by the derivative parameter and added to the output of the heater. This corrects for the oscillations produced by the integral parameter, but if the value is too large temperature instability can result.

The PID algorithm is just the damped-driven oscillator in disguise. Early PID controllers were in fact systems of masses, springs, and pnuematic dampeners.

A properly tuned PID algorithm is capable of fine temperature control. There are several algorithms for tuning, but unless the thermal properties of the system are well known, and the system is linear in thermal response, tuning is more art than science. Fortunately the DAC was fairly well-behaved and the temperature was usually kept between 299.7 K and 300.3 K, once the cell had time to reach setpoint.

We chose 300 K for the isotherm we measured because, while it is often described as "room temperature", most people find 300 K a little too warm. Climate-controlled rooms, therefore, will be kept around 300 K. To maintain 300 K only a heater is needed, and a small one at that.

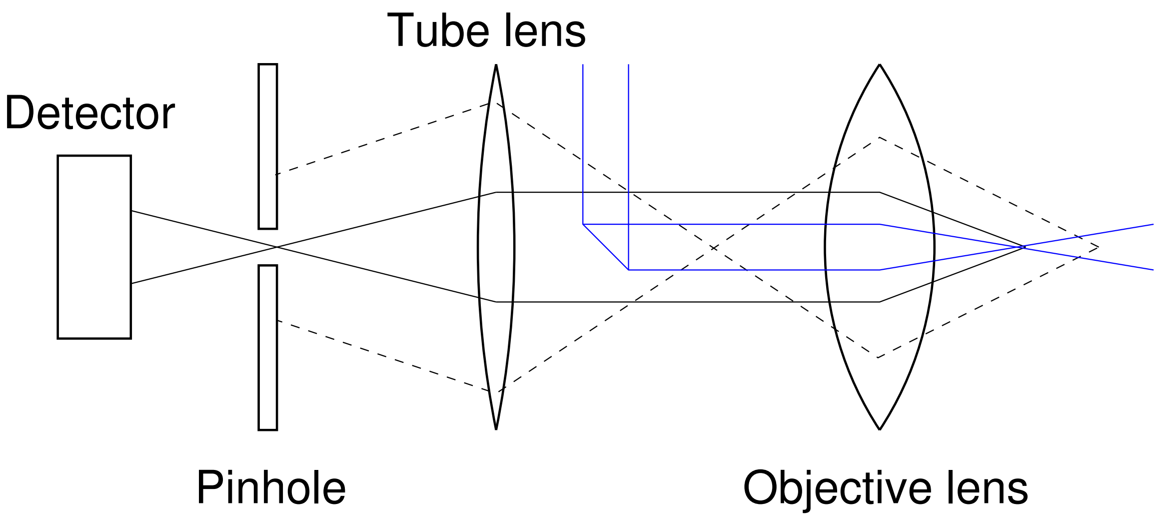

Figure 4.6: Schematic of confocal microscope. Solid lines represent light originating from the focal point, dashed lines represent light originating elsewhere and screened by the pinhole. Blue: the illuminating laser.

4.2 Confocal microscopy

Confocal microscopy was invented in 1957 by Marvin Minsky [10, 11]. As shown in figure 4.6, in essence a confocal microscope consists of two lenses and a pinhole. Light (usually a laser) is shined through the objective lens onto the object. Reflected or emitted (e.g. by fluorescence) light comes back to the objective. Light passing through the focus of the objective passes through the pinhole, but a fraction of the light passing through other points is screened. Images are obtained by scanning over a volume and taking data point by point.

The image is improved in two ways, with respect to conventional microscopy. First, the illuminating laser is focused to a point, and thus the illumination is much more intense than in a conventional microscope. Second, the pinhole improves resolution by screening much of the light that does not pass through the objective focus. An ideal confocal microscope, in the geometric optics limit, would image only the focal point. These improvements come at the price of only being able to look at one small point at a time. Consequently, in order to image an extended object the focal point must be moved. Minsky's microscope moved the stage to image the object, and the image was displayed on a long-persistence oscilloscope [10].

Modern confocal microscopes move the light and lenses by mirrors and motors respectively. The light is captured by a detector and processed by software into an stack of 2D images, one for each focal plane, which may then be processed into a 3D image by software such as ImageJ [12]. Confocal microscopes are capable of high resolution (nanometer scale) 2D images, but typically the resolution in the third dimension is measured in microns [11].

Lateral resolution (x, y) for conventional microscopes is given by the well known formula $0.51\frac{\lambda}{\mathrm{NA}}$ [13], where λ is the wavelength of the light reaching the microscope and NA is the numerical aperture of the lens. A confocal microscope, on the other hand, has a lateral resolution given by $0.37\frac{\lambda'}{\mathrm{NA}}$[13]. λ' is defined by

$$\frac{1}{\lambda'^2} \equiv \frac{1}{\lambda^2} + \frac{1}{\lambda_i^2}, \tag{4.1}$$

where λ_i is the wavelength of the light illuminating the sample and λ the light reaching the microscope. (Since confocal microscopes are often used to image fluorescence, these wavelengths are not necessarily the same.)

Axial resolution (z) for conventional microscopes is given by $\frac{\lambda}{\mathrm{NA}^2}$, while for a confocal microscope it is approximately $1.28\frac{\lambda'}{\mathrm{NA}}$ [13]. Numerical apertures are nearly always less than one, so a confocal microscope has a significantly better resolution [13].

In most biological applications, a confocal microscope uses a laser to illuminate the object, typically a cell with impregnated with dyes. The laser excites fluorescence in the dyes which is collected by the objective. A dichroic mirror filters out the reflected laser light, and a stack of high-resolution 2D images of the fluorescence provides the 3D structure of the cell [11].

In this work, we use the microscope quite differently. Instead of exciting fluorescence to image the interior of the diamond anvil cell, we use the reflected laser light to find the area and optical thickness of the cell, yielding the volume. To our knowledge this technique has not been worked out previously. In order to explain this new technique we must first introduce the measurement of the reflected intensity profile (section 4.2.1), which is best analyzed by modelling the laser as a Gaussian beam (section 4.2.2). The Gaussian beam model is most easily handled by matrix optics (section 4.2.3). This allowed us to calculate the shapes of the peaks in the reflected intensity profile (section 4.2.5), which to our knowledge has not been done previously. From our analysis of this model we were able to develop the method of measuring volume and refractive index discussed in sections 4.2.6, 4.2.7, 4.2.8, and 4.2.9.

4.2.1 Reflected intensity profile

When we first learned to use the microscope we were interested in imaging, for example, crystals of ice VI in water at room temperature and 1 GPa [14]. The confocal microscope produces high quality images of the area of the cell (figure 4.7). However, the axial resolution of fluorescence images is much worse, precluding an accurate determination of the sample thickness.

We had noticed that as we focused down into the diamond anvil cell there were bright flashes as the focal point passed through the surfaces of the diamonds (figure 4.7). It occured to us that the reflected intensity of the light could tell us where the diamond surfaces were located, if we could work out the intensity as a function of the position of the focus. A plot of reflected intensity as a function of focus position, which we call the *reflected intensity profile*, is shown in figure 4.8.

The reflected intensity profile is generated from the image stack as follows. A small

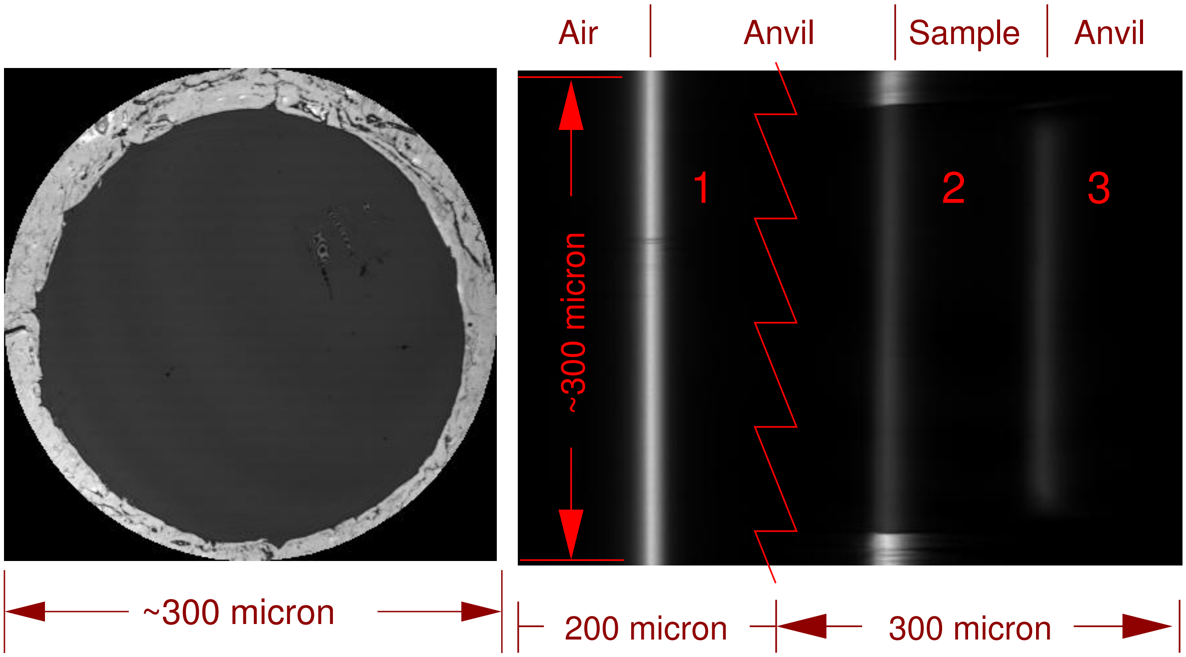

Figure 4.7: Left: Cross-section of diamond anvil cell, showing the sample surrounded by the gasket. Right: Axial section of diamond anvil cell, showing reflections from the interfaces. The jagged line indicates a break of 600 microns. The second diamond-air interface is not shown.

area near the center of the gasket, but not near the ruby chip, is selected using ImageJ. The intensity is averaged over this small area, and this is repeated for every image in the stack (section 4.2.6).

In order to use the reflected intensity profile for measuring the thickness of the sample we needed to model the reflection of the beam from the interfaces. There are four optical interfaces within the cell: the diamond tables, which are air-diamond interfaces, and the diamond culets, which are diamond-sample interfaces. Each interface is reflecting light back through the microscope, as shown in figure 4.9, with most of the light screened by the pinhole.

Modeling the laser as a cone of rays shows that there is a maximum of reflected light when the light is focused on the interface, but the ray optics approximation is not good enough to fit the observed profile (appendix B). A better model for the incident beam

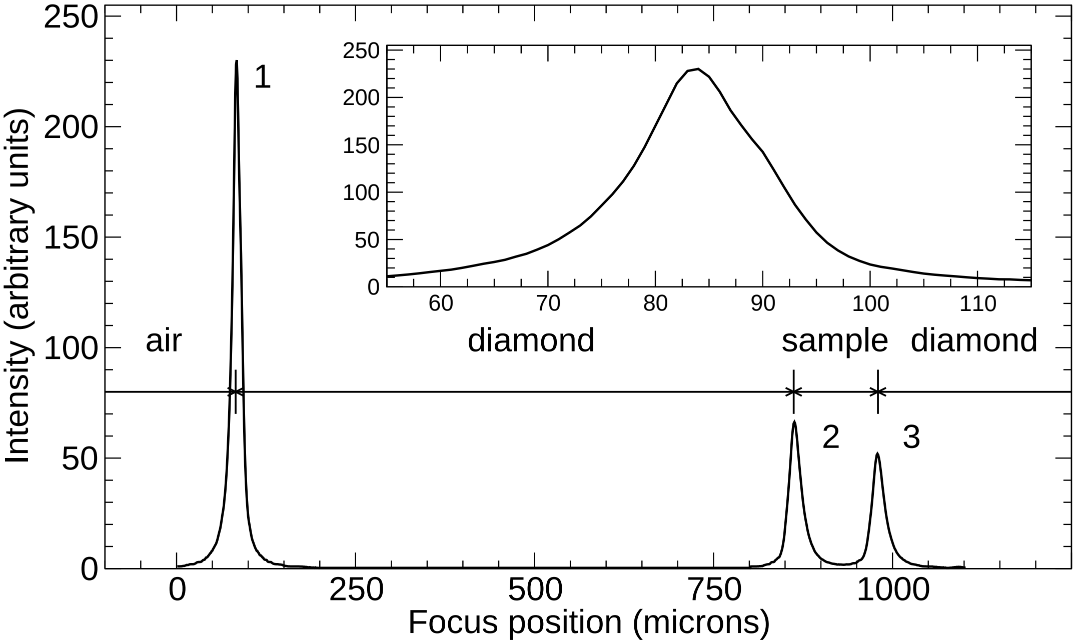

Figure 4.8: Reflected intensity profile. The numbered peaks correspond to the numbered interfaces in figure 4.7. The fourth peak is not shown. Inset: The first peak, plotted to emphasize the shape.

was needed, and so we turned to the Gaussian beam model.

4.2.2 Gaussian beam model

Lasers are modelled as Gaussian beams [15–19]. A Gaussian beam is a solution to the Helmholtz equation in the paraxial approximation ($\sin\theta \approx \theta$, with θ being the angle with respect to the z axis) [15–19]. Starting with the Helmholtz equation:

$$\left(\nabla^2 + k^2\right) E(\vec{r}) = 0, \tag{4.2}$$

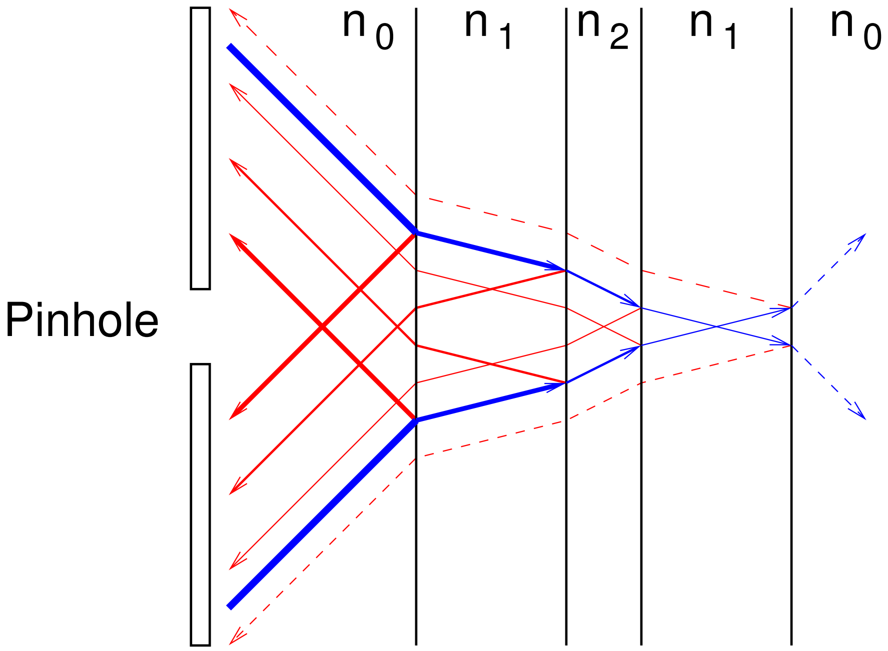

Figure 4.9: Blue lines: cone of light rays incident on a diamond anvil cell. Red lines: light reflecting from the four interfaces and screened by the pinhole. n_0: refractive index of air. n_1: refractive index of diamond. n_2: refractive index of sample.

where k is the wave number and E is the electric field written as a complex-valued scalar, we write the Laplacian in cylindrical coordinates (ρ,ϕ,z):

$$\nabla^2 = \frac{1}{\rho}\frac{\partial}{\partial\rho} + \frac{\partial^2}{\partial\rho^2} + \frac{1}{\rho^2}\frac{\partial^2}{\partial\phi^2} + \frac{\partial^2}{\partial z^2}. \tag{4.3}$$

Spherical wave solutions to the Helmholtz equation in three dimensions are given by:

$$\begin{aligned} E(\vec{r}) &= E_0(\vec{r})e^{\pm i\vec{k}\cdot\vec{r}}, \qquad (4.4) \\ \vec{r} &\equiv x\hat{x} + y\hat{y} + z\hat{z}. \end{aligned}$$

In the paraxial approximation, $\vec{k}$ is nearly parallel to $\hat{z}$, so $\vec{k}\cdot\vec{r} \approx kz$ and we rewrite $E(\vec{r})$ as:

$$E(\vec{r}) = E_0(\vec{r})e^{\pm ikz}. \tag{4.5}$$

Inserting this into the Helmholtz equation gives

$$\left(\frac{1}{\rho}\frac{\partial}{\partial\rho}+\frac{\partial^2}{\partial\rho^2}+\frac{1}{\rho^2}\frac{\partial^2}{\partial\phi^2}\right)E_0 \pm 2ik\frac{\partial E_0}{\partial z}+\frac{\partial^2 E_0}{\partial z^2}=0. \tag{4.6}$$

If $\left|\frac{\partial E_0}{\partial z}\right| << |kE_0|$ and $\left|\frac{\partial^2 E_0}{\partial z^2}\right| << |k^2 E_0|$ then the third term can be neglected, and the paraxial Helmholtz equation is

$$\left(\frac{1}{\rho}\frac{\partial}{\partial\rho}+\frac{\partial^2}{\partial\rho^2}+\frac{1}{\rho^2}\frac{\partial^2}{\partial\phi^2}\right)E_0 \pm 2ik\frac{\partial E_0}{\partial z}=0. \tag{4.7}$$

Equation 4.7 is used to describe optical resonant cavities, such as in lasers. The boundaries of a resonant cavity might be mirrors, symmetric about the z-axis. A Gaussian beam is the fundamental mode of such a cavity, and thus solves equation 4.7. (The solution is rather abstract, so it is relegated to appendix C).

A Gaussian beam is much like a cone of light rays, as shown in figure 4.10. The wave properties of light do not allow it to be focused to the geometric point seen in ray diagrams. Instead, a Gaussian beam has a finite waist w_0 (located at $z = z_0$), the size of which is determined by the wavelength of the light and the half-angle θ of the beam: $w_0 = \frac{2\lambda}{\pi\theta}$.

A Gaussian beam is most intense along the optical axis z and falls off with distance ρ from the optical axis. The intensity of a Gaussian beam is given by:

$$\begin{aligned} I &= I_0\left(\frac{w_0}{w(z)}\right)^2 e^{-\frac{2\rho^2}{w(z)^2}}, && (4.8)\\ w(z) &\equiv w_0\left[1+\left(\frac{\lambda(z-z_0)}{\pi w_0^2}\right)^2\right]^{1/2}. && (4.9)\end{aligned}$$

At the waist, the wave fronts of a Gaussian beam are perpendicular to the z-axis. Far from the waist, the wave fronts are spherical. The radius of curvature of the wavefronts

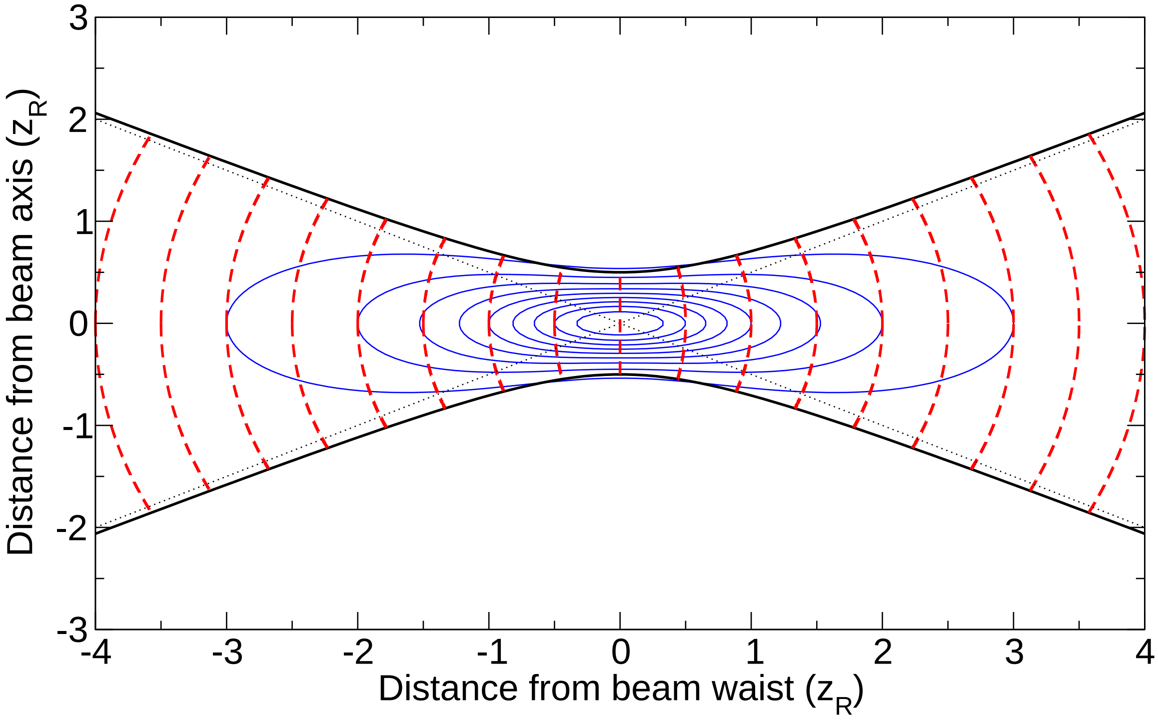

Figure 4.10: Gaussian beam (waist $w_0 = z_R/2$). Blue lines: intensity contour plot, contour interval 10 % of maximum intensity (see equation 4.8). Solid black lines: Beam envelope, defined as $I(z)e^{-2}$ (see equation 4.9). Dotted black lines: cone of light rays which approximates beam. Red lines: wavefronts (see equation 4.10).

is given by

$$R(z) = (z - z_0)\left[1 + \left(\frac{\pi w_0^2}{\lambda(z - z_0)}\right)^2\right]. \tag{4.10}$$

Three parameters characterize a Gaussian beam: wavelength λ, waist position z_0, and waist size w_0. It is convienient to define the Rayleigh parameter $z_R = \frac{\pi w_0^2}{\lambda}$, reducing the number of parameters to two [15, 16].

The laser of a confocal microscope incident on a diamond anvil cell will be reflected from the four diamond surfaces, then propagated through the optics of the microscope, and then screened by a pinhole. In order to understand the reflected intensity profile, it is necessary to figure out what happens to a Gaussian beam subject to these conditions. This had not, to our knowledge, been done before; so we did it ourselves, using the

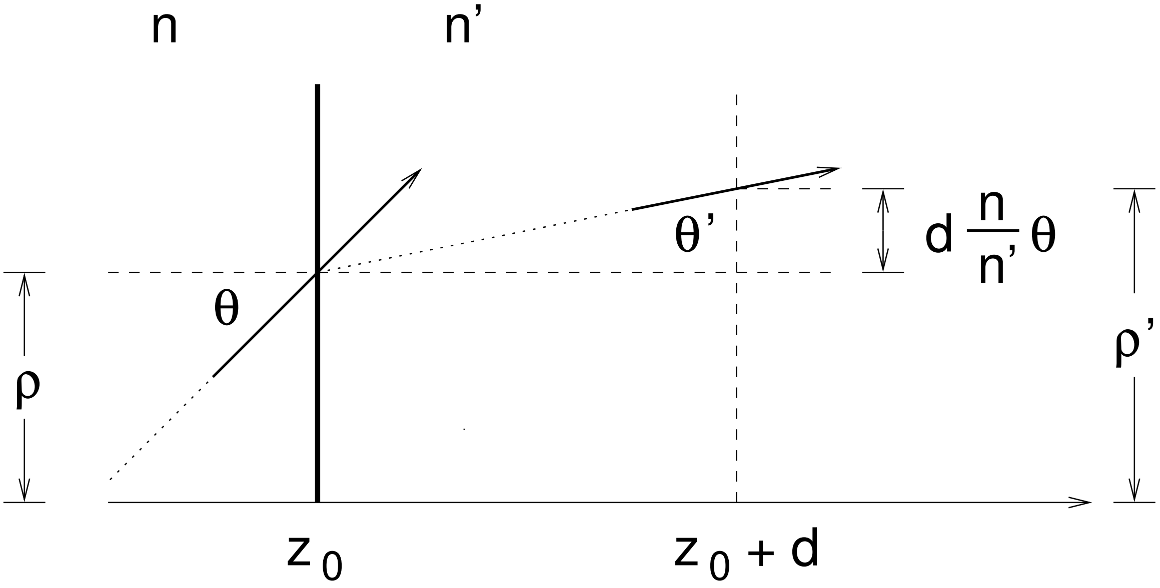

Figure 4.11: A ray at angle θ with respect to the optical axis propagates through a medium of refractive index n. At $z = z_0$ the ray encounters an interface with a medium of refractive index n', and is described by the vector given by expression 4.11. The ray propagates a distance d within the second medium, and its new vector is given according to equation 4.13.

matrix optics formalism desscribed below.

4.2.3 Matrix optics

The behavior of a Gaussian beam in an optical system can be described using matrix optics, a formalism developed for ray optics [15–19].

In matrix optics, a ray is represented by a vector, and there are three matrices which operate on this vector: translation, refraction, and reflection. Combinations of these three types of matrices represent lenses, mirrors, or optical media such as air or diamond. The paraxial approximation $\sin\theta \approx \theta$ is used throughout [15, 16].

A ray, located along the optical axis z at some reference position z_0, is characterized by 3 parameters: the distance ρ from the optical axis, the angle θ with respect to the optical axis, the index of refraction at the reference plane, n. (See figure 4.11.) A ray is represented by the following vector:

$$\begin{pmatrix} \rho \\ n\theta \end{pmatrix}. \tag{4.11}$$

If a ray passes into a medium of index n' at z_0, and propagates to a new position $z_0 + d$, its new angle θ' will be approximately $\frac{n}{n'}\theta$, by Snell's Law. Its new distance ρ' will be $\rho + d\frac{n}{n'}\tan\theta \approx \rho + d\frac{n}{n'}\theta$, as in figure 4.11. Consequently we write the *translation matrix* as

$$\begin{pmatrix} 1 & \frac{d}{n'} \\ 0 & 1 \end{pmatrix}. \tag{4.12}$$

Its operation on a ray is

$$\begin{pmatrix} \rho' \\ n'\theta' \end{pmatrix} = \begin{pmatrix} 1 & \frac{d}{n'} \\ 0 & 1 \end{pmatrix} \begin{pmatrix} \rho \\ n\theta \end{pmatrix} = \begin{pmatrix} \rho + d\frac{n}{n'}\theta \\ n\theta \end{pmatrix}; \tag{4.13}$$

as it must, if the geometry is to work out correctly.

Refraction at plane interfaces is handled automatically by the translation matrix, provided that translation matrices are written to connect each to the next. Refraction at curved interfaces is described as follows.

A ray is incident on a curved surface at $z = z_0$ (see figure 4.12). The surface has a radius of curvature R. (If $R > 0$, then the center of curvature is located at a point $z > z_0$.) Before the surface the index is n, and beyond the surface the index is n'. The ray's distance ρ from the optical axis does not change, but it will be refracted.

The incident angle to the surface γ is $\phi + \theta$, where $\tan\phi \approx \phi = \rho/R$. The refracted angle γ' is, by Snell's Law, $\frac{n}{n'}\gamma$. The new ray angle θ' is therefore $\frac{1}{n'}\left(\frac{n-n'}{R}\rho + n\theta\right)$. In the paraxial approximation the entire curved surface is in the same plane, so the incident

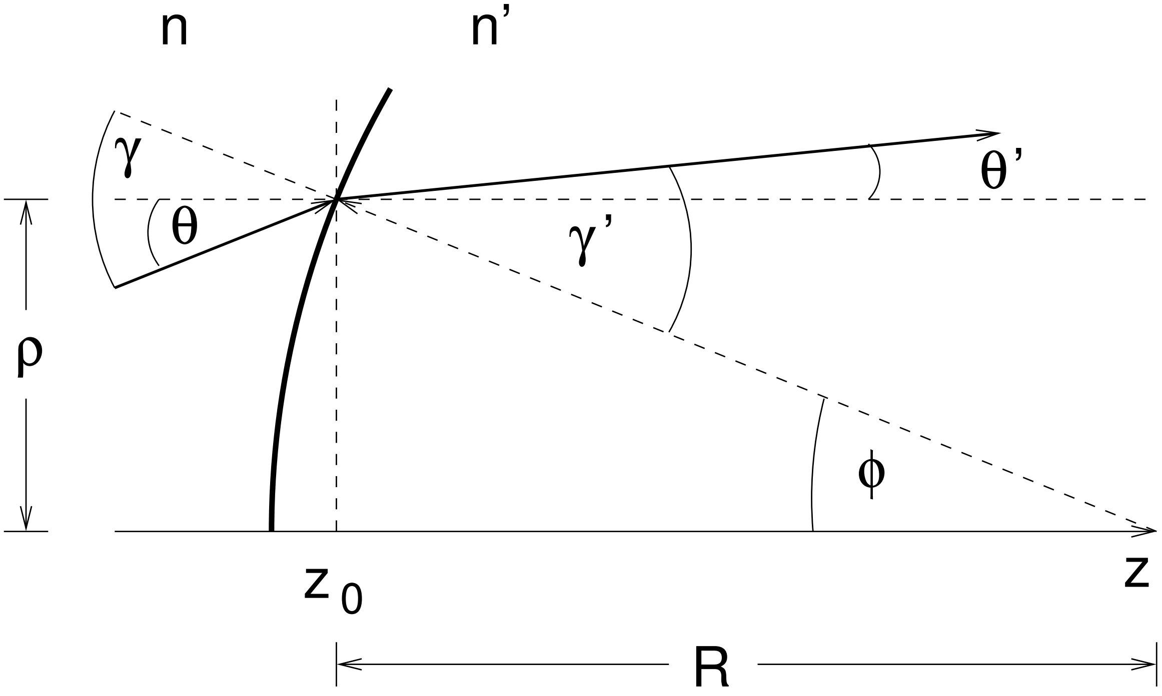

Figure 4.12: A ray at angle θ with respect to the optical axis propagates through a medium of refractive index n. At $z = z_0$ the ray encounters a curved interface with a medium of refractive index n' and radius of curvature R. The ray refracts according to equation 4.14.

ray has the same z coordinate for all ρ. Consequently the *refraction matrix* is given by

$$\begin{pmatrix} 1 & 0 \\ \frac{n-n'}{R} & 1 \end{pmatrix}. \tag{4.14}$$

Note that the refraction matrix reduces to the identity matrix when R is infinite or $n' = n$. It does not reduce to the translation matrix.

The *reflection matrix* from a flat surface is simply the identity matrix. Since $\theta' = -\theta$ this would seem to be wrong. But for reflected beams the direction of propagation is along the negative z direction, and the index n is considered to be negative by convention. Thus $n\theta$ does not change with reflection from a flat surface.

The matrix describing an optical component, such as a lens, is constructed by multiplying these matrices from output to input. For example, consider a thin lens made from a material with index n, with curvature R_1 on the incident side and R_2 on the other side. Let the beam initially propagate in a medium of index 1. In the paraxial approximation, the whole surface of the lens is located in one plane, even though the normal to the surface changes, and for a thin lens we consider the thickness to be zero. The matrix for the thin lens is thus

$$\begin{pmatrix} 1 & 0 \\ \frac{n-1}{-R_2} & 1 \end{pmatrix} \begin{pmatrix} 1 & 0 \\ \frac{1-n}{R_1} & 1 \end{pmatrix} = \begin{pmatrix} 1 & 0 \\ (1-n)\left(\frac{1}{R_2}+\frac{1}{R_1}\right) & 1 \end{pmatrix}. \tag{4.15}$$

If one pays close attention to the sign convention, one may notice that the only term that is not zero or one is found in the lens maker's equation for thin lenses

$$\frac{1}{f} = (n-1)\left(\frac{1}{R_1}+\frac{1}{R_2}\right), \tag{4.16}$$

found in any freshman physics text.

So we can write any thin lens as a matrix in terms of its focal length f:

$$\begin{pmatrix} 1 & 0 \\ -\frac{1}{f} & 1 \end{pmatrix}. \tag{4.17}$$

We can use this matrix to recover the thin lens equation

$$\frac{1}{p}+\frac{1}{q}=\frac{1}{f}, \tag{4.18}$$

also found in any freshman text, where p is the image distance and q is the object distance:

$$\begin{pmatrix} 1 & q \\ 0 & 1 \end{pmatrix} \begin{pmatrix} 1 & 0 \\ -\frac{1}{f} & 1 \end{pmatrix} \begin{pmatrix} 1 & p \\ 0 & 1 \end{pmatrix} = \begin{pmatrix} 1-\frac{q}{f} & p+q-\frac{pq}{f} \\ \frac{1}{q}+\frac{1}{p} & 1-\frac{p}{f} \end{pmatrix}. \tag{4.19}$$

Because p is the object distance and q is the image distance, all rays with the same ρ at p end up at q with the same ρ', regardless of angle. So the angular dependence of ρ' is zero, which means that $p + q - \frac{pq}{f} = 0$, and this is the thin lens equation. All of the other properties of thin lenses, familiar from introductory physics courses, are easily obtained from equation 4.19.

A ray matrix can also be used to propagate spherical waves [15, 16]. Consider the rays normal to a spherical wavefront of radius R. Because $\sin\theta = \rho/R$ and $\sin\theta \approx \theta$ in the paraxial approximation, $R = \rho/\theta$. Consequently

$$R' = \frac{A\rho + Bn\theta}{C\rho + Dn\theta} = \frac{A\frac{R}{n} + B}{C\frac{R}{n} + D}. \tag{4.20}$$

This is known as the *ABCD rule*.

A Gaussian beam, in this formalism, is accomodated by a complex radius [15, 16]:

$$\begin{aligned} q &\equiv z + iz_R, && (4.21) \\ \frac{1}{q} &= \frac{n}{R(z)} + i\frac{n\lambda}{\pi w(z)^2}, && (4.22) \end{aligned}$$

and the operation of the ray matrix is given by

$$q' = \frac{Aq + B}{Cq + D}, \tag{4.23}$$

just as for R.

It is not easy to see how to work this out from first principles, but it is easy to show that it works (appendix C). At the beam waist, $1/R = 0$, and $w = w_0$, thus $q = -i\frac{\pi w_0^2}{n\lambda}$. At some distance z from the waist, $R(z) = z\left[1 + \left(\frac{\pi w_0^2}{\lambda z}\right)^2\right]$ and $w(z) = \sqrt{1 + \left(\frac{\pi w_0^2}{\lambda z}\right)^2}$. The matrix is given by $A = 1, B = z/n, C = 0, D = 1$. Applying the ABCD rule to $1/q$ gives $1/q'$. Matching the real and imaginary parts of q to q' recovers $R(z)$ and $w(z)$.

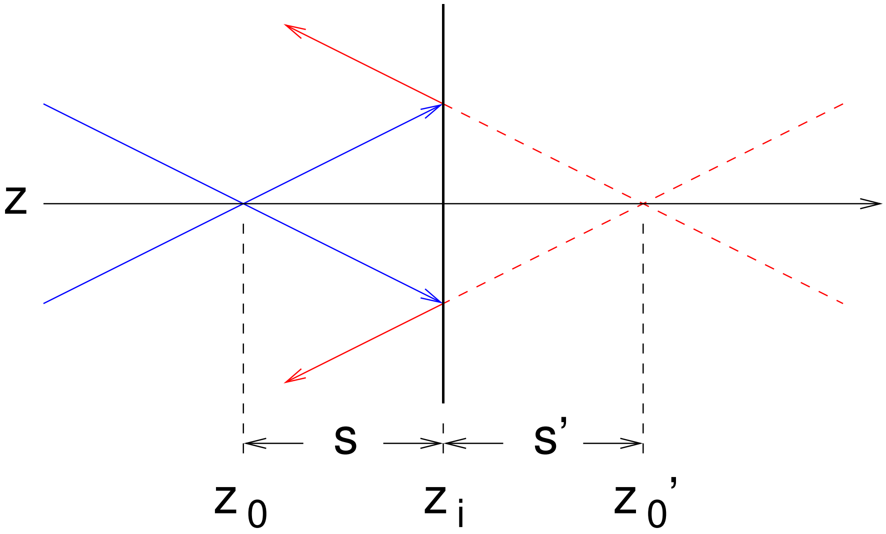

Figure 4.13: Reflection of a Gaussian beam (approximated in the drawing by a cone). s and s' are the image and object distance respectively. By convention, s and s' have the same sign when z_0 and z_0' are on opposite sides of the lens. Blue: incident beam. Red: reflected beam.

4.2.4 Thin lens equations and reflection

Armed with the matrix optics formalism, we can determine what effect optical components such as reflecting interfaces and lenses will have on Gaussian beams [15, 16, 20].

First we work out the effect of reflection. A Gaussian beam is characterized by its Rayleigh parameter z_R and the position of its waist z_0. It propagates to an interface located at z_i and the reflected beam will have a new waist position z_0' and a new Rayleigh parameter z_R', as shown in figure 4.13. It is convenient to write in terms of the object distance $s \equiv z_i - z_0$ and $s' \equiv z_0' - z_i$.

The reflection matrix is given by

$$\begin{pmatrix} 1 & \frac{s'}{-n} \\ 0 & 1 \end{pmatrix} \begin{pmatrix} 1 & 0 \\ 0 & 1 \end{pmatrix} \begin{pmatrix} 1 & \frac{s}{n} \\ 0 & 1 \end{pmatrix} = \begin{pmatrix} 1 & \frac{s-s'}{n} \\ 0 & 1 \end{pmatrix}. \qquad (4.24)$$

Because we are dealing with beam waists, $1/q = -\frac{i}{z_R}$ and $1/q' = -\frac{i}{z_R'}$. Applying the ABCD rule yields

$$\begin{aligned} s - s' &= 0, & (4.25) \\ -\frac{i}{z_R} &= -\frac{i}{z'_R}. & (4.26) \end{aligned}$$

The new Rayleigh parameter is equal to the old one. The image distance is equal to the object distance, which is the same result that geometric optics gives for reflection from a plane mirror.

Refraction through a thin lens of focal length f, located at z_i, is handled similarly (with $n = 1$):

$$\begin{pmatrix} 1 & s' \\ 0 & 1 \end{pmatrix} \begin{pmatrix} 1 & 0 \\ -1/f & 1 \end{pmatrix} \begin{pmatrix} 1 & s \\ 0 & 1 \end{pmatrix} = \begin{pmatrix} 1 - \frac{s'}{f} & s + s' - \frac{ss'}{f} \\ -\frac{1}{f} & 1 - \frac{s}{f} \end{pmatrix}. \tag{4.27}$$

We apply the ABCD rule and get

$$s' - f = f^2 \frac{s - f}{(s - f)^2 + z_R^2}, \tag{4.28}$$

the first thin lens law for Gaussian beams derived by Self [20].

In the geometric limit $z_R \to 0$ and equation 4.28 reduces to the familiar $1/f = 1/s + 1/s'$. However, a surprising result is obtained for Gaussian beams which has no analog in geometric optics. A beam waist at the focus is propagated to the other focus, not to infinity, even in the limit $z_R \to 0$. We also get

$$z'_R = \frac{f^2}{(s - f)^2 + z_R^2} z_R, \tag{4.29}$$

the second thin lens law derived by Self [20].

These two relations will be used to find the reflected intensity as a function of the

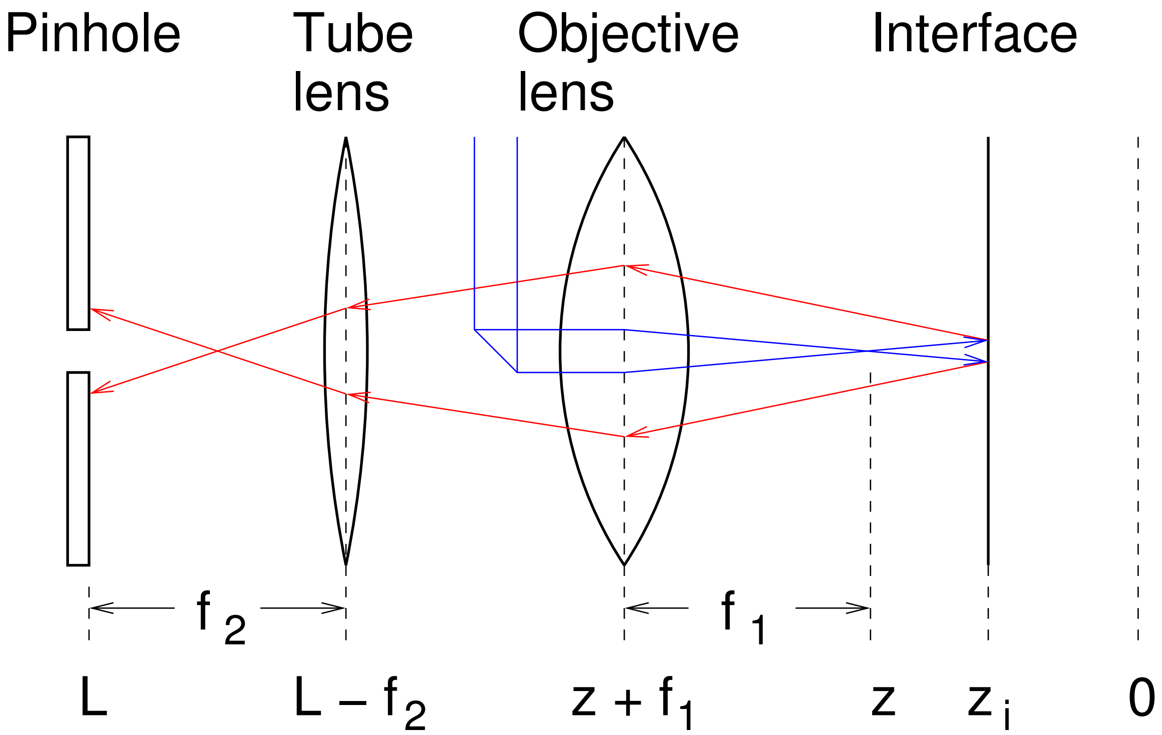

Figure 4.14: Coordinate system for calculating reflected intensity profile. Blue: incident laser. Red: Light reflected from interface. See page 80 for description of coordinates.

focus position.

4.2.5 Reflected intensity as a function of focus position

Here we present the shape of the reflected intensity profile, derived from the properties of Gaussian beams via matrix optics and the Gaussian thin lens equations. To our knowledge this has not been derived before.

The optical components of a confocal microscope which we consider here are two lenses and a pinhole. We apply the thin lens laws (equations 4.28, 4.29) to propagate the Gaussian beam incident on the objective to the pinhole. Then we calculate the intensity of the resulting Gaussian beam screened by the pinhole, using equation 4.8.

As shown in figure 4.14, a laser beam with Rayleigh parameter R is focused with its waist at position z. The beam is incident on an interface at z_i. The beam is reflected, yielding a new waist position z_0, but the Rayleigh parameter is unchanged. The beam is then refracted by the objective lens of focal length f_1, located at $z + f_1$, yielding a new waist at z_1 and a new Rayleigh parameter R_1. The beam then is refracted by the tube lens of focal length f_2, located at $L - f_2$. (L is the distance of the pinhole from the zero of the coordinate system, of the order of ten cm.) The resulting beam has a waist position at z_2 and a Rayeigh range of R_2. It is then screened by a pinhole of diameter D located at L.

Integrating the intensity of the beam over the diameter of the pinhole gives the power reaching the detector:

$$P(z_2) = P_i \left[1 - \exp\left(-\frac{D^2}{2w_2^2} \frac{R_2^2}{R_2^2 + (L - z_2)^2} \right) \right], \tag{4.30}$$

where P_i is proportional to the reflection coefficient of the interface, described in more detail below, and w_2 is the waist size determined by the Rayleigh parameter R_2.

Using the thin lens laws twice on the initial waist position and Rayleigh parameter gives z_2 and R_2:

$$z_2 = L + q^2 f_2^2 \frac{pq^2 - \left(\frac{1}{2}q^2 + f_1^2\right)(q^2 - R^2)^{1/2}}{\left[pq^2 - \left(\frac{1}{2}q^2 + f_1^2\right)(q^2 - R^2)^{1/2}\right]^2 + f_1^4 R^2}, \tag{4.31}$$

$$R_2 = f_1^2 f_2^2 \frac{q^2}{\left[pq^2 - \left(\frac{1}{2}q^2 + f_1^2\right)(q^2 - R^2)^{1/2}\right]^2 + f_1^4 R^2} R, \tag{4.32}$$

with $p \equiv (L - 2f_1 - 2f_2 - z_i)$ and $q^2 \equiv 4(z - z_i)^2 + R^2$.

If the focus is close to the interface, $q << p$ and the expressions reduce to

$$z_2 \approx L - 2\left(\frac{f_2}{f_1}\right)^2 (z - z_i), \tag{4.33}$$

$$R_2 \approx \left(\frac{f_2}{f_1}\right)^2 R, \tag{4.34}$$

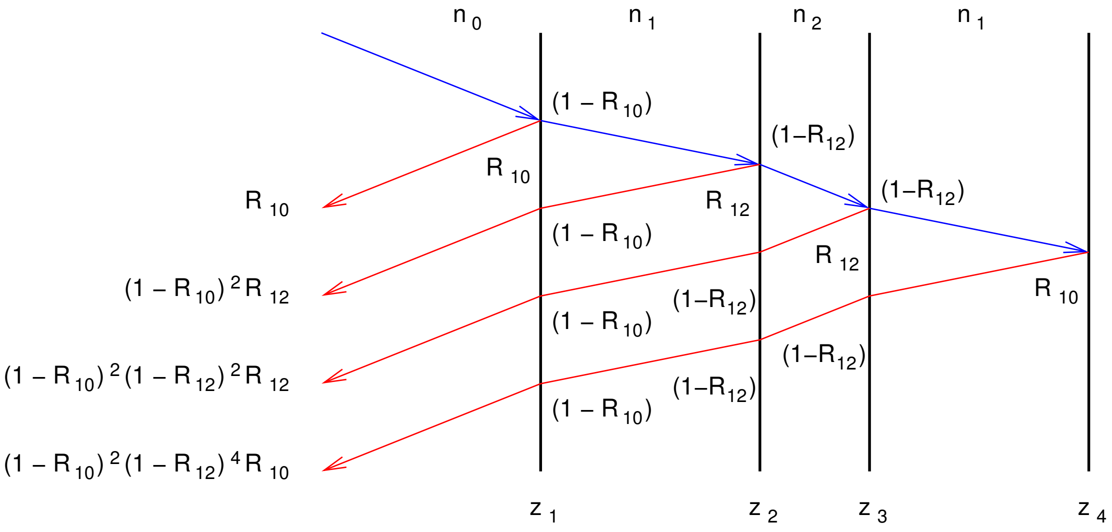

Figure 4.15: Summing of reflections from multiple interfaces. Blue lines: incident light. Red lines: reflected light.

and $w_2^2 = \frac{w^2}{R}R_2 = \left(\frac{f_2}{f_1}\right)^2 w^2$.

Substituting into the expression for the power gives the profile for reflection from one interface:

$$f_i(z) = Q_i \left[1 - \exp\left(-\frac{D^2}{2w^2}\left(\frac{f_1}{f_2}\right)^2 \frac{R^2}{4(z-z_i)^2 + R^2}\right)\right], \tag{4.35}$$

with Q_i proportional to the reflection coefficient of the interface.

The reflection profile from multiple interfaces is simply the sum of single interface profiles, but the Q_i terms will contain reflection and transmission coefficients for every interface the beam has passed through on its way to the pinhole. In this work there are four interfaces, and as shown in figure 4.15,

$$Q_1 = R_{10}, \tag{4.36}$$

$$Q_2 = (1 - R_{10})^2 R_{12}, \tag{4.37}$$

$$Q_3 = (1 - R_{10})^2 (1 - R_{12})^2 R_{12}, \tag{4.38}$$

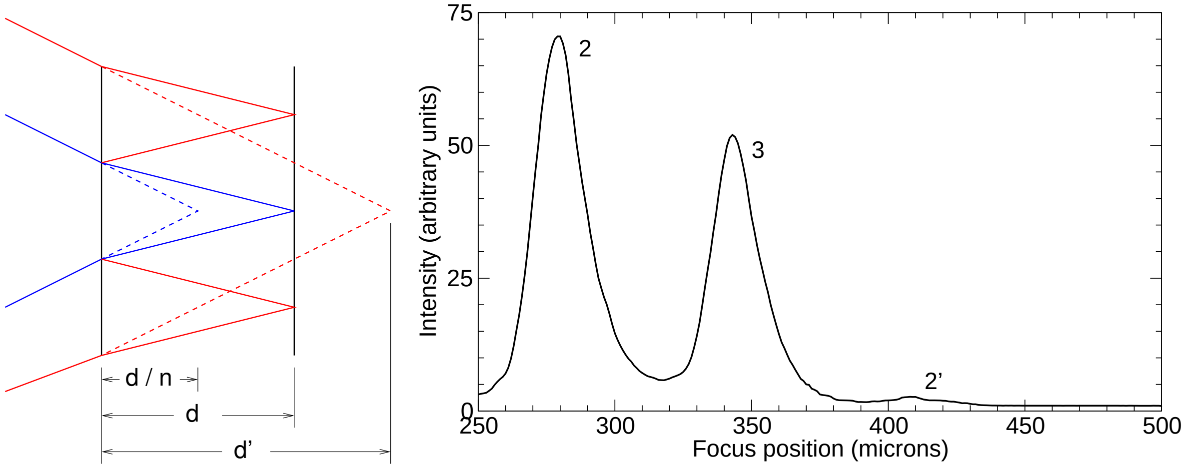

Figure 4.16: Left: Optical thickness and the effect of secondary reflections. Primary reflections (blue), due to refraction, appear to originate from d/n (optical thickness) rather than from d (true thickness). Secondary reflections (red) appear to orginate from d', and are displaced from primary reflections in the reflected intensity profile. Right: Reflected intensity profile showing secondary reflection peak 2' of peak 2.

$$Q_4 \quad = \quad (1 - R_{10})^2 (1 - R_{12})^4 R_{10}, \tag{4.39}$$

with R_{jk} the reflection coefficient for the interface between index j and index k. The differences between peak locations z_i and z_{i+1} will give the optical thickness d/n of the medium between the interfaces, as figure 4.16 illustrates.

Of course a beam does not reflect only one time from each interface. Between interface 1 and 2, for example, there are an infinite number of secondary reflections, but each one appears in a different location, as the figure illustrates. An example of a multiple reflection from our data appears in the figure.

We want this model to have general applicability and so we do not want to have to know exactly what the optical parameters of the microscope are. Consequently we do not explicitly identify the parameters in the profile, and we rewrite the function as

$$f_i(z) = A_i \left(1 - e^{-a_i}\right)^{-1} \left[1 - \exp\left(-a_i \frac{R_i^2}{4(z - z_i)^2 + R_i^2}\right)\right]. \tag{4.40}$$

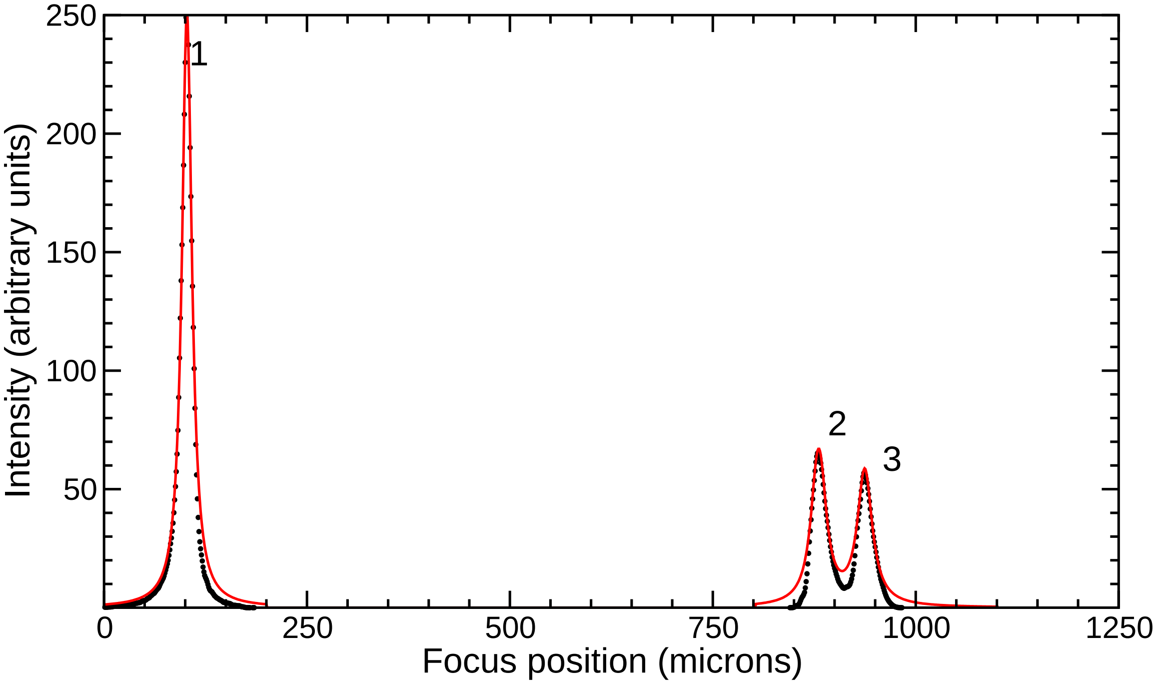

Figure 4.17: Fit (red) of the reflected intensity profile (black) to the expression 4.40 via the Taylor expansion 4.41.

Because least-squares fitting to this function is numerically problematic, we fit our profile data to its Taylor expansion about z_i:

$$f_i(z) \approx A_i \left[1 - \frac{8a_i}{R_i^2(e_i^a - 1)}(z - z_i)^2 + \frac{(384a_i - 192a_i^2)}{R_i^4(e_i^a - 1)}(z - z_i)^4 \right]. \qquad (4.41)$$

The result may be seen in figure 4.17.

4.2.6 Measuring volume: experimental procedure

Here we present the confocal volume measurement technique we developed. To our knowledge this has not been done before.

The confocal microscope which we used is a Zeiss LSM 510 Meta, shown in figure 4.18. We used the 514 nm argon laser to illuminate the cell. The light passed though an 80/20 beamsplitter, through the objective lens, which is a 10X apochromatic lens

Figure 4.18: Zeiss LSM 510 Meta, at the Franchesci Microscopy and Imaging Center, Washington State University.

with numerical aperture of 0.26 (yielding a Rayleigh range of 2.4 microns and a waist size of 0.6 microns). It reflected from the cell, back through the objective and the tube lens, and was screened by a pinhole of diameter 174 microns.

The preparations for a volume measurement were as follows: First, we found the boundary of the sample using the eyepiece of the microscope, and restricted the scanning area to a circle centered on the sample, as shown in figure 4.19. Next, we moved the stage back 800 microns to find the first air diamond interface, and adjusted the gain of the detector so that the signal was not saturated. Next, we moved the stage forward 400 microns and adjusted the offset of the detector so the signal was zero. (If a is about 1 and R is about 12 microns, as in our data, the reflected intensity fraction of the peak value 400 microns from the peak should be about 0.0004, close to zero.) Then, we

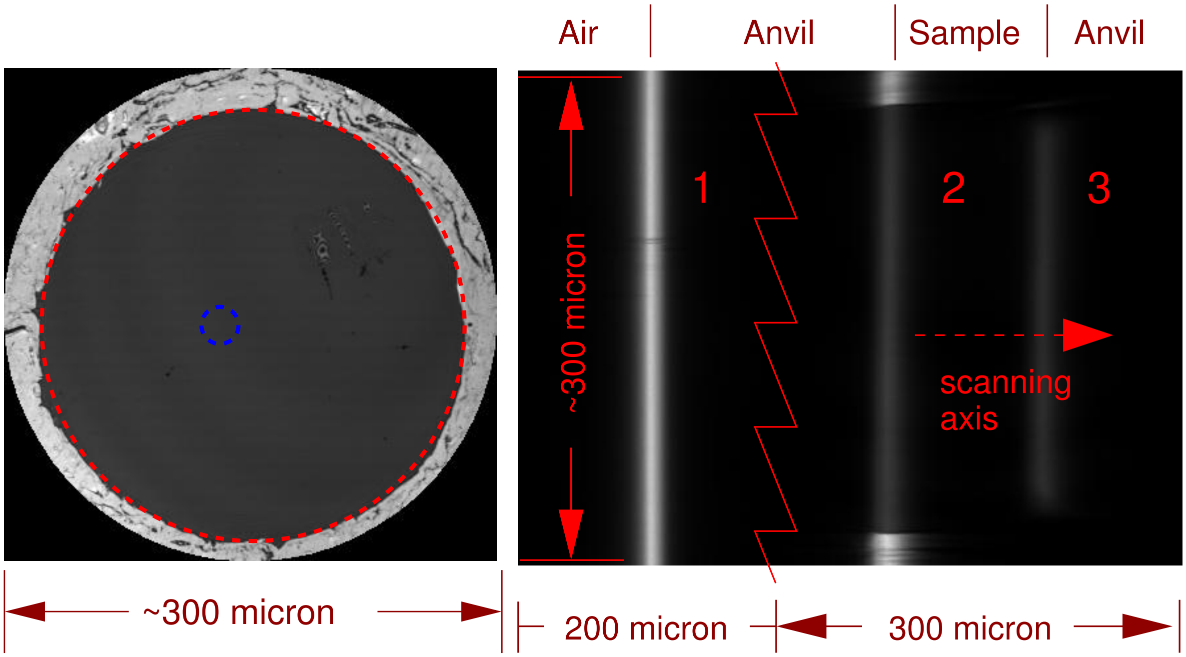

Figure 4.19: Left: Cross-section of diamond anvil cell, showing the sample surrounded by the gasket. Black areas are not scanned. Blue circle: Area in which greyscale is averaged to produce reflected intensity profile. Red circle: Fitted ellipse to determine area of sample. Right: Axial section of diamond anvil cell, showing reflections from the interfaces. The jagged line indicates a break of 600 microns. The second diamond-air interface is not shown. Interfaces must be perpendicular to scan axis.

moved the stage to 100 microns before the peak and scanned at 5 micron intervals for 1100 microns. Finally, we looked at the side projection of the image stack. The three peaks should look like thick planes viewed edge-on. They should be perpendicular to the scanning axis. If they were not, then the cell was readjusted in the stage and the preparations repeated.

Once the microscope was prepared we scanned the cell in two sections. First, we scanned a thickness of 200 microns centered around the air-diamond interface. Then we moved the stage forward 600 microns and scanned a thickness of 300 microns, starting before the first diamond-sample interface and finishing beyond the second. We did not scan the fourth air diamond interface. We scanned at 1 micron intervals. The result was a stack of 501 images, omitting the uninteresting interior of the diamond.

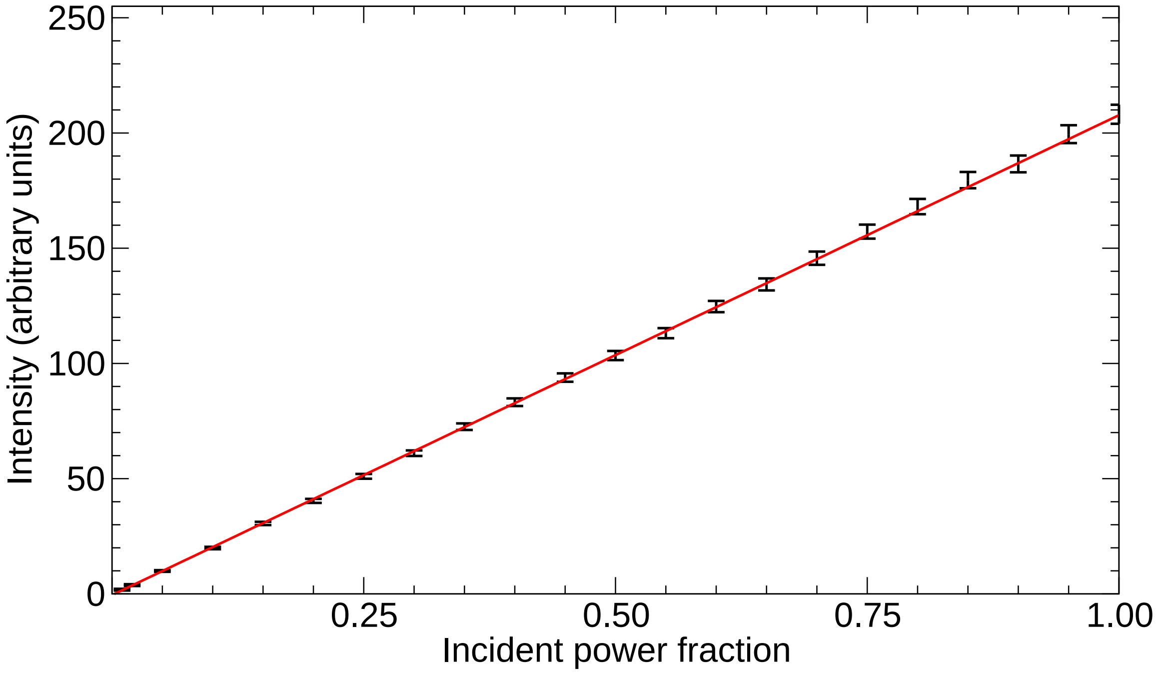

Figure 4.20: Reflected intensity as a function of incident laser power. The greyscale value ranges from 0 to 255. If greyscale is not directly proportional to the intensity of the light, our refractive index measurements will be wrong.

4.2.7 Optical thickness and area

Once the image stack was collected, we used ImageJ [12] to get the reflected intensity profile. We chose a small area near the center of the cell, not near the ruby, as shown in figure 4.19. We then calculated the average greyscale value of the circle for all 501 images. The greyscale value is directly proportional to intensity, as shown in figure 4.20.

The result was output to a text file. When plotted, the reflected intensity profile appeared as three peaks. The three peaks were fitted to the Taylor expansion of the model profile, as described above and shown in figure 4.17. The optical thickness of the sample was given by the difference in peak positions corresponding to the diamond culets (numbered 2 and 3 in figure 4.17).

The area of the sample was determined by selecting the image at the surface of the gasket. In this image, we fit an ellipse to the area of the hole, as shown in figure 4.19, and ImageJ counted the pixels in the ellipse. Each pixel represents an area, which is calculated by the microscope based on the lens and laser wavelength used. In this work the area of one pixel was 0.77 μm^2.

4.2.8 Refractive index and calibration

The ratios of the peak heights A_i yield the refractive index of the sample. The ratio P_{21} of peak 2 to peak 1 is, according to our model

$$P_{21} = \frac{(1 - R_{10})^2}{R_{10}} R_{12} \tag{4.42}$$

and the ratio P_{31} of peak 3 to peak 1 is

$$P_{31} = \frac{(1 - R_{10})^2 (1 - R_{12})^2}{R_{10}} R_{12}. \tag{4.43}$$

The well-known indices of diamond [3] (n_1) and air [21] (n_0) at 514 nm are used to calculate R_{10}. Inverting these expressions gives two estimates for R_{12}, and we get the sample index n_2

$$n_2 = \left(\frac{1 - \sqrt{R_{12}}}{1 + \sqrt{R_{12}}} \right) n_1. \tag{4.44}$$

Other than refraction and specular reflection, no other optical effects, such as absorption and scattering, are accounted for in this model. Consequently, the values for the index which we calculated from the peak ratios needed correction. We did this by measuring substances for which the refractive index is well known. Organic solvents are found in most labs and have indices ranging from 1.3 to 1.6, which is where most of our measurements were done. If the anvils, gaskets, laser wavelengths, or objective lenses are very different from those used in the calibrated set of measurements, it is best to

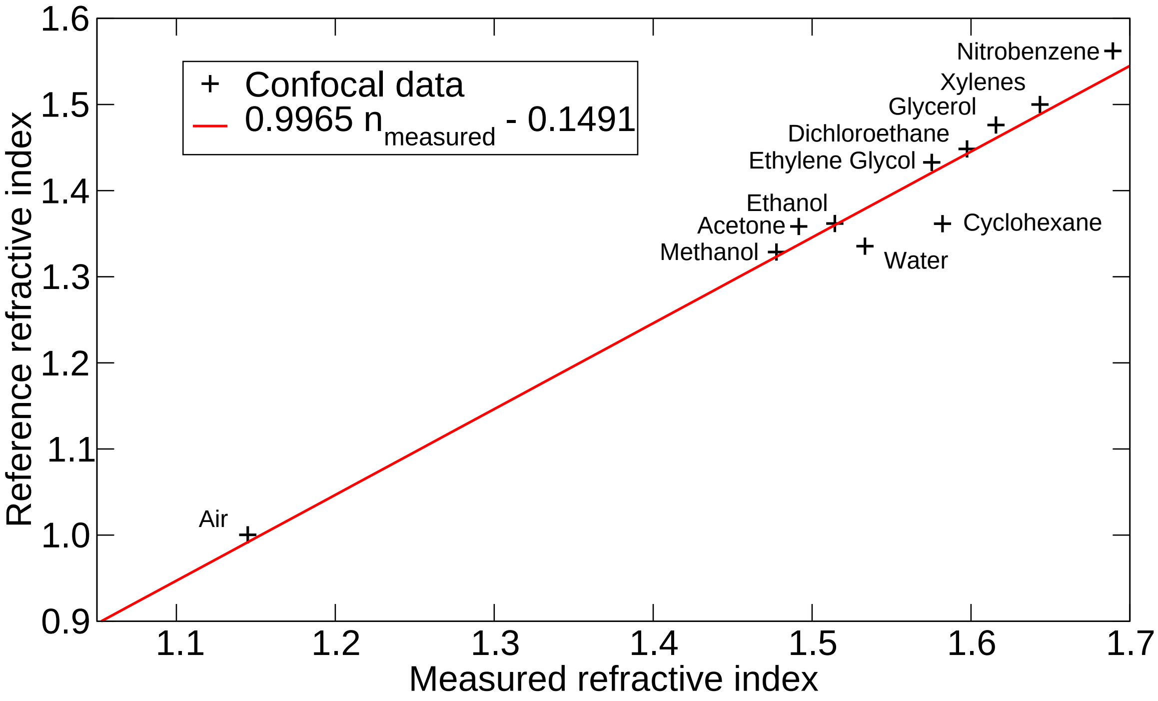

Figure 4.21: Refractive index measurement calibration using various organic solvents. The measurements for water and cyclohexane deviate considerably from the fit line. In other experiments we measured the index of water more accurately [22].

recalibrate.

Figure 4.21 shows a plot of known index as a function of measured index. Our argon measurements are calibrated to the linear fit of these data.

4.2.9 Precision of measurements

The precision of the optical thickness measurement is dependent on the precision of the motors that move the stage of the microscope. Repeated measurements of the optical thickness of a diamond anvil gave an estimate of 1 micron for the precision of the optical thickness measurement. Consequently gaskets should be thick for confocal measurements; in this work ours were between 100 microns and 200 microns.

The precision of the refractive index measurement is calculated from the scatter of measured indices about the calibration line shown in figure 4.21, and is estimated to be

1 %.

The precision of the area measurement is dependent on the shape of the gasket. An uncertainty of 1 % was estimated by repeatedly fitting ellipses to the same hole, and by comparing with the size of the bit used to drill the hole.

If these three measurements are multiplied to produce a measurement of absolute sample volume, the uncertainty in the volume measurements will be approximately 2 %. One way to reduce the uncertainty is to fit the refractive index to a function of pressure, and use the fitted index rather than the measured index to calculate the volume. Relative volumes were produced by fitting the measured volumes of the solidifed sample to an equation of state from the literature; for many solids precise X-ray data exist. Using this procedure the error on the relative volumes, as a function of pressure, were estimated to be 1 %, as judged by the standard deviation of the scatter of the relative volumes about the known equation of state [23].

4.3 Fourier transform infrared spectroscopy

In this work we also wished to investigate the behavior of the asymmetric stretching mode of carbon dioxide dissolved in argon. The frequency of the stretching mode changes with pressure; this change in pressure should depend fundamentally on changes in the local density of argon near the carbon dioxide molecule and thus probe the structure (section 5.2.1). We are the first, to our knowledge, to measure the frequency as a function of pressure and density for argon and nitrogen at ambient temperature.

4.3.1 The interferogram

FTIR spectrometry uses an interferometer in place of a diffraction grating. The type used in this work is a Michelson interferometer, invented in 1880 [24]. Infrared light

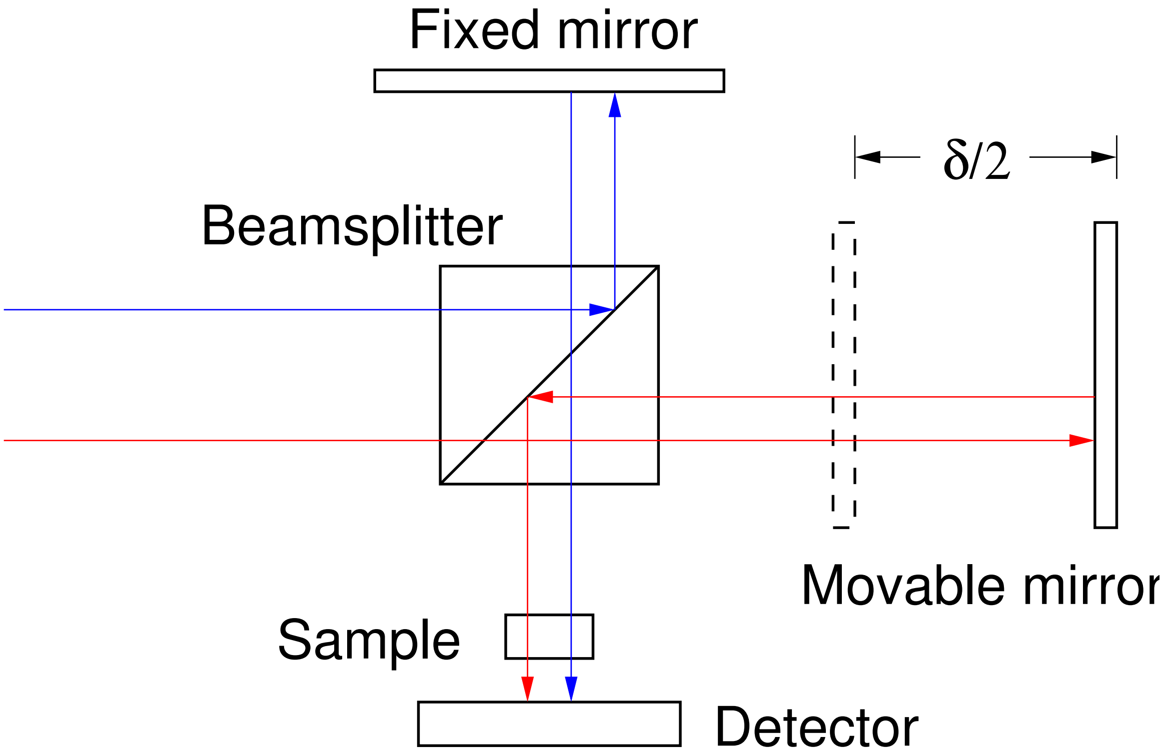

Figure 4.22: Schematic of interferometer. Blue lines: beam that reflects from the fixed mirror. Red lines: beam that reflects from the movable mirror. At the detector the beams interfere.

passes through a beamsplitter. One beam is reflected from a fixed mirror, and then to the detector. The other beam is reflected from a movable mirror, and then to the detector, as shown in figure 4.22.

A source of infrared light emits photons at many frequencies; we denote the number emitted as a function of frequency $N(\omega)$. The number of photons of frequency ω which reach the detector will vary with the path difference δ between between the two beams. When δ is half a wavelength, $N(\omega)$ will be zero, and when δ is a full wavelength $N(\omega)$ will be a maximum. Consequently it will be simpler to write $N(\omega)$ in terms of the wave number, $k = \omega/c$, where c is the speed of light. The interferometer does not "know" the frequency of the photons, it only "knows" the position of the mirror. We write the number of photons detected as a function of mirror position, $N_d(\delta)$, as

$$N_d(\delta) = N(k)(1 + \cos k\delta). \tag{4.45}$$

The detector will therefore produce a signal with "AC" and "DC" components; if we drop the DC component we get

$$N_d(\delta) = N(k)\cos k\delta. \tag{4.46}$$

This relationship is a Fourier cosine transform. If more than one frequency is emitted from the source, the *interferogram* $N(\delta)$ is given by

$$N_d(\delta) = 2\int_0^\infty N(k)\cos k\delta\, dk, \tag{4.47}$$

as illustrated for a very simple case in figure 4.23.

A real detector does not detect photons of all frequencies equally well, and neither does a real beamsplitter reflect and transmit photons of all frequencies equally. We can modify $N_d(\delta)$ with expressions for the efficiency of the detector, $E_D(k)$ and the efficiency of the beam splitter, $E_B(k)$:

$$N_d(\delta) = 2\int_0^\infty N(k)E_D(k)E_B(k)\cos k\delta\, dk = 2\int_0^\infty N(k)I(k)\cos k\delta\, dk, \tag{4.48}$$

where $I(k)$ is an function summarizing the response of the all the instruments.

Of course what we are actually interested in is the response of the sample to infrared light, $S(k)$, and so the number of photons detected, if a sample is present, is

$$N_d(\delta) = 2\int_0^\infty N(k)I(k)S(k)\cos k\delta\, dk \tag{4.49}$$

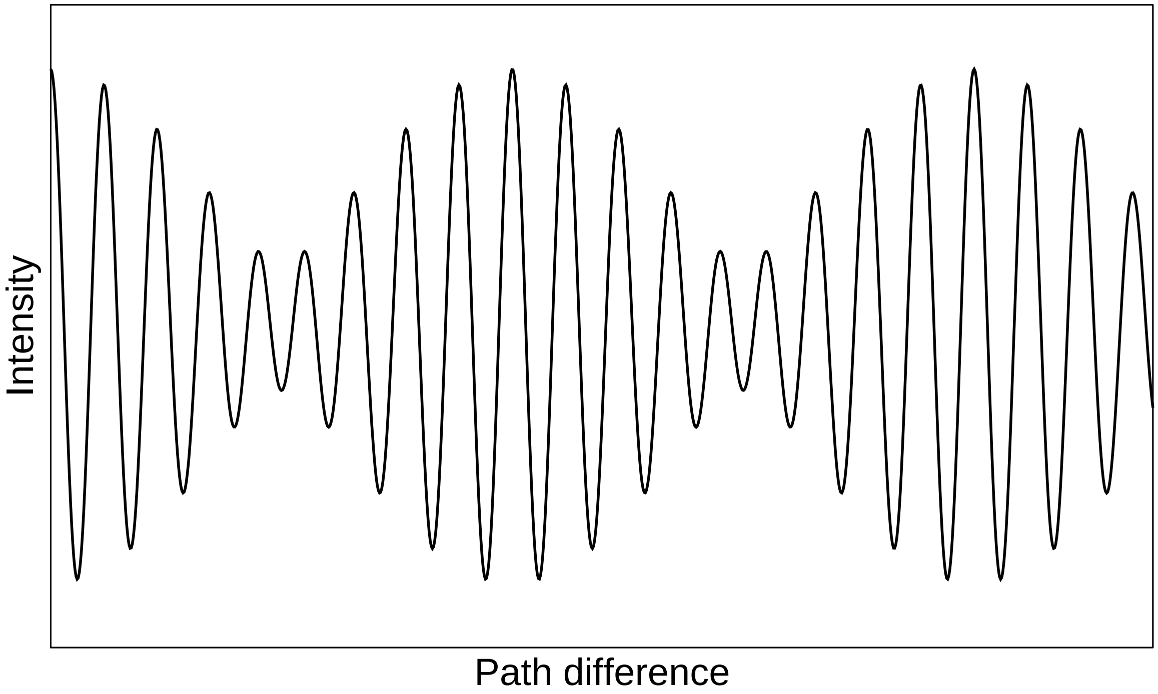

Figure 4.23: A very simple interferogram. The source emits N_1 photons at wave number k_1 and N_2 photons at wave number k_2.

In order to get $S(k)$ out of $N_d(\delta)$, we take the inverse Fourier cosine transform of both sides:

$$2\int_0^\infty N_d(\delta)\cos k\delta\, d\delta = N(k)I(k)S(k). \tag{4.50}$$

Collecting an interferogram without a sample present will yield $N(k)I(k)$; the ratio of the spectra will yield $S(k)$.

While we have presented here the essential principle of FTIR spectrometry, there is a great deal more to consider. For example, the movable mirror cannot go out to infinity, so the Fourier transform is truncated at the maximum displacement L. This limits the resolution Δk of the spectrometer to $\Delta k \propto 1/L$; as well as changing the shapes of spectral lines, which must be corrected by a mathematical function known as the *apodization*. In addition, the interferogram is only sampled at finite intervals, so the Fourier transform is actually a discrete Fourier transform. This produces the effect

Figure 4.24: Bomem DA8 FTIR spectrometer.

known as *aliasing*, where a waveform is reflected and sent to a part of the spectrum where it doesn't really occur [24, 25]. These and other practical considerations are important for understanding a real spectrometer, but a thorough discussion will not be undertaken here.

4.3.2 Using the FTIR spectrometer

In this work we used a Bomem DA8 FTIR spectrometer, shown in figure 4.24. The source of infrared light is a globar, which emits a blackbody spectrum. The beamsplitter is composed of KBr, appropriate for a range between $450\,\mathrm{cm}^{-1}$ and $5000\,\mathrm{cm}^{-1}$. The detector is InSb, which must be cooled to liquid nitrogen temperatures and is suitable

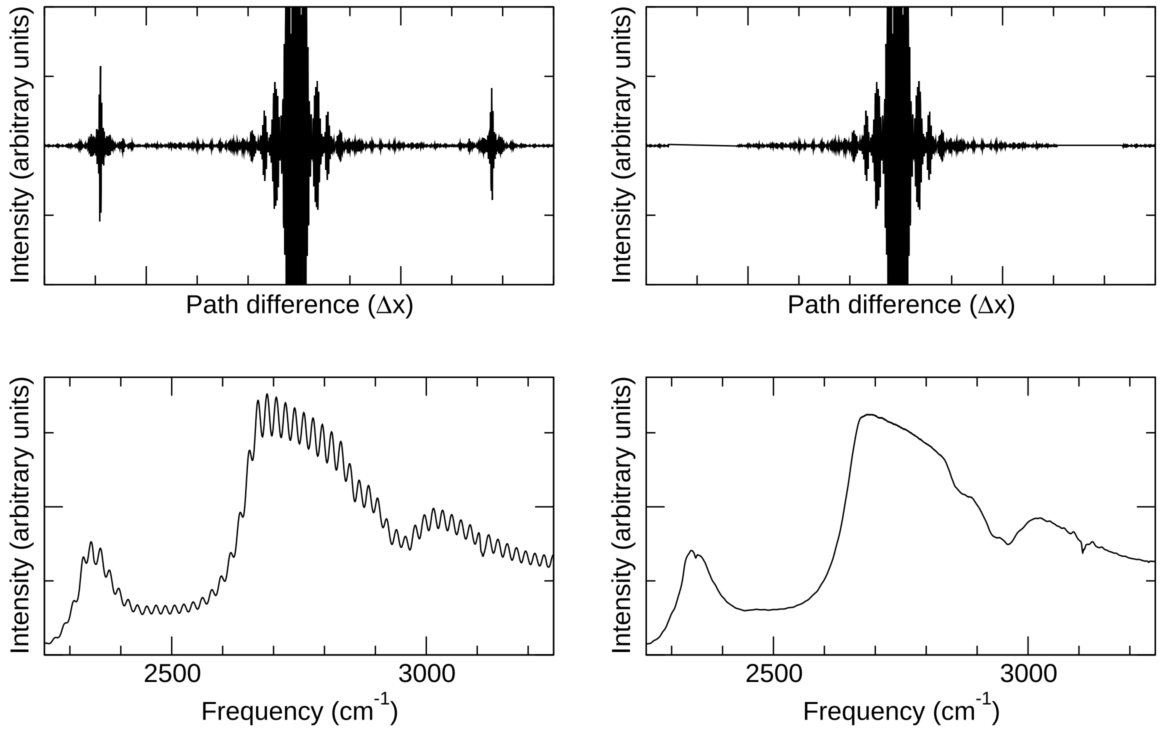

Figure 4.25: Effect of Fabry-Perot interference. Top left: Interferogram from diamond anvil cell. The two large peaks flanking the center peak are responsible for the Fabry-Perot interference. Bottom left: Fabry-Perot interfence appears as a "ripple" in the spectrum. Top right: "Zapping" the flanking peaks removes the Fabry-Perot interference. Bottom right: Corrected spectrum.

for a range between $1600\,\text{cm}^{-1}$ and $7000\,\text{cm}^{-1}$ [26].

When collecting the interferogram for a diamond anvil cell, we compensated for the effect of *Fabry-Perot interference.* Diamond has a high refractive index, and the culets and tables of the diamonds were kept as flat and parallel as we could acheive. Consequently, as infrared light passed through the DAC, it reflected from all the interfaces and interfered with itself. As a result the transmitted intensity through the cell varied with frequency. This interference made it difficult to locate normal modes, as can be seen in figure 4.25. This was compensated for by "zapping" the interferogram; the peaks corresponding to the Fabry-Perot interference are easily located and eliminated.

Because the IR spectrum must be taken in vacuum, to eliminate the strong absorbance of water vapor, carbon dioxide, and other atmospheric components, we did not attempt to control the temperature of the DAC as we did when performing confocal measurements (section 4.1.6). Ambient temperature in the lab was usually about 297 K. The purpose of controlling the temperature of the DAC was to ensure accurate pressure measurements. This accuracy was ensured at ambient temperature by measuring the fluorescence of a reference ruby at ambient pressure and temperature before measuring the fluorescence of the ruby in the DAC (section 4.1.5).

4.4 Bibliography

[1] A. Jayaraman. Diamond anvil cell and high pressure physical investigations. *Reviews of Modern Physics*, 55:65–108, 1983.

[2] C. D. Clark, R. W. Ditchburn, and H. B. Dyer. The absorption spectra of natural and irradiated diamonds. *Proceedings of the Royal Society of London A*, 234:363–381, 1956.

[3] A. Zeitzev, editor. *Optical properties of diamond: a data handbook*. Springer, 2001.

[4] L. Merrill and W. A. Basset. Miniature diamond anvil cell for single crystal x-ray diffraction studies. *Review of Scientific Instruments*, 45:290–294, 1974.

[5] D. Ragan, R. Gustavsen, and D. Schiferl. Calibration of the ruby R_1 and R_2 fluorescence shifts as a function of temperature from 0 to 600 K. *Journal of Applied Physics*, 72:5539–5544, 1992.

[6] O. Grasset. Calibration of the R ruby fluorescence lines in the pressure range [0 - 1 GPa] and the temperature range [250 - 300 K]. *High Pressure Research*, 21:139, 2001.

[7] S. Sharma and Y. M. Gupta. Theoretical analysis of r-line shifts of ruby subjected to different deformation conditions. *Physical Review B*, 43:879–893, 1991.

[8] SA1-RTD Product Manual M0503C/0608. OMEGA Engineering, Inc., http://www.omega.com/manuals/index.html, 2008.

[9] Temperature control: tuning a pid (three-mode) controller. OMEGA Engineering, Inc., http://www.omega.com/temperature/Z/pdf/z115-117.pdf, 2003-2009.

[10] M. Minsky. Memoir on inventing the confocal microscope. *Scanning*, 10:128–138, 1988.

[11] J. Pawley, editor. *Handbook of biological confocal microscopy.* Springer, 1995.

[12] W.S. Rasband. ImageJ. U. S. National Institutes of Health, Bethesda, Maryland, http://rsb.info.nih.gov/ij/, 1997-2009.

[13] S. Wilhelm, B. Gröbler, M. Gluch, and H. Heinz. Confocal laser scanning microscopy: principles. Carl Zeiss Jena GmbH, http://www.zeiss.de/lsm, 2003.

[14] M. D. McCluskey, B. D. Riley, A. M. Perenchio, and M. Knoblauch. Confocal microscopy of water under static pressure. In M. Elert, M. D. Furnish, R. Chau, N. Holmes, and J. Nguyen, editors, *Shock Compression of Condensed Matter - 2007 (the Proceedings of the 15th APS Topical Conference on Shock Compression of Condensed Matter)*. American Institute of Physics, 2007.

[15] A. E. Siegman. *Lasers.* University Science Books, 1986.

[16] A. Gerrard and J. M. Bruch. *Introduction to matrix methods in optics.* Wiley Interscience, 1975.

[17] H. Kogelnik and T. Li. Laser beams and resonators. *Applied Optics*, 5:1150, 1966.

[18] W. J Firth and R. G. Harrison, editors. *Lasers: physics, systems and techniques.* SUSSP Publications, 1982.

[19] William T. Silvfast. *Laser fundamentals.* Cambridge University Press, 2004.

[20] S. A. Self. Focusing of spherical gaussian beams. *Applied Optics*, 22:658–661, 1983.

[21] M. J. Weber, editor. *Handbook of optical materials.* CRC Press, 2003.

[22] G. J. Hanna and M. D. McCluskey. Measuring the volume of a fluid in a diamond anvil cell using a confocal microscope. *Applied Optics*, 48:1758–1763, 2009.

[23] G. J. Hanna and M. D. McCluskey. Confocal microscopy to measure the volume of a fluid in a diamond anvil cell. In M. Elert, M. D. Furnish, R. Chau, N. Holmes, and J. Nguyen, editors, *Shock Compression of Condensed Matter - 2009 (the Proceedings of the 16th APS Topical Conference on Shock Compression of Condensed Matter)*, page (in press). American Institute of Physics, 2009.

[24] R. Bell. *Introductory Fourier transform spectroscopy.* Academic Press, 1972.

[25] P. Griffiths and J. de Hasseth. *Fourier transform infrared spectroscopy.* John Wiley and Sons, 1986.

[26] S. Jokela. *Stability and structure of hydrogen defects in zinc oxide.* PhD thesis, Washington State University, 2006.

Chapter 5

Experimental results

5.1 Confocal data

In this section we present the results of our refractive index and volume measurements for argon at high pressure. These data are interesting in their own right, but they will also serve to establish confocal microscopy as a viable technique for measuring fluid volumes and refractive indices.

5.1.1 Equation of state for argon at 300 K

Each confocal microscopy experiment was performed by first loading a DAC with argon as described in section 4.1. Then the reflected intensity profile was measured as described in section 4.2.6. The pressure was adjusted in small increments by tightening only three of six screws at one time. The ruby fluorescence was stimulated by the mercury lamp of the confocal microscope, and collected by a 0.5 mm optical fiber. The location of the R_1 peak was determined with an Ocean Optics spectrometer. Once pressures of about 6 GPa were attained, the experiment was ended, and a new cell prepared and loaded for the next experiment. (We chose to end the experiments at 6 GPa

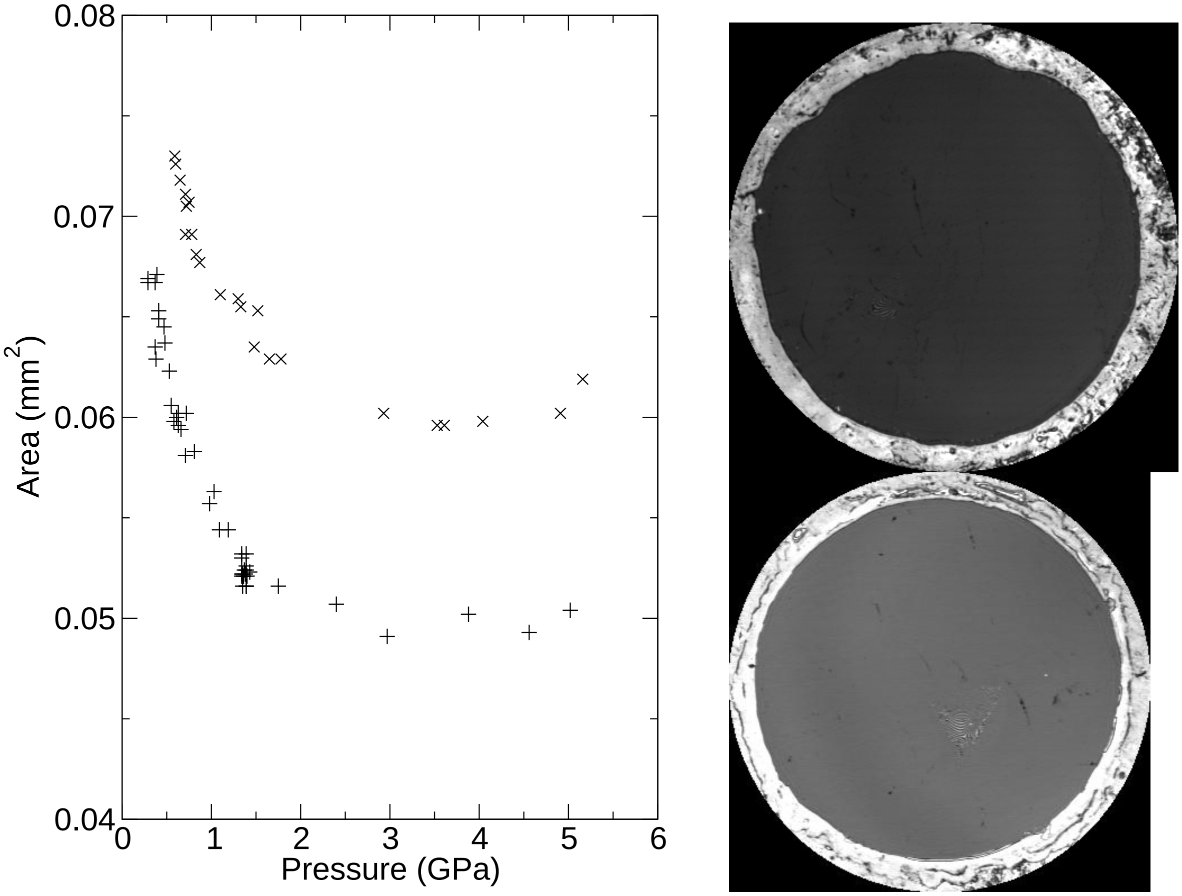

Figure 5.1: Left: Area of sample in DAC as a function of pressure. + and X denote separate experiments. Right: Images of sample areas for X (top) and + (bottom) showing the difference in size between experiments.

because at that pressure we had enough solid-phase data to determine the mole number of the sample, as described below.)

The resulting image stacks were processed into reflected intensity profiles as described in section 4.2.6. Each peak was fitted to the Taylor expansion (equation 4.41) and its location and height were used to calculate the optical thickness and refractive index of the sample for each pressure, as described in section 4.2. Areas were determined as described in section 4.2.7.

The area, optical thickness, and refractive index measurements are plotted as functions of pressure in figures 5.1, 5.2, and 5.3.

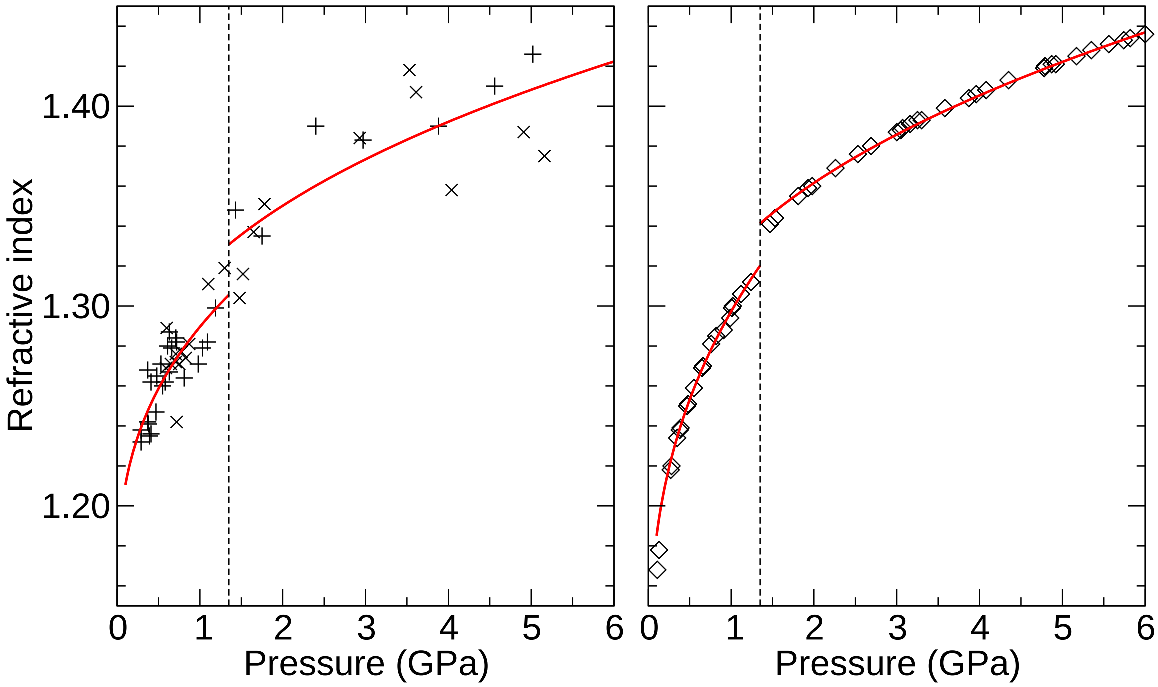

Figure 5.2: Left: Refractive index as a function of pressure as measured by confocal microscopy. + and X denote separate experiments. Red lines: fits to fluid and solid data (table 5.1). Right: Refractive index from reference [1]. Red lines: fits to fluid and solid data (table 5.1).

The area does not seem always to decrease with increasing pressure. We do estimate an uncertainty of about 1 % in the area measurement, but we think the irregular changes in area have something to do with the response of the gasket to sudden changes in pressure. Presumably gaskets of different materials will respond differently, but we have not investigated this systematically. At high enough pressures, argon becomes stiffer than the metal gasket, and this explains why the area stops decreasing at higher pressures.

Optical thickness seems always to decrease with increasing pressure, although one or two exceptions may be seen in figure 5.3. As with area, we attribute this behavior to the material properties of the gasket, and we have not investigated it systematically. Around 1.35 GPa there are many points where the optical thickness is decreasing but

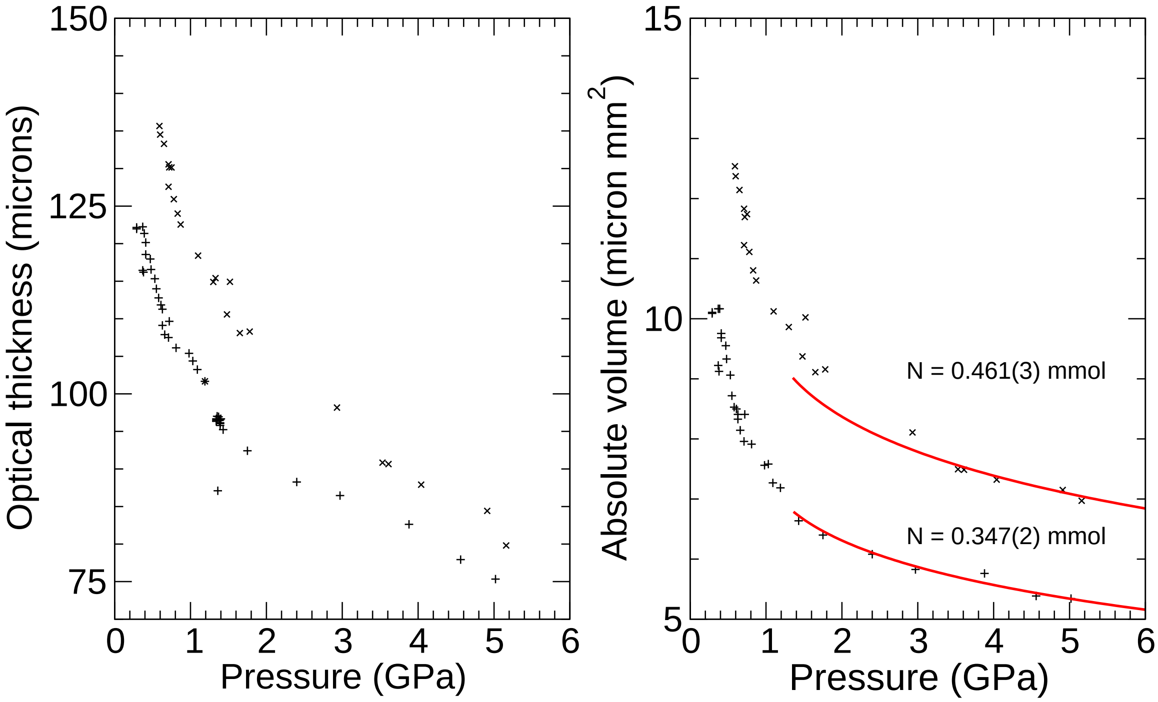

Figure 5.3: Data from confocal microscopy of argon in DAC. + and X denote separate experiments. Left: Optical thickness as pressure increases. Right: Absolute volumes of sample as pressure increases. Red lines: Fit to XRD pressure-volume data of solid at ambient temperature [1], with mole number N of sample as adjustable parameter.

the pressure is not increasing, and this is the phase transition from fluid to solid. This may be visually confirmed in the microscope images.

We show refractive index, along with fits to calculated values [1], in figure 5.2. We excluded all points with pressures between 1.3 GPa and 1.4 GPa, because the calculation that produces refractive index from peak heights is meaningless if fluid and solid argon are both present. We chose to exclude pressure within 50 MPa of the phase transition for two reasons. First, the pressure measurements are only precise to about 20 MPa. Second, the difference in refractive index between fluid and solid argon is small (less than 0.1) and sometimes it is difficult to see the solid argon. The problem is much the same as trying to photograph ice in water under bright light.

Fitting the refractive index to a function of pressure is tricky, because the refractive

	fluid		solid	
	a	b	a	b
reference	0.13738	0.00197	0.08011	0.13022
This work	0.09632	0.09385	0.07739	0.12705

Table 5.1: Fitting parameters for pressure as a function of refractive index.

index of argon is really a function of density, described by the Clausius-Mossotti relation

$$\frac{n^2-1}{n^2+2}=\frac{1}{3}\alpha\rho, \tag{5.1}$$

where α is the polarizability of an argon atom (appendix D). Pressure, however, can be expressed as a polynomial in density, via the virial equation of state (section 3.3); and the equation of state of argon (whether solid or fluid) is approximately cubic (equation 5.3). This allows us to linearize the data,

$$\frac{n^2-1}{n^2+2}=a\left(\frac{P}{P_0}\right)^{1/3}+b, \tag{5.2}$$

where a and b are the fitting parameters and $P_0 = 1.35\,\mathrm{GPa}$, the freezing pressure at 300 K, is a convenient scaling factor. The parameters are given, to a convenient number of figures, in table 5.1; the resulting functions $n(P)$ are plotted in figure 5.2. The root-mean-square deviation of our data from the fits to the reference data is 0.02, and so we estimate the absolute error on our index data to be 0.02.

Absolute volumes are plotted in figure 5.3. They are the product of area, optical thickness, and fitted refractive index. As with refractive index, the data with pressures between 1.3 GPa and 1.4 GPa were excluded. The solid phase data were fitted to a published equation of state produced from X-ray diffraction data [1]:

$$P = A_0 + A_1\rho + A_2\rho^2 + A_3\rho^3. \tag{5.3}$$

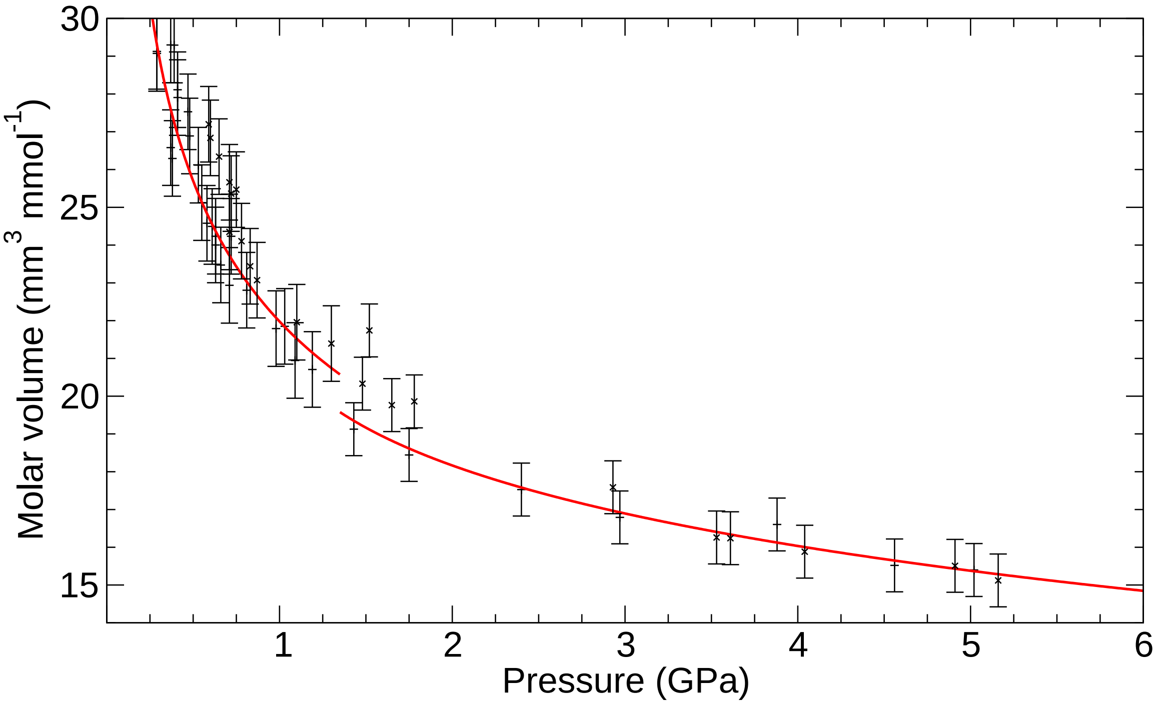

Figure 5.4: Measured equation of state of argon. + and X denote separate experiments. Red lines: fits to experimental 300 K isotherm [2] and XRD pressure-volume data at ambient temperature [1].

We rewrote ρ as N/V and fitted our absolute volumes using N as the fitting parameter. This gave us the number of moles N of argon in our samples, which are shown in figure 5.3, which we used to convert our absolute volumes into molar volumes, shown in figure 5.4. N can be roughly estimated from the density of liquid argon at the boiling point ($1.394 \times 10^{-3}\,\mathrm{g\,mm^{-3}}$), the atomic mass of argon ($0.039\,948\,\mathrm{g\,mmol^{-1}}$), and the volume of the hole drilled in the gasket ($\frac{1}{4}(0.29\,\mathrm{mm})^2(0.150\,\mathrm{mm})$), which yields $N = 0.350\,\mathrm{mmol}$.

The root mean square deviation of molar volume from the published equation of state, for the solid data, is $0.7\,\mathrm{mm^3\,mmol^{-1}}$; for the fluid data it is $1\,\mathrm{mm^3\,mmol^{-1}}$.

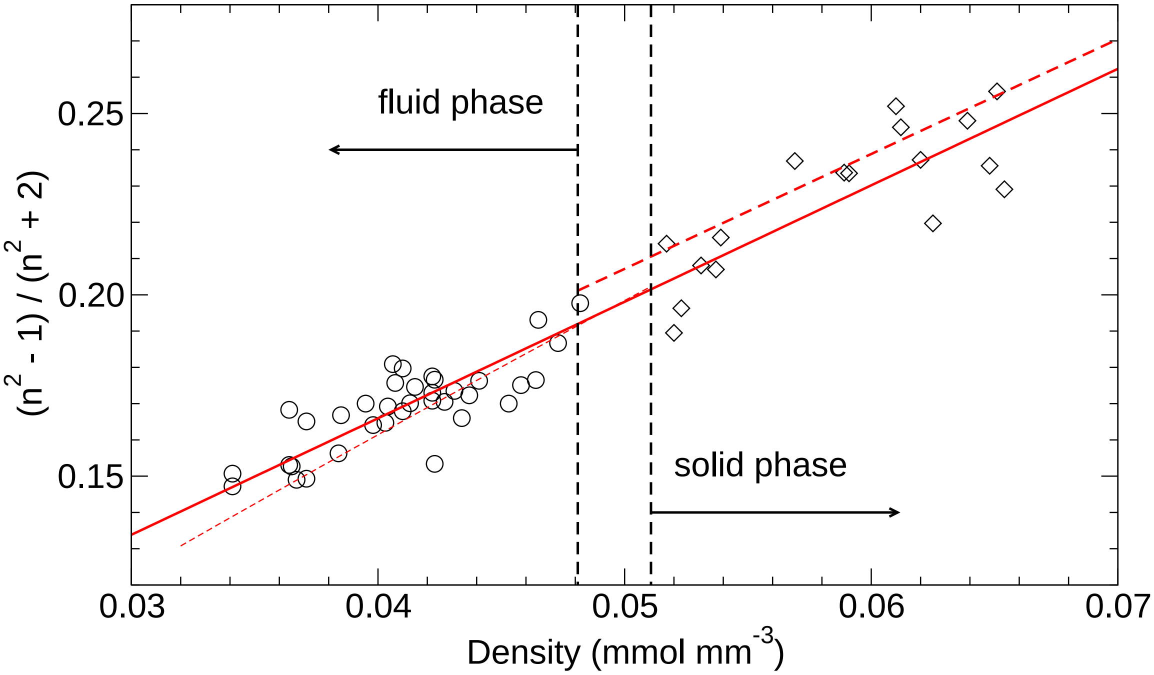

Figure 5.5: Clausius-Mossotti relation. Circles and diamonds denote fluid and solid data repectively. Solid red line: fit to confocal data (slope = $3.21(14)\,\mathrm{mm}^3\,\mathrm{mmol}^{-1}$, intercept = $0.037(6)$). Dashed red lines: fit to published liquid data [3] and calculated solid data [1]. Density is calculated from the measured pressure via the appropriate equation of state [1, 2], $(n^2-1)/(n^2+2)$ is calculated using the measured index. Error bars are omitted for clarity; the error on the density is about $0.002\,\mathrm{mmol}\,\mathrm{m}^{-3}$, and the error on C_{CM} is about 0.007.

5.1.2 Refractive index and Clausius-Mossotti relation

For the purpose of measuring volume we assumed that refractive index is a function of pressure. But it is only indirectly a function of pressure, because pressure is itself a function of density through the equation of state.

Density and refractive index are related through the Clausius-Mosotti relation [4]

$$C_{CM} = \frac{n^2-1}{n^2+2} = \frac{1}{3}\rho\alpha, \tag{5.4}$$

where n is refractive index, ρ is number density, and α is polarizability of the argon atom. The relation is derived by treating each atom as being in a spherical “hole” in

	$\alpha(\text{Å}^3)$
This work	1.77(8)
Lallemand (1977) [5]	1.643

Table 5.2: Polarizability of argon.

an isotropic linear dielectric medium, which is polarized by an incident electromagnetic wave. α depends on the structure of the atom, which should be independent of pressure for any pressures achieved in this work, and the field the atom experiences from the other atoms that make up the dielectric. Therefore changes in α indicate changes in the structure of the dielectric, besides the change in density.

In figure 5.5, we plot the left-hand side of equation 5.4, calculated from the measured refractive index for each pressure, against the density (calculated from the molar volume v using the fitted refractive index). The uncertainty is calculated in the standard way:

$$\rho = \frac{1}{v} \tag{5.5}$$

$$\frac{\Delta\rho}{\rho} = \frac{\Delta v}{v} \tag{5.6}$$

$$C_{CM} = \frac{n^2-1}{n^2+2} \tag{5.7}$$

$$\frac{\Delta C_{CM}}{C_{CM}} = 2n\Delta n\left(\frac{1}{(n^2+1)^2}+\frac{1}{(n^2-1)^2}\right)^{1/2} \tag{5.8}$$

$$\frac{\Delta v}{v} = 0.02 \tag{5.9}$$

$$\Delta n = 0.01 \tag{5.10}$$

Our data, whether in the solid or fluid phase, seem all to lie on the same line, which would indicate that the polarizability of argon is not affected, within the experimental uncertainty, by phase or density over the range of pressures we studied. Our data are consistent with published estimates of polarizability (table 5.2).

5.1.3 Discussion - confocal data

Because argon is a substance extensively studied, well understood, and readily available, it is an ideal substance on which to test and refine a new technique of measurement. The agreement of our confocal data, both for refractive index and equation of state, with the literature indicates that the technique is viable for "optically simple" substances.

The refractive index of argon at high pressure has been previously measured to a precision of only about 4 % [6]; our precision is about 2 %.

5.2 FTIR data

Argon is a spherical atom and consequently absorbs very little infrared. Previous work done in our research group [7] showed that the infrared absorption of carbon dioxide, which is usually present in cryogenically loaded DACs, can be used as a pressure standard. One interesting feature is that the frequency as a function of pressure shows discontinuities at phase transitions, as illustrated for carbon dioxide in nitrogen at ambient temperature. (figure 5.6).

Carbon dioxide dissolved in argon would also be a useful pressure standard. In addition, the discontinuities at phase transitions indicate that the frequency of dissolved carbon dioxide is somehow dependent on the structure of the solvent. Figure 5.7 shows a representative absorption spectrum for a diamond anvil cell loaded with argon and carbon dioxide.

According to matrix isolation studies [9], carbon dioxide occupies two sites in the argon fcc lattice. Using this information we calculated frequency as a function of argon density using Gaussian03 (the B3LYP method), in three different ways: 1) a carbon dioxide molecule, surrounded by fixed nearest-neighbor argon atoms, using the LANL2DZ basis set, 2) a carbon dioxide molecule, surrounded by fixed nearest-neighbor

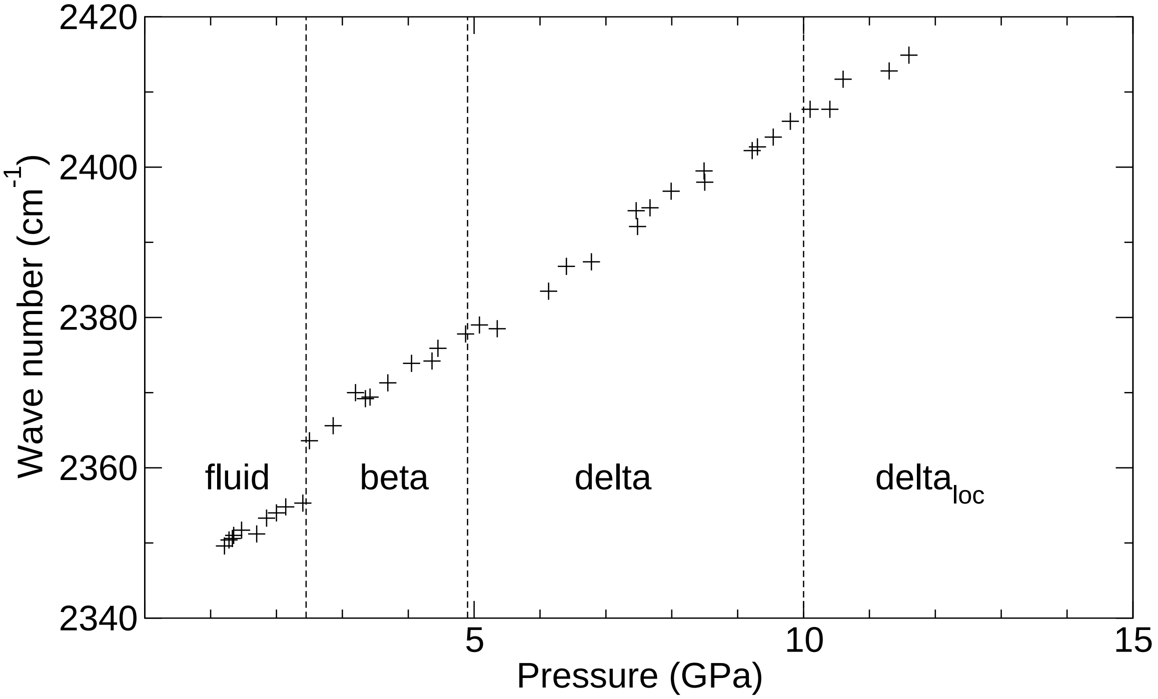

Figure 5.6: Frequency of carbon dioxide in nitrogen, as a function of pressure, at ambient temperature. Dashed lines: phase transitions [8].

argon atoms, using the aug-cc-PVDZ basis set, and 3) a carbon dioxide molecule, surrounded by nearest- and second-nearest-neighbor argon atoms, with the nearest-neighbors free to move, using the LANL2DZ basis set. (The free nearest neighbors did not move significantly.) The results are shown in figure 5.8, scaled by the carbon dioxide frequency at “zero density” (no neighbors) for each basis set.

Using published equations of state [1, 2], we able to plot the frequencies, determined by FTIR spectroscopy, of carbon dioxide in argon as a function of the density of argon, as shown in figure 5.9. The concentration of carbon dioxide is estimated to be 0.08 mmol cm^{-3}, using the area of the absorbance peaks in the solid [10] and the estimated gasket thickness from figure 5.3.

Like the experimental data for the solid, the Gaussian data is apparently linear for densities between 0.04 mmol mm^{-3} and 0.07 mmol mm^{-3}. But one important difference

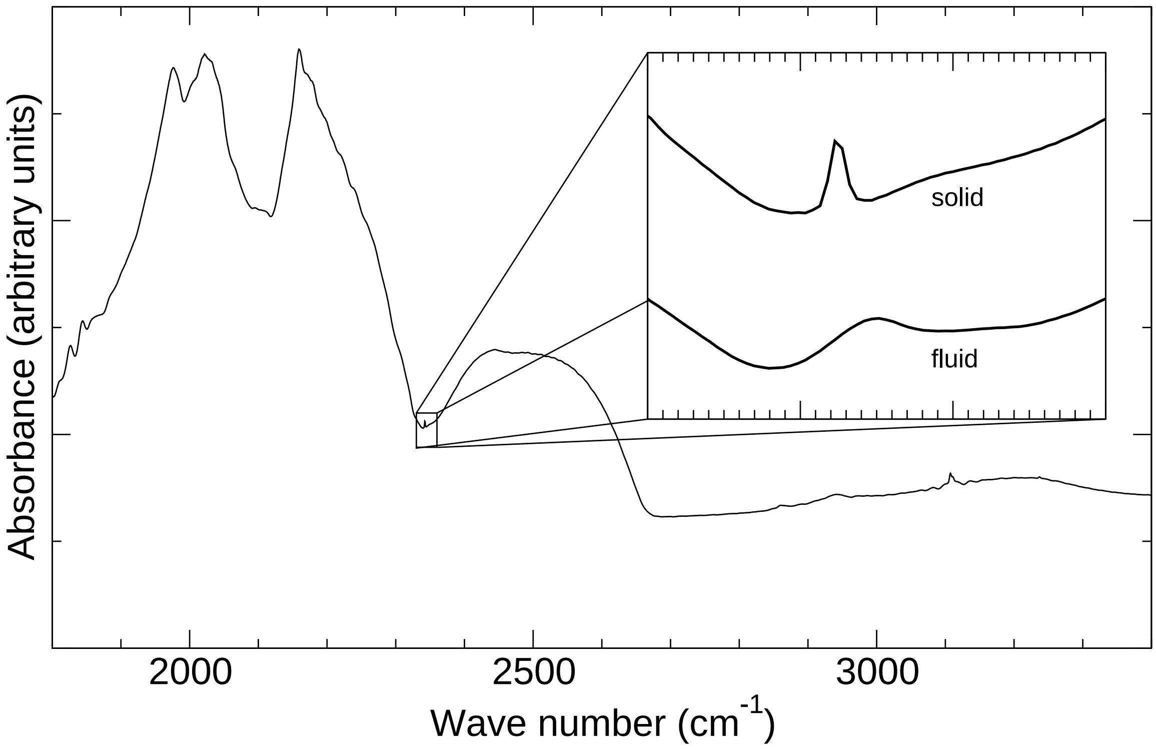

Figure 5.7: Absorption spectrum of a diamond anvil cell loaded with argon and carbon dioxide. Inset: The absorption peak of carbon dioxide. The carbon dioxide peak in the solid is much sharper than that in the fluid; this is most likely due to the disordered nature of the fluid, where the local density of argon atoms varies. Argon itself absorbs little infrared.

is that the Gaussian data goes to the zero pressure frequency of carbon dioxide, and the experimental data is always below that pressure (2349 cm^{-1}). The matrix isolation data [9, 11] shows the same effect, as illustrated in figure 5.9.

Figure 5.10 shows the width of the IR peaks of carbon dioxide in argon and nitrogen. In argon the peaks become noticeably sharper in the solid phase, but in nitrogen we do not observe this.

5.2.1 Discussion - FTIR data

We are the first, to our knowledge, to measure the frequency of carbon dioxide as a function of pressure in argon and nitrogen. We find that Gaussian calculations overes-

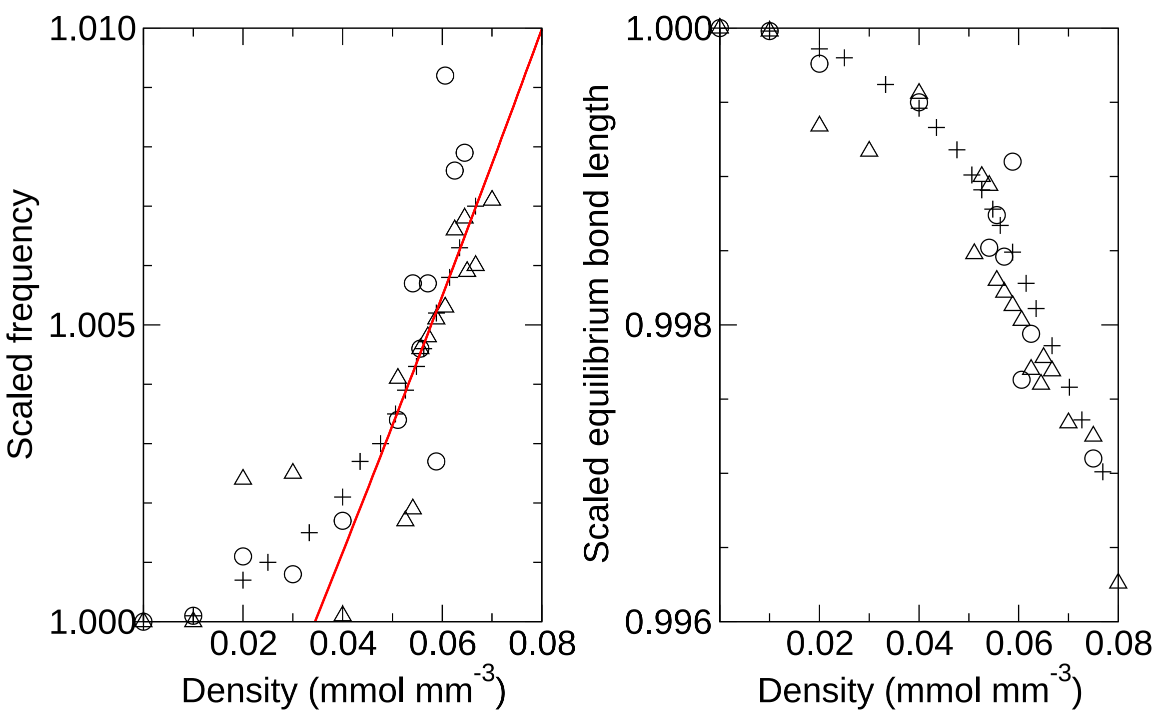

Figure 5.8: Left: frequencies of asymmetric stretching mode of carbon dioxide in solid argon, calculated by Gaussian. Red line: fit to equations 5.14 and 5.15. Only the LANL nearest-neighbor data (+) was fitted, and only for densities greater than $0.04\,\mathrm{mmol\,mm^{-3}}$. Right: Equilibrium C-O bond length for carbon dioxide in solid argon, calculated by Gaussian. Diamonds: LANL second-nearest-neighbor calculation, with nearest neighbors free to move. Circles: aug-cc nearest-neighbor calculation.

timate the frequency shift. To explain these data, we propose a rather simple model for the carbon dioxide-argon interaction.

We assume that we have isolated carbon dioxide molecules. Because the cell is loaded at liquid argon temperatures, as it warms up both argon and carbon dioxide pass through gas states and are presumably well-mixed by the time the cell reaches its equilibrium pressure and temperature.

Suppose that each argon atom interacts with an oxygen atom, according to a Lennard-Jones potential, not necessarily of the 12-6 type, $V_{ArO}(r)$, where r is the distance from an argon atom to an oxygen atom on the z-axis at z. The oxygen atoms would be subject to a nearly harmonic potential from the carbon atom; and near equi-

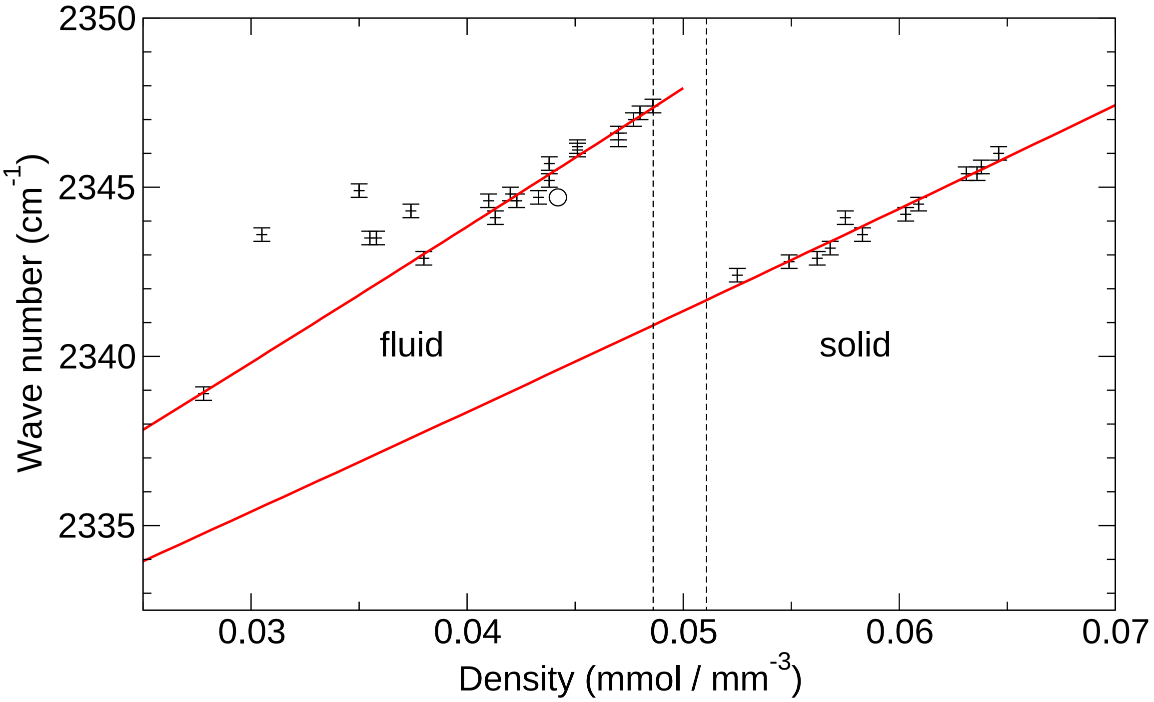

Figure 5.9: Frequency of carbon dioxide in argon at ambient temperature. Red lines: fits to equations 5.14 and 5.15. Dashed lines: phase boundaries. The pressures are converted to densities by equations of state for the fluid phase [2] and the fcc phase [1]. Circle: Frequency of carbon dioxide in argon matrix isolation at 10 K [11]. The density of the argon matrix is estimated by interpolation from the solid equations of state at 4 K and 20 K [12].

librium, a nearly harmonic potential from the argon atoms.

This potential could be written as an integral over all space, if the distribution of argon atoms in space were known. Assuming that the argon atoms are distributed symmetrically about the longitudinal axis of the carbon dioxide molecule (which they are in an fcc solid), this potential would depend only on the z-coordinate of the oxygen atom. Near equilibrium the potential would be approximately harmonic, and we can write the total force on each oxygen atom as

$$F_O = -k_0(z - z_{eq}) - k_\rho(z - z_{eq}), \tag{5.11}$$

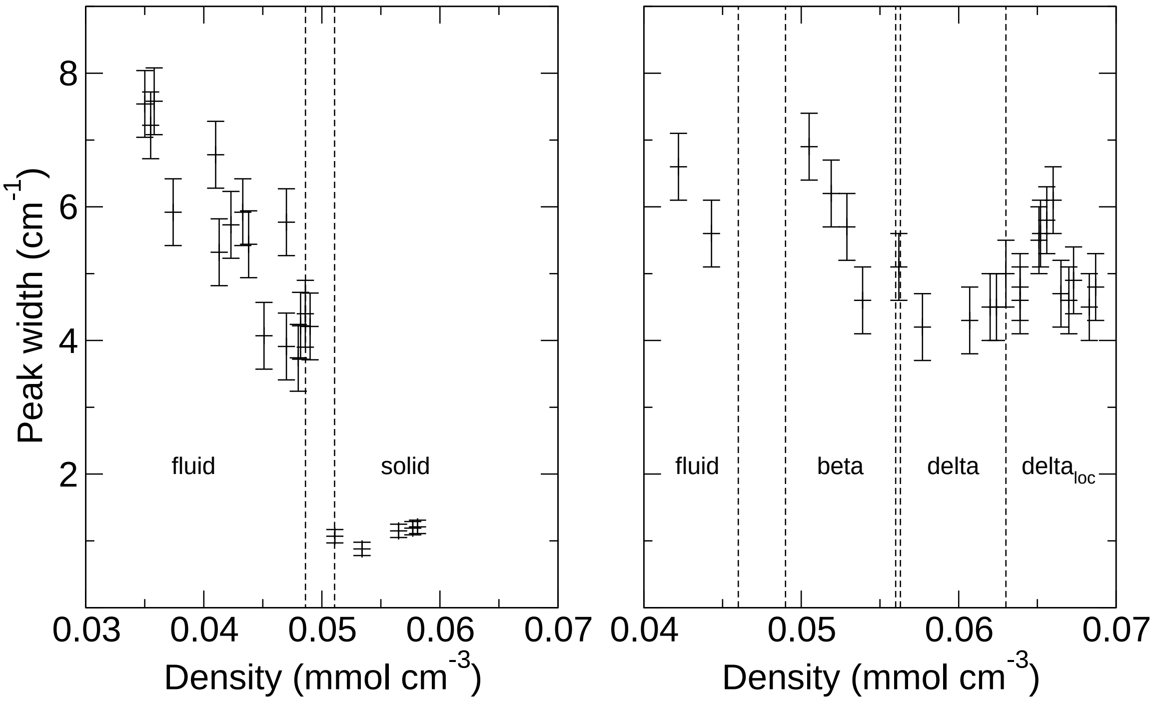

Figure 5.10: Widths of IR peaks of carbon dioxide as a function of argon and nitrogen densities.

where k_0 is the force constant of the carbon-oxygen interaction, k_ρ the force constant due to the argon-oxygen interaction, and z_{eq} the equilibrium position for the oxygen atoms.

Solving for the normal modes of the the carbon-dioxide molecule in the standard way gives, for the asymmetric IR-active mode,

$$\omega^2 = \frac{m_C(k_0 + k_\rho) + 2k_0 m_O}{2m_O m_C}\left[1 + \left(1 - \frac{8k_0 k_\rho m_O m_C}{[m_C(k_0 + k_\rho) + 2k_0 m_O]^2}\right)^{1/2}\right] \tag{5.12}$$

where m_C, m_O are the masses of the carbon and oxygen atoms, respectively. If k_ρ is positive, then the frequency will increase, and if negative the frequency will decrease, with respect to the frequency of an isolated carbon dioxide molecule.

If the distribution of argon atoms in space is known (for the solid, it is the fcc

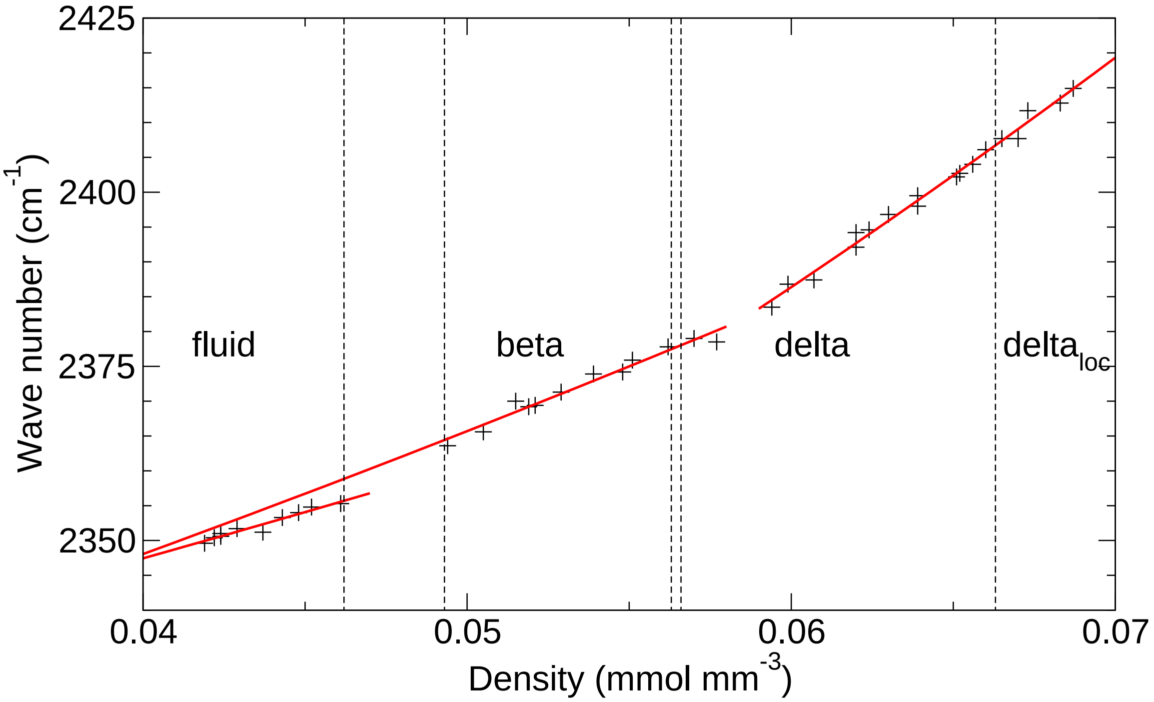

Figure 5.11: Frequency of carbon dioxide in nitrogen at ambient temperature. Red lines: fits to equations 5.14 and 5.15. Dashed lines: phase boundaries [8]. The δ-δ_{loc} phase boundary does not involve a change in molar volume. The pressures are converted to densities by equations of state for the fluid phase [13] and the β and δ phases [8]. Very few points have been measured for the β equation of state.

lattice), then k_ρ may be found from

$$\frac{1}{2}k_\rho(z-z_{eq})^2 = \rho\int g(x',y',z')V_{ArO}\,dx'dy'dz', \tag{5.13}$$

where ρ is the number density of the argon atoms and $g(x',y',z')$ dimensionlessly represents the distribution of the argon atoms in space. It follows that k_ρ must be directly proportional to ρ, and so we write

$$k_\rho = A\rho + B; \tag{5.14}$$

so that the force constant has a density-dependent and a density-independent part

	A ($\mathrm{mm^3\,mmol^{-1}}$)	B
Gaussian ($\rho \geq 0.4\,\mathrm{mmol\,mm^{-3}}$)	5.63(9)	-0.194(5)
Fluid argon ($\rho \geq 0.4\,\mathrm{mmol\,mm^{-3}}$)	4.74(3)	-0.25(1)
Solid argon	3.55(2)	-0.26(1)
Fluid nitrogen	15.1(13)	-0.622(6)
β nitrogen	19.6(11)	-0.79(6)
δ & δ_{loc} nitrogen	31.0(7)	-1.46(5)

Table 5.3: Fit parameters for the model given in equation 5.14.

(which might depend on other parameters such as temperature).

If each phase has a different $g(x', y', z')$, we can expect the constant A to change with phase transitions. We can also expect that k_ρ is dominated by the nearest argon atoms to the oxygen atoms, because interactions between neutral atoms fall off faster than r^{-2}. A change in the constants A and B might imply a local change in density; for example, in the fluid argon atoms might tend to crowd around the carbon dioxide, making the frequency less sensitive to changes in overall number density.

We can simplify things somewhat by writing 5.12 dimensionlessly in terms of the asymmetric mode of an isolated carbon dioxide atom, ω_0:

$$\left(\frac{\omega}{\omega_0}\right)^2 = \frac{1}{2}\left(1 + \frac{\mu\kappa}{\mu + 2}\right)\left[1 + \left(1 - \frac{8\mu\kappa}{[\mu(1+\kappa)+2]^2}\right)^{1/2}\right], \tag{5.15}$$

where $\mu = m_C/m_O$ and $\kappa = k_\rho/k_0$.

The fits to the experimental data to this model are shown in figure 5.9 and 5.11, and the fit parameters given in 5.3.

From the table we learn that the density-independent part of the force constant for argon does not change, within the estimated error, but the density-dependent part changes significantly. The solid argon density dependence is also significantly different from that of the Gaussian calculations, suggesting that the argon lattice distorts in some way near the carbon dioxide molecule. In the case of nitrogen, the density dependence

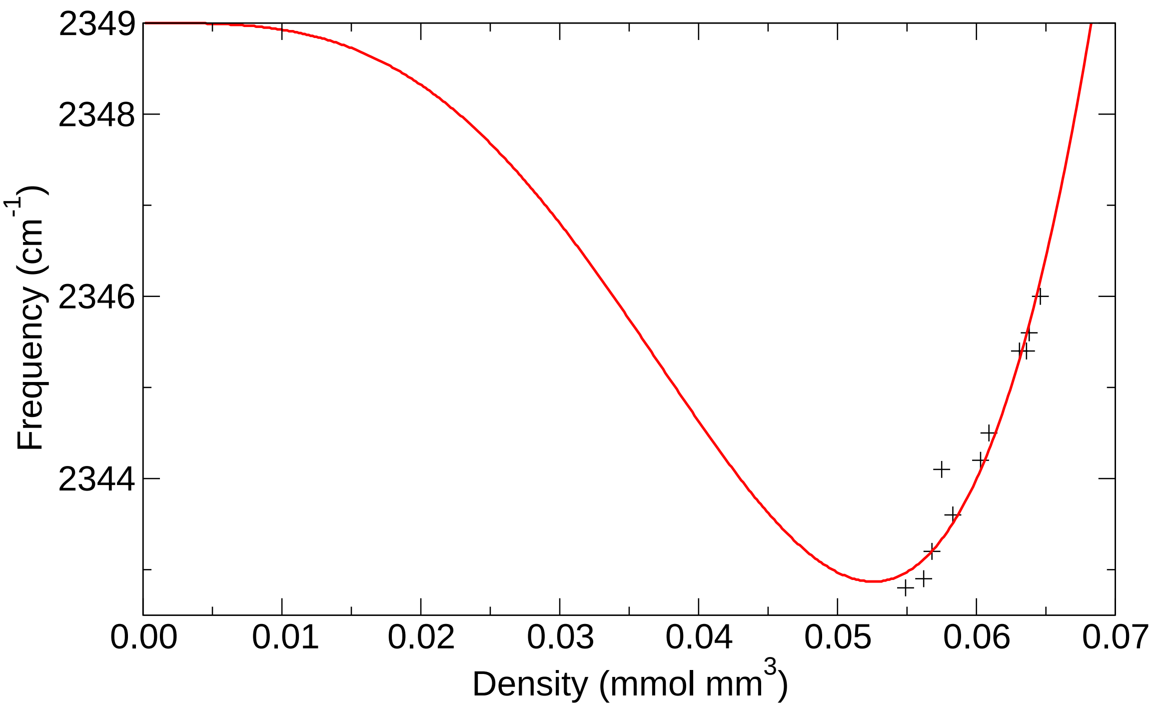

Figure 5.12: Frequency of carbon dioxide in solid argon at ambient temperature. Red lines: fit to density-dependent force constant assuming isotropic Lennard-Jones interaction for argon and oxygen.

changes a great deal, and the density-independent part of the δ-phase force constant changes significantly from that of the fluid and β phases.

We can explain the approximately linear dependence of force constant on density in another way. First we assume that each oxygen atom interacts with each argon atom according to an isotropic Lennard-Jones potential, and each oxygen atom interacts with the carbon atom according to a harmonic potential. We can calculate the total potential energy of the oxygen atoms and Taylor expand the potential energy about the C - O equilibrium bond length to derive the density-dependent force constant k_ρ. Using a 12-6 Lennard-Jones potential with parameters σ, ϵ, and argon atoms in an fcc lattice of interatomic separation a, we find

$$\begin{aligned} k_\rho \approx & - 4\frac{\epsilon}{\sigma^2}\left(41625.024\frac{z_0^4}{a^4} - 10035.576\frac{z_0^2}{a^2} - 326.964\right)\left(\frac{\sigma}{a}\right)^{14} \\ & + 4\frac{\epsilon}{\sigma^2}\left(2533.968\frac{z_0^4}{a^4} - 1918.194 z_0^2 a^2 + 10.164\right)\left(\frac{\sigma}{a}\right)^{8}, \end{aligned} \tag{5.16}$$

where z_0 is the C - O bond length for the free carbon dioxide molecule. Using this expression for k_ρ and treating ϵ and σ as fitting parameters we find the frequency as a function of density in figure 5.12. In the range of solid pressures measured in this work we see the approximately linear behavior discussed previously, but as the solid density approaches zero the frequency increases to the frequency of the free carbon dioxide molecule. This model of an isotropic argon - oxygen potential is too simplistic. There should also be an argon-carbon interaction. A more realistic model would complicate the density-dependent force constant relation derived here. However, from this simple model we can conclude that van der Waals forces are largely responsible for the frequency dependence at lower densities. This explains the discrepancy between the Gaussian calculations and the experimental data; density functional theory calculations do not replicate van der Waals forces.

An accurate argon - carbon dioxide potential determined from the solid argon data would help us to understand the behavior in the liquid; the difference between liquid and solid behavior would be attributed then to the local density of the argon atoms near the carbon dioxide molecule.

5.3 Bibliography

[1] M. Grimsditch, P. Loubeyre, and A. Polian. Brillouin scattering and three-body forces in argon at high pressure. *Physical Review B*, 33:7192–7200, 1986.

[2] Ch. Tegeler, R. Span, and W. Wagner. A new equation of state for argon covering the fluid region for temperatures from the melting line to 700 K at pressures up to 1000 MPa. *Journal of Physical Chemistry Reference Data*, 28:779–850, 1998.

[3] H. Hochheimer, K. Weishaupt, and M. Takesada. High pressure Brillouin scattering study of dense argon and nitrogen. *Journal of Chemical Physics*, 105:374–378, 1996.

[4] R. Feynman, R. Leighton, and M. Sands. *The Feynman lectures on physics*. Addison-Wesley, 1965.

[5] M. Lallemand and D. Vidal. Variation of the polarizability of noble gases with density. *Journal of Chemical Physics*, 66:4776–4780, 1977.

[6] M Grimsditch, R. Letoullec, A. Polian, and M. Gauthier. Refractive index determination in diamond anvil cells: results for argon. *Journal of Applied Physics*, 60:3479–3481, 1986.

[7] M. McCluskey and K. Zhuravlev. N_2 and CO_2 vibrational modes in solid nitrogen under pressure. *Journal of Chemical Physics*, 116:1607–1612, 2002.

[8] V. Manzhelii and Y. Freiman, editors. *Physics of cryocrystals*. American Institute of Physics, 1997.

[9] M. J. Irvine, J. G. Matheson, and A. D. E. Pullin. The infrared matrix isolation spectra of carbon dioxide. ii argon matrices: the CO_2 monomer bands. *Australian Journal of Chemistry*, 35:1971–1977, 1982.

[10] H. Yamada and W. Person. Absolute infrared intensities of the fundamental absorption bands in solid CO_2 and N_2O. *Journal of Chemical Physics*, 41:2478–2487, 1964.

[11] J. Castano, A. Fantoni, and R. Romano. Matrix isolation FTIR study of carbon dioxide: reinvestigation of the CO_2 dimer and $CO_2 \ldots N_2$ complex. *Journal of Molecular Structure*, 881:68–75, 2008.

[12] M. S. Anderson and C. A. Swenson. Experimental equations of state for the rare gas solids. *Journal of Physics and Chemistry of Solids*, 36:145–162, 1975.

[13] R. Span, E. Lemmon, T. Jacobsen, W. Wagner, and A. Yokozeki. A reference equation of state for the thermodynamic properties of nitrogen for temperatures from 63.151 to 1000 K and pressures to 2200 MPa. *Journal of Physical and Chemical Reference Data*, 29:1361–1433, 2000.

Chapter 6

Conclusion

Confocal microscopy of argon

In this work we have developed and demonstrated the use of confocal microscopy to measure fluid volumes and refractive indices in the diamond anvil cell. As far as we are aware, we are the first to do so. Besides being of interest for characterizing materials, refractive index data is needed for Brillouin scattering experiments. Confocal microscopy should prove to be a useful technique for the high-pressure community.

The advantages of confocal microscopy are these: measurements are non-destructive, inexpensive, and quick, and can handle fluids. The disadvantages: the precision is low (a few percent), and the technique is restricted to transparent, optically simple materials with well defined plane interfaces. The low precision is mitigated by the ability to take a great deal of data in a short time at low cost. In addition, confocal microscopy allows for simultaneous and independent measurements of refractive index along with area and optical thickness.

Our confocal measurements of fluid argon seem to be as good as any that exist in the literature; because argon is widely used as a hydrostatic pressure medium in the high-pressure community, this in itself was worth doing. In addition, we have measured the refractive index directly for pressures greater than 0.1 GPa, and these measurements are as good as those in the literature.

FTIR spectroscopy of carbon dioxide in argon and nitrogen

We are the first to determine the frequency of carbon dioxide, as a function of density, in nitrogen and argon. As a probe of structure, the preliminary steps we have taken seem to show some promise. We have shown that the frequency of carbon dioxide in argon and nitrogen is primarily affected density. We have found that the Gaussian calculations overestimate the change in frequency for argon and that van der Waals forces are largely responsible for the low-density behavior of argon.

Further research

Now that the confocal microscopy technique for fluids is worked out, using it to measure some fluids might be a useful occupation. Our search of the literature indicates that the equation of state of the β phase of nitrogen, at ambient temperature, is not well measured; that seems a good place to start. In addition, it might be worth trying to measure the density of water, to see if high-density and low-density water can be distinguished.

Integrating Fabry-Perot interference measurements into the confocal microscopy procedure should improve the estimates of refractive index and sample thickness. The reflected intensity profile gives independent estimates of index n and optical thickness d/n; Fabry-Perot inteference would add an independent estimate of nd.

Further investigation of the interaction of carbon dioxide and argon would be useful in probing the structure of fluid argon. Measurements at very low pressures, for diamond anvil cells, seem like the next logical step; and simulations of carbon dioxide in argon ought not to be too difficult. Simulations might reveal some of the details of the distribution of argon atoms about the carbon dioxide molecule that would improve on the naive model presented here.

What exactly happens as a liquid condenses to a solid? A combination of these techniques with simulations might help to shed some light on this question.

Appendix A

Heitler-London derivation of exchange repulsion

We consider two electrons and two nuclei interacting by Coulomb potentials as shown in figure A.1. We treat the nuclei as fixed and the internuclear separation R as a parameter of the system (Born-Oppenheimer approximation [1]). We define the coordinate system as follows: $\vec{r_1}$ is the position of electron 1 with respect to nucleus 1; $\vec{r_2}$ is the position of electron 2 with respect to nucleus 2; $\vec{R} - \vec{r_1}$ is the position of electron 1 with respect to nucleus 2, and $\vec{R} + \vec{r_2}$ is the position of electron 2 with respect to nucleus 1.

The trial wave function for the electrons, ψ_T, is given in terms of the ground state of the hydrogen atom, $\phi(r)$, where

$$\phi(r) = Ae^{-\frac{r}{a_0}}, \tag{A.1}$$

r is the distance of one electron from one nucleus, a_0 is the Bohr radius, and A is the constant that normalizes $\int \phi^2(r)\, dV$ to 1.

We are interested in the energy of the spin triplet state, which must be antisymmetric

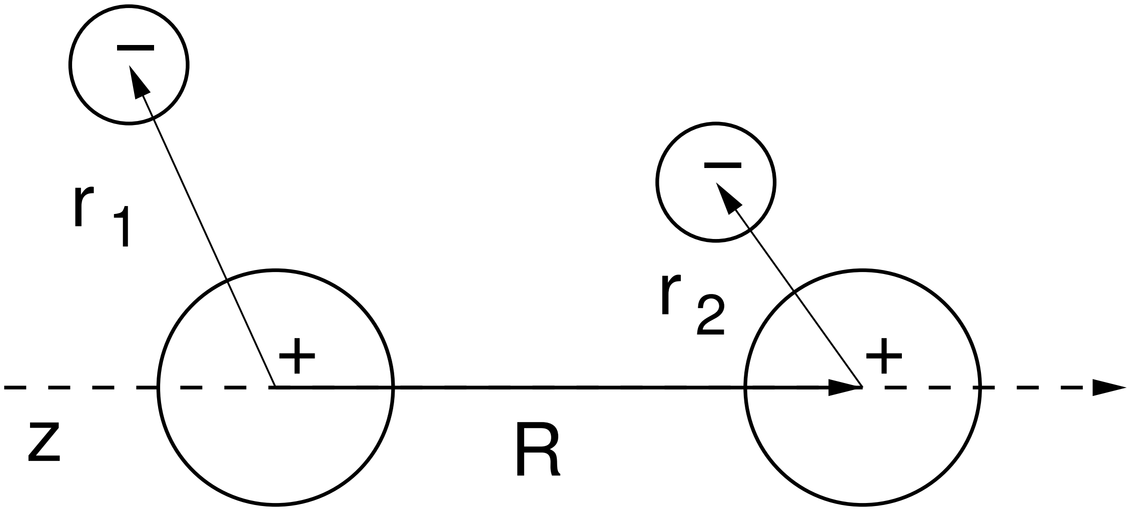

Figure A.1: Coordinate system for calculating exchange energy.

with respect to spatial coordinates:

$$|\psi_T\rangle = \frac{1}{\sqrt{2}}\left[\phi(r_1)\phi(r_2) - \phi\left(\left|\vec{R}-\vec{r_1}\right|\right)\phi\left(\left|\vec{R}+\vec{r_2}\right|\right)\right]. \tag{A.2}$$

Any trial wave function gives an energy higher than the true ground state energy. This energy, E_T, is given by

$$\begin{aligned} E_T &= \frac{\left\langle \psi_T \left| \hat{H} \right| \psi_T \right\rangle}{\langle \psi_T \mid \psi_T \rangle}, & \text{(A.3)} \\ E_T &= \left\langle \psi_T \left| -\frac{\hbar^2}{2m_e}\nabla^2_{r_1} - \frac{\hbar^2}{2m_e}\nabla^2_{r_2} - E_H\left(\frac{a_0}{r_1}+\frac{a_0}{r_2}\right)\right| \psi_T \right\rangle \langle \psi_T \mid \psi_T \rangle^{-1} \\ &+ E_h \left\langle \psi_T \left| \frac{a_0}{\left|\vec{R}+\vec{r_2}-\vec{r_1}\right|} - \frac{a_0}{\left|\vec{R}-\vec{r_1}\right|} - \frac{a_0}{\left|\vec{R}+\vec{r_2}\right|} \right| \psi_T \right\rangle \langle \psi_T \mid \psi_T \rangle^{-1} \\ &+ E_h \frac{a_0}{R}, & \text{(A.4)} \end{aligned}$$

$$E_T = \frac{A}{1-I^2} + E_h\left(\frac{C-B}{1-I^2} + \frac{a_0}{R}\right). \tag{A.5}$$

For convenience in evaluating the integrals, we group them differently than in section

2.2.2. There are four quantities we need to evaluate:

$$
\begin{aligned}
1 - I^2 &= \langle \psi_T \mid \psi_T \rangle \,, && \text{(A.6)}\\
A &= \left\langle \psi_T \left| -\frac{\hbar^2}{2m_e}\nabla^2_{r_1} - \frac{\hbar^2}{2m_e}\nabla^2_{r_2} - E_h\left(\frac{a_0}{r_1} + \frac{a_0}{r_2}\right) \right| \psi_T \right\rangle , && \text{(A.7)}\\
B &= \left\langle \psi_T \left| \frac{a_0}{\left|\vec{R} - \vec{r_1}\right|} + \frac{a_0}{\left|\vec{R} + \vec{r_2}\right|} \right| \psi_T \right\rangle , && \text{(A.8)}\\
C &= \left\langle \psi_T \left| \frac{a_0}{\left|\vec{R} + \vec{r_2} - \vec{r_1}\right|} \right| \psi_T \right\rangle . && \text{(A.9)}
\end{aligned}
$$

We tackle these in order. The details of evaluating the integrals are covered thoroughly in Slater (1963) [2].

The first integral is

$$
\begin{aligned}
\langle \psi_T \mid \psi_T \rangle &= \frac{1}{2}\int\int \phi^2(r_1)\phi^2(r_2)\, dV_1\, dV_2\\
&+ \frac{1}{2}\int\int \phi^2\left(\left|\vec{R} - \vec{r_1}\right|\right)\phi^2\left(\left|\vec{R} + \vec{r_2}\right|\right)\, dV_1\, dV_2\\
&- \int\int \phi(r_1)\phi\left(\left|\vec{R} - \vec{r_1}\right|\right)\phi(r_2)\phi\left(\left|\vec{R} + \vec{r_2}\right|\right)\, dV_1\, dV_2 \qquad \text{(A.10)}
\end{aligned}
$$

$$
\begin{aligned}
\langle \psi_T \mid \psi_T \rangle &= \frac{1}{2}\int \phi^2(r_1)\, dV_1 \int \phi^2(r_2)\, dV_2\\
&+ \frac{1}{2}\int \phi^2\left(\left|\vec{R} - \vec{r_1}\right|\right)\, dV_1 \int \phi^2\left(\left|\vec{R} + \vec{r_2}\right|\right)\, dV_2\\
&- \int \phi(r_1)\phi\left(\left|\vec{R} - \vec{r_1}\right|\right)\, dV_1 \int \phi(r_2)\phi\left(\left|\vec{R} + \vec{r_2}\right|\right)\, dV_2. \qquad \text{(A.11)}
\end{aligned}
$$

The first two terms of $\langle \psi_T \mid \psi_T \rangle$ are just normalized probability distributions integrated over all space. The third term is square of the *overlap integral*, I:

$$
\begin{aligned}
I &= \int \phi(r_1)\phi\left(\left|\vec{R} - \vec{r_1}\right|\right)\, dV_1 = \int \phi(r_2)\phi\left(\left|\vec{R} + \vec{r_2}\right|\right)\, dV_2\\
&= 2\pi A^2 \int_0^\infty \int_0^\pi \exp\left(-\frac{r}{a_0}\right) \exp\left(-\left[\frac{R^2 - 2Rr\cos\theta + r^2}{a_0}\right]^{1/2}\right) r^2 \sin\theta\, d\theta\, dr
\end{aligned}
$$

$$= \left(1+\frac{R}{a_0}+\frac{1}{3}\frac{R^2}{a_0^2}\right)e^{-\frac{R}{a_0}}. \qquad (A.12)$$

The final result is $\langle\psi_T \mid \psi_T\rangle = 1 - I^2$.

The second integral is

$$\begin{aligned} A &= \left\langle \psi_T \left| -\frac{\hbar^2}{2m_e}\nabla^2_{r_1} - \frac{\hbar^2}{2m_e}\nabla^2_{r_2} - E_h\left(\frac{a_0}{r_1}+\frac{a_0}{r_2}\right)\right| \psi_T \right\rangle \\ &= \left\langle \psi_T \left| \hat{H}_1 + \hat{H}_2 \right| \psi_T \right\rangle \qquad (A.13) \end{aligned}$$

where $\hat{H}_1, \hat{H}_2$ are the Hamiltonians of isolated hydrogen atoms, equal to $\frac{1}{2}E_h$ when operating on the appropriate wave function. The integral becomes

$$\begin{aligned} A &= \frac{1}{2}\int\int \phi(r_1)\phi(r_2)\left(\hat{H}_1+\hat{H}_2\right)\phi(r_2)\phi(r_1)\,dV_1\,dV_2 \\ &+ \frac{1}{2}\int\int \phi\left(\left|\vec{R}-\vec{r_1}\right|\right)\phi\left(\left|\vec{R}+\vec{r_2}\right|\right)\left(\hat{H}_1+\hat{H}_2\right)\phi\left(\left|\vec{R}+\vec{r_2}\right|\right)\phi\left(\left|\vec{R}-\vec{r_1}\right|\right)\,dV_1\,dV_2 \\ &- \int\int \phi(r_1)\phi(r_2)\left(\hat{H}_1+\hat{H}_2\right)\phi\left(\left|\vec{R}-\vec{r_1}\right|\right)\phi\left(\left|\vec{R}+\vec{r_2}\right|\right)\,dV_1\,dV_2 \qquad (A.14) \end{aligned}$$

$$\begin{aligned} A &= \frac{1}{2}E_h\int \phi^2(r_1)\,dV_1 \int \phi^2(r_2)\,dV_2 \\ &+ \frac{1}{2}E_h\int \phi^2\left(\left|\vec{R}-\vec{r_1}\right|\right)\,dV_1 \int \phi^2\left(\left|\vec{R}+\vec{r_2}\right|\right)\,dV_2 \\ &- E_h\int \phi(r_1)\phi\left(\left|\vec{R}-\vec{r_1}\right|\right)\,dV_1 \int \phi(r_2)\phi\left(\left|\vec{R}+\vec{r_2}\right|\right)\,dV_2 \qquad (A.15) \end{aligned}$$

$$A = E_h\left(1-I^2\right). \qquad (A.16)$$

The third integral is

$$\begin{aligned} B &= \left\langle \psi_T \left| \frac{a_0}{\left|\vec{R}-\vec{r_1}\right|} + \frac{a_0}{\left|\vec{R}+\vec{r_2}\right|} \right| \psi_T \right\rangle \\ &= \frac{1}{2}\int\int \phi^2(r_1)\left(\frac{a_0}{\left|\vec{R}-\vec{r_1}\right|}+\frac{a_0}{\left|\vec{R}+\vec{r_2}\right|}\right)\phi^2(r_2)\,dV_1\,dV_2 \end{aligned}$$

$$
\begin{aligned}
&+ \quad \frac{1}{2}\int\int \phi^2\left(\left|\vec{R}-\vec{r_1}\right|\right)\left(\frac{a_0}{\left|\vec{R}-\vec{r_1}\right|}+\frac{a_0}{\left|\vec{R}+\vec{r_2}\right|}\right)\phi^2\left(\left|\vec{R}+\vec{r_2}\right|\right) dV_1\, dV_2\\
&- \quad \int\int \phi(r_1)\phi\left(\left|\vec{R}-\vec{r_1}\right|\right)\left(\frac{a_0}{\left|\vec{R}-\vec{r_1}\right|}+\frac{a_0}{\left|\vec{R}+\vec{r_2}\right|}\right)\phi(r_2)\phi\left(\left|\vec{R}+\vec{r_2}\right|\right) dV_1\, dV_2
\end{aligned}
\tag{A.17}
$$

The integrals separate into

$$
\begin{aligned}
B \quad = \quad & \frac{1}{2}\int \phi^2(r_1)\frac{a_0}{\left|\vec{R}-\vec{r_1}\right|}\, dV_1 + \frac{1}{2}\int \phi^2(r_2)\frac{a_0}{\left|\vec{R}+\vec{r_2}\right|}\, dV_2\\
+ \quad & \frac{1}{2}\int \phi^2\left(\left|\vec{R}-\vec{r_1}\right|\right)\frac{a_0}{\left|\vec{R}-\vec{r_1}\right|}\, dV_1 + \frac{1}{2}\int \phi^2\left(\left|\vec{R}+\vec{r_2}\right|\right)\frac{a_0}{\left|\vec{R}+\vec{r_2}\right|}\, dV_2\\
- \quad & \int \phi(r_1)\phi\left(\left|\vec{R}-\vec{r_1}\right|\right)\frac{a_0}{\left|\vec{R}-\vec{r_1}\right|}\, dV_1 + \int \phi(r_2)\phi\left(\left|\vec{R}+\vec{r_2}\right|\right)\frac{a_0}{\left|\vec{R}+\vec{r_2}\right|}\, dV_2.
\end{aligned}
\tag{A.18}
$$

Inspection reveals that the first term is identical to the second, the third term to the fourth, and the fifth term to the sixth. They can be rewritten as

$$
\begin{aligned}
B \quad = \quad & 2\pi A^2\int_0^{\infty}\int_0^{\pi} e^{-2\frac{r}{a_0}}\frac{a_0}{\left(R^2-2Rr\cos\theta+r^2\right)^{1/2}} r^2\sin\theta\, d\theta\, dr\\
+ \quad & 2\pi A^2\int_0^{\infty}\int_0^{\pi} e^{-2\frac{r}{a_0}}\frac{a_0}{r} r^2\sin\theta\, d\theta\, dr,\\
- \quad & 4\pi A^2\int_0^{\infty}\int_0^{\pi} e^{-\frac{r}{a_0}}\exp\left(\frac{\left(R^2-2Rr\cos\theta+r^2\right)^{1/2}}{a_0}\right)\frac{a_0}{r} r^2\sin\theta\, d\theta\, dr
\end{aligned}
\tag{A.19}
$$

$$
\begin{aligned}
B \quad = \quad & \frac{a_0}{R}-\left(1+\frac{a_0}{R}\right)e^{-2\frac{R}{a_0}}\\
+ \quad & 1\\
+ \quad & \left(1+\frac{R}{a_0}\right)e^{-\frac{R}{a_0}}.
\end{aligned}
\tag{A.20}
$$

The fourth integral is

$$
C \quad = \quad \left\langle \psi_T \left| \frac{a_0}{\left|\vec{R}+\vec{r_2}-\vec{r_1}\right|} \right| \psi_T \right\rangle
$$

$$\begin{aligned}
&= \frac{1}{2}\int\int \phi^2(r_1)\phi^2(r_2)\frac{a_0}{\left|\vec{R}+\vec{r_2}-\vec{r_1}\right|}\,dV_1\,dV_2 \\
&+ \frac{1}{2}\int\int \phi^2\left(\left|\vec{R}-\vec{r_1}\right|\right)\phi^2\left(\left|\vec{R}+\vec{r_2}\right|\right)\frac{a_0}{\left|\vec{R}+\vec{r_2}-\vec{r_1}\right|}\,dV_1\,dV_2 \\
&- \int\int \phi(r_1)\phi\left(\left|\vec{R}-\vec{r_1}\right|\right)\phi(r_2)\phi\left(\left|\vec{R}+\vec{r_2}\right|\right)\frac{a_0}{\left|\vec{R}+\vec{r_2}-\vec{r_1}\right|}\,dV_1\,dV_2. \qquad \text{(A.21)}
\end{aligned}$$

Unlike the others evaluated so far these integrals do not separate, and are most easily solved in spheroidal coordinates [2]. Inspection reveals that the first term is identical to the second. They evaluate to:

$$\begin{aligned}
C &= \frac{a_0}{R} - e^{-2\frac{R}{a_0}}\left(\frac{a_0}{R}+\frac{11}{8}+\frac{3}{4}\frac{R}{a_0}+\frac{1}{6}\frac{R^2}{a_0^2}\right) \\
&+ \frac{1}{5}\left(\begin{array}{l} -e^{-2\frac{R}{a_0}}\left[-\frac{25}{8}+\frac{23}{4}\frac{R}{a_0}+3\frac{R^2}{a_0^2}+\frac{1}{3}R^3a_0^3\right]+ \\ 6\frac{R}{a_0}\left[I^2\left(\gamma+\log\frac{R}{a_0}\right)+I'^2\mathrm{Ei}\left(-4\frac{R}{a_0}\right)-2II'\mathrm{Ei}\left(-2\frac{R}{a_0}\right)\right] \end{array}\right) \\
\text{where } I &= \left(1+\frac{R}{a_0}+\frac{1}{3}\frac{R^2}{a_0^2}\right)e^{-\frac{R}{a_0}}, \\
I' &= \left(1-\frac{R}{a_0}+\frac{1}{3}\frac{R^2}{a_0^2}\right)e^{\frac{R}{a_0}}, \\
\mathrm{Ei}(-x) &= -\int_x^\infty \frac{1}{t}\left(1-e^{-t}\right)\,dt, \\
\gamma &= 0.57722\ldots \qquad \text{Euler's constant.} \qquad \text{(A.22)}
\end{aligned}$$

Now that the four integrals are evaluated we can return to equation A.5:

$$\begin{aligned}
E_T &= \frac{A}{1-I^2}+E_h\left(\frac{C-B}{1-I^2}+\frac{a_0}{R}\right) \\
&= E_h\left(1+\frac{a_0}{R}+\frac{C-B}{1-I^2}\right) \qquad \text{(A.23)}
\end{aligned}$$

Since E_h is independent of R, we subtract it from the energy so that it goes to zero at infinite separation. E_T is plotted in figure A.2.

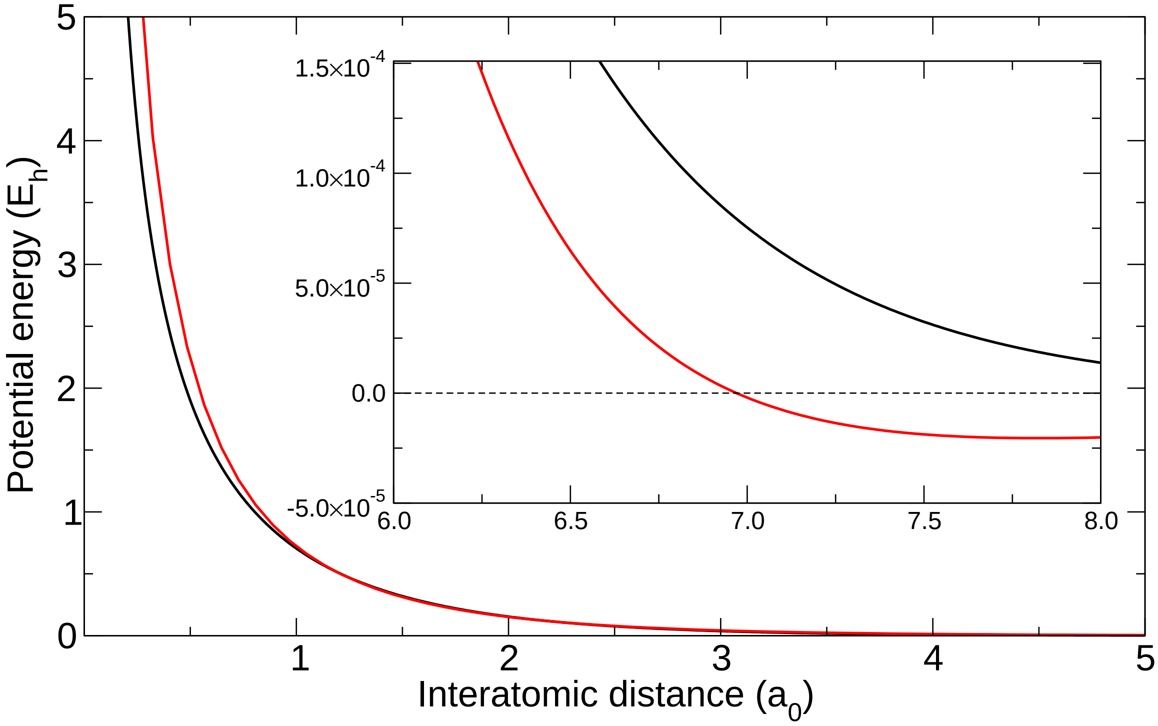

Figure A.2: Exchange repulsion energy E_T. Black: Result of the Heitler-London calculation. Red: Fit to $A\exp(-kR)$, where $A = 1.725\,E_h$ and $k = 0.870\,a_0^{-1}$. Inset: Comparison of Heitler-London energy (black) to Lennard-Jones potential (red) for the hydrogen triplet, $\sigma = 6.97\,a_0$, $\epsilon = 2.047 \times 10^{-5}\,E_h$ [3].

Taylor expansion about $R = 0$ gives

$$E_T \approx E_h \left(\frac{a_0}{R} + \frac{1}{2} - 2\frac{R}{a_0} \right), \tag{A.24}$$

which is accurate within 2 % up to $R = 0.1\,a_0$ but rapidly becomes useless thereafter. As shown in figure A.2, a fit to

$$E_T \approx A e^{-k\frac{R}{a_0}} \tag{A.25}$$

works tolerably well.

The Heitler-London method fails at long-range; E_T approaches zero at infinite separation, instead of recovering the van der Waals R^{-6} attraction. The hydrogen triplet actually has a potential minimum at about $7.8\,a_0$ [3].

A.1 Bibliography

[1] B. H. Brandsen and C. J. Joachain. *Physics of atoms and molecules.* Prentice-Hall, 2003.

[2] J. C. Slater. *Quantum theory of molecules and solids.* McGraw-Hill Book Company, 1963.

[3] W. Stwalley and L. Nosanow. Possible "new" quantum systems. *Physical Review Letters*, 36:910–913, 1976.

Appendix B

Reflected intensity profile: ray optics

Our first attempt to describe the reflected intensity profile used ray optics in the paraxial approximation.

A cone of light rays of uniform intensity I_0 has its focus at z, and reflects from a plane interface located at z_i. The reflected light enters the objective lens, of focal length f_1, then through the tube lens of focal length f_2, and then is screened by the pinhole of diameter D located at the focal point of the tube lens, as illustrated in figure B.1.

Light that passes through the pinhole must first pass through the image of the pinhole located at the focal point of the objective. A trivial calculation shows that no matter how far apart the lenses, the image of the pinhole is always at the at the focus of the objective (hence the name *confocal microscope*), and that the diameter of the pinhole image is given by

$$D_i = \frac{f_1}{f_2} D, \tag{B.1}$$

as figure B.2 makes clear.

The reflected light forms a cone of light rays with its focus at z'. By the law of

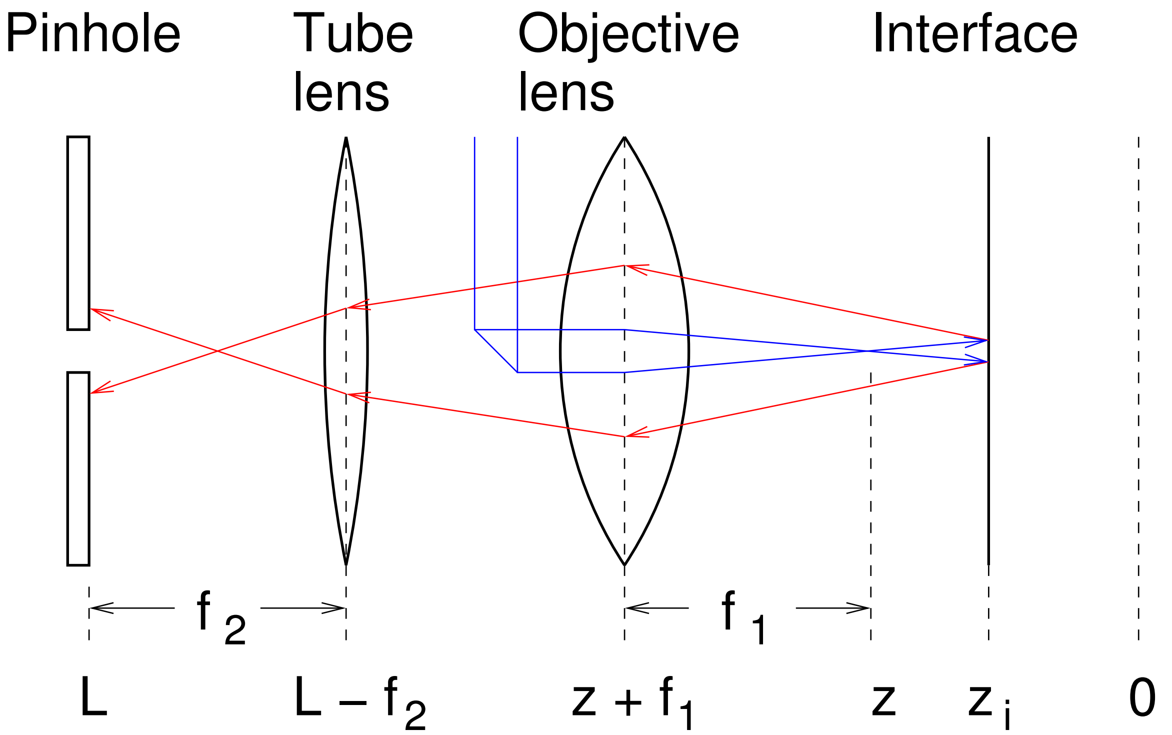

Figure B.1: Coordinate system for reflected intensity profile.

reflection,

$$z - z_i = z_i - z', \tag{B.2}$$

and so the distance of the reflected focus from the virtual pinhole is $2(z - z_i)$. Assuming constant intensity, the reflected power P_r passing through the virtual pinhole is

$$P_r = I_0 \pi \left(\frac{f_1}{f_2} \frac{D}{2} \right)^2 . \tag{B.3}$$

The total incident power in the cone is given by

$$P_0 = I_0 \pi R^2 \tag{B.4}$$

where R is the radius of the reflected cone at the focal point. In the paraxial approximation, $R = 2(z - z_i)\theta$, where θ is the half-angle of the cone.

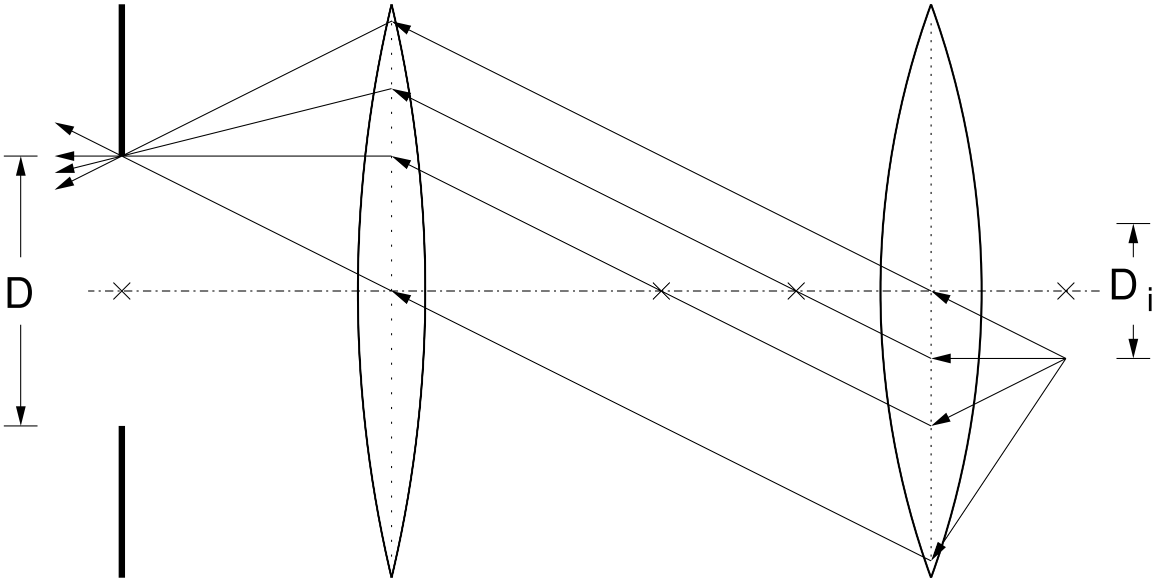

Figure B.2: Ray diagram of pinhole and pinhole image. Parallel lines, in the paraxial approximation, are always brought to the focal point, and an object at one focus has its image at the other.

The reflected intensity profile in the ray optics model is therefore

$$f(z) = \begin{cases} \frac{f_1^2}{f_2^2}\frac{D^2}{8\theta^2(z-z_i)^2} & |z-z_i| \; > \; \frac{1}{\theta 2\sqrt{2}}\frac{f_1}{f_2}D \\ 1 & |z-z_i| \; \leq \; \frac{1}{\theta 2\sqrt{2}}\frac{f_1}{f_2}D \end{cases} \tag{B.5}$$

These flat-topped peaks were found too crude to fit the data, though they did show that the reflected intensity is indeed a maximum when the focus is at the interface. The Gaussian beam model derived in section 4.2.5, equation 4.35, is

$$f(z) = \left[1 - \exp\left(-\frac{D^2}{2w^2}\left(\frac{f_1}{f_2}\right)^2 \frac{R^2}{4(z-z_i)^2 + R^2}\right)\right]. \tag{B.6}$$

In the limit that the beam waist goes to zero this reduces to

$$f(z) = 1 - \exp\left(-\frac{D^2}{2\theta^2}\frac{f_1^2}{f_2^2}\frac{1}{4(z-z_i)^2}\right). \tag{B.7}$$

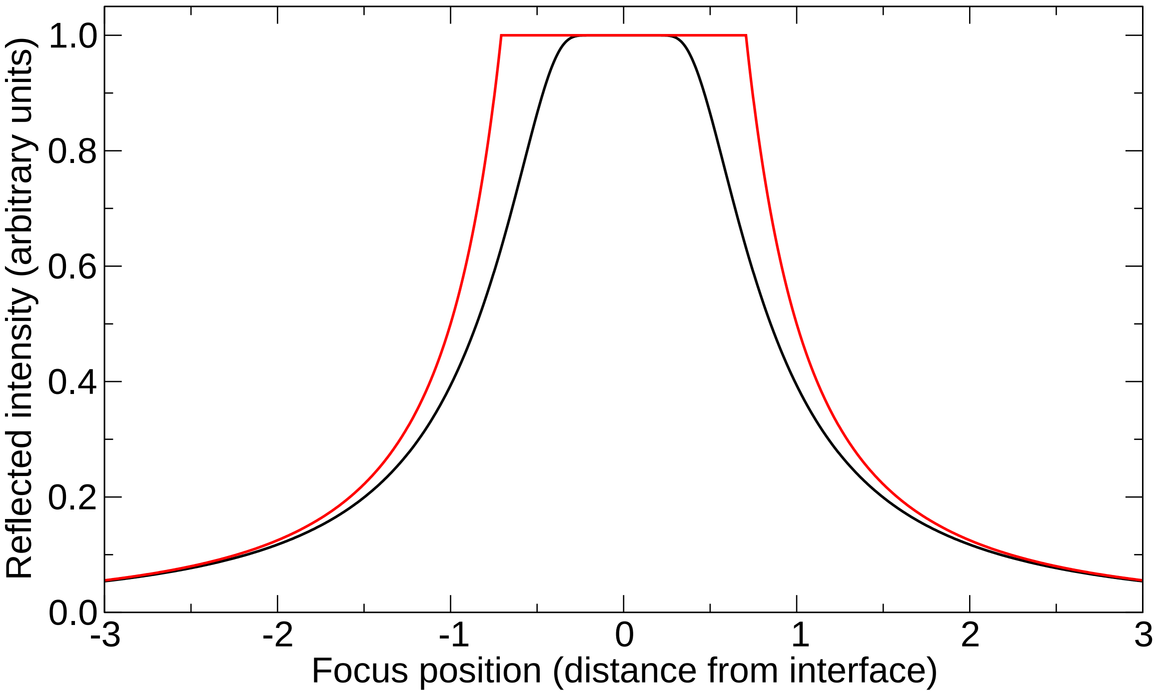

Figure B.3: The ray optics profile (red) compared with the Gaussian beam profile (black). The horizontal axis shows the distance of the focus from the interface, in units of the virtual pinhole radius, $\frac{1}{2}\frac{f_1}{f_2}D$.

Setting the pinhole diameter to be very large (several hundred microns) with respect to the beam waist will show flat-topped peaks, difficult to locate precisely. But equation B.6 only reduces to equation B.5 when far from the interface. The two profiles are plotted together in figure B.3; the ray optics model fails badly near the interface, which is what we desire to model.

Appendix C

Solving the paraxial Helmholtz equation

We demonstrate that a Gaussian beam is a solution to the paraxial Helmholtz equation

$$\left(\frac{1}{\rho}\frac{\partial}{\partial\rho} + \frac{\partial^2}{\partial\rho^2}\right) E(\rho, z)e^{ikz} = 2ik\frac{\partial}{\partial z}E(\rho, z)e^{ikz}, \tag{C.1}$$

where ρ, z are the radial and axial coordinates, $E(\rho, z)$ is a complex-valued scalar representing the magnitude of the electric field, and k is the wave number.

We write the electric field as a scalar because in the paraxial approximation the wave vector is considered to point along the z axis. The direction of the electric field is therefore already assumed to be perpendicular to the z axis. In this case, for simplicity, we assume that the electric field points in the radial ($\hat{\rho}$) direction and is radially symmetric. Real lasers need not show radial symmetry. The symmetry of a real laser depends on the shapes that define its resonant cavity [1–5].

The intensity of a Gaussian beam is given in section 4.2.2,

$$\begin{aligned} I &= I_0 \left(\frac{w_0}{w(z)}\right)^2 \exp\left(-2\frac{\rho^2}{w^2(z)}\right), && \text{(C.2)} \\ w(z) &= w_0\sqrt{1+\left(\frac{z}{z_R}\right)^2}, && \text{(C.3)} \end{aligned}$$

where w_0 is the size of the beam waist, $z_R = \pi w_0^2/\lambda$ is the Rayleigh range of the beam, and I_0 is the maximum intensity (at the origin, for simplicity).

The electric field which produces this intensity is given by [1, 3, 4]

$$\begin{aligned} E(\rho, z) &= E_0\frac{w_0}{w(z)} \exp\left(-\frac{\rho^2}{w^2(z)}\right) \exp\left(-ik\frac{\rho^2}{2R(z)} - i\zeta(z)\right), && \text{(C.4)} \\ R(z) &= z\left[1+\left(\frac{z_R}{z}\right)^2\right], && \text{(C.5)} \\ \zeta(z) &= \tan^{-1}\frac{z}{z_R}, && \text{(C.6)} \end{aligned}$$

and it is simple to show that $|E(\rho, z)|^2$ gives the intensity given in equation C.2.

This equation looks quite complex and it is not easy to see, from first principles, how it is derived. It is written in this way because $R(z)$, $w(z)$, and $\zeta(z)$ are parameters that help to visualize the beam in terms of a plane wave propagating along the z axis.

$\zeta(z)$ is the *Gouy phase shift*, surprisingly difficult to spell, which expresses how the phase of the beam differs from that of a plane wave as a function of z. $R(z)$ is the radius of curvature of the wavefronts of the beam; it makes the beam approximate a plane wave at the waist and a spherical wave far from the waist. $w(z)$ expresses the falling-off of intensity with distance from the beam axis (figure C.1.)

Equation C.4 is greatly simplified by the substitution of the complex radius

$$q \equiv z + iz_R, \tag{C.7}$$

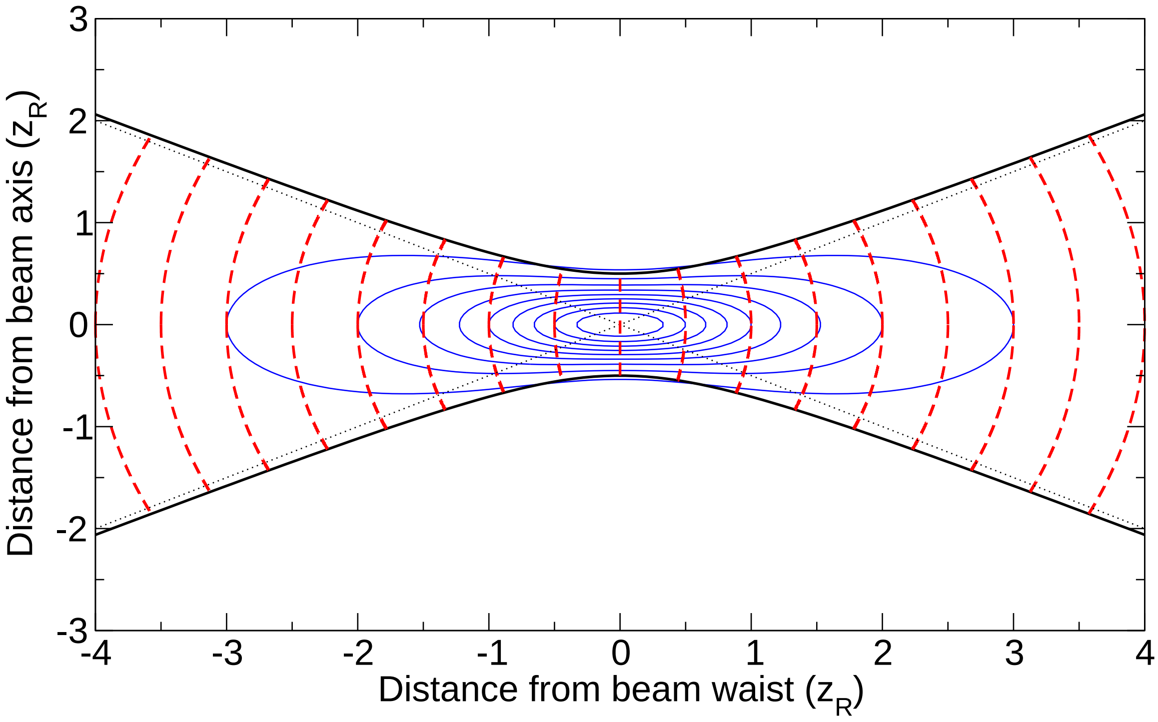

Figure C.1: Gaussian beam (waist $w_0 = z_R/2$). Blue lines: intensity contour plot, contour interval 10 % of maximum intensity (see equation C.2). Solid black lines: Beam envelope, defined as $I(z)e^{-2}$ (see equation C.3). Dotted black lines: cone of light rays which approximates beam. Red lines: wavefronts (see equation C.5).

discussed in section 4.2.5. Equation C.4 becomes

$$E(\rho, q) = E_0 \frac{q_0}{q} \exp\left(-ik\frac{\rho^2}{2q}\right), \tag{C.8}$$

with $q_0 = z_R$. Equation C.8 is much easier to manipulate than equation C.4, but much harder to interpret physically. Equation C.8 was derived first, by analogy with the time-dependent Schrödinger equation, and the interpretation of q in terms of a modified plane wave worked out afterward [5]. Inserting equation C.8 into equation C.1 yields

$$\begin{aligned} -\frac{ik}{q}E(\rho,q) - \left(\frac{k^2\rho^2}{q^2} + \frac{ik}{q}\right)E(\rho,q) &= 2ik\left(-\frac{1}{q} + \frac{ik\rho^2}{2q^2}\right)E(\rho,q) \\ \frac{k^2\rho^2}{q^2} - 2\frac{ik}{q} &= \frac{k^2\rho^2}{q^2} - 2\frac{ik}{q} \end{aligned} \tag{C.9}$$

Like the Schrödinger equation, there are many solutions to the paraxial Helmholtz equation. The Gaussian beam is the fundamental transverse mode, and is designated TEM_{00} [1–5].

C.1 Bibliography

[1] A. E. Siegman. *Lasers.* University Science Books, 1986.

[2] William T. Silvfast. *Laser fundamentals.* Cambridge University Press, 2004.

[3] W. J Firth and R. G. Harrison, editors. *Lasers: physics, systems and techniques.* SUSSP Publications, 1982.

[4] A. Gerrard and J. M. Bruch. *Introduction to matrix methods in optics.* Wiley Interscience, 1975.

[5] H. Kogelnik and T. Li. Laser beams and resonators. *Applied Optics*, 5:1150, 1966.

Appendix D

Derivation of the Clausius-Mossotti relation

The Clausius-Mossotti relation is also known as the Lorentz-Lorenz relation or Maxwell relation, depending on the context. It is derived by considering an atom of a fluid to reside in a spherical hole in a uniformly polarized linear dielectric consisting of the other atoms in the fluid [1].

An external field E polarizes a fluid in the z direction. The fluid has a dielectric constant ϵ and is of number density ρ. The atoms of the fluid have a polarizability α.

The field E_h inside a spherical hole in a uniformly polarized dielectric is

$$E_h = E + \frac{P}{3\epsilon_0}, \tag{D.1}$$

where P is the dipole moment per unit volume. P is given by

$$P = (\epsilon - \epsilon_0)\, E, \tag{D.2}$$

due to the linear response of the dielectric. Because the dielectric is made up of atoms of polarizability α, this P must also be

$$P = \rho \alpha \epsilon_0 E_h. \tag{D.3}$$

Eliminating E_h and P (E cancels) yields

$$\frac{\frac{\epsilon}{\epsilon_0} - 1}{\frac{\epsilon}{\epsilon_0} + 2} = \frac{1}{3} \alpha \rho. \tag{D.4}$$

Recalling that $\epsilon / \epsilon_0 = n^2$, if the permeability of the dielectric is the same as vacuum, we get the Clausius-Mossotti relation

$$\frac{n^2 - 1}{n^2 + 2} = \frac{1}{3} \alpha \rho. \tag{D.5}$$

D.1 Bibliography

[1] R. Feynman, R. Leighton, and M. Sands. *The Feynman lectures on physics*. Addison-Wesley, 1965.

Appendix E

Confocal data for water at 300 K

Our first confocal measurements of fluid volume were carried out on water at 300 K, as described in reference [1]. The results are plotted in figure E.1 and E.2. These were our first results, intended to demonstrate the viability of the technique, and not all of the procedures described in chapter 4 were yet worked out. These data are not as accurate or precise as the data collected for argon (section 5.1.1). However, they did enable us to refine the technique.

In this experiment, we used a piston-cylinder DAC, identical to that described in section 4.1, with a stainless steel gasket indented to about 150 μm, and drilled a hole of diameter 330 μm. We loaded the cell with high-purity water as described in section 4.1.3 and a small ruby chip for pressure measurement as described in section 4.1.5. We maintained the cell at 300 K using a 100 W mica band heater as described in section 4.1.6. We then collected the reflected intensity profile as described in section 4.2.1.

However, in this experiment volume was calculated by multiplying the measured area, optical thicknes, and calibrated refractive index, without doing any smoothing. We did not calculate mole number; instead we multiplied published equations of state for water, ice VI, and ice VI by least squares fit of the published fluid EOS [2] to our

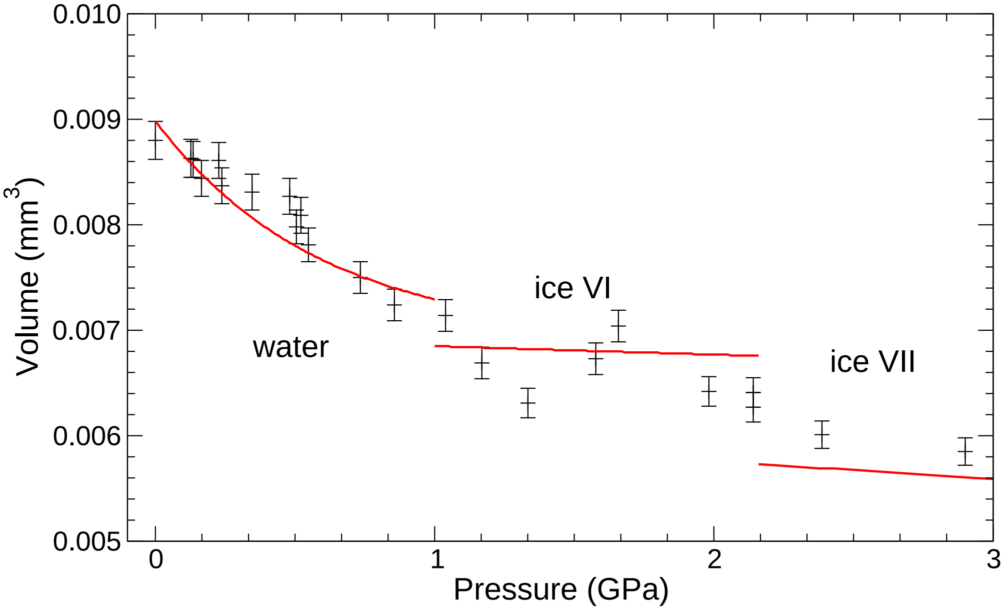

Figure E.1: Equation of state for water at 300 K [1]. Red lines: equations of state for water [2], ice VI [3], and ice VII [4].

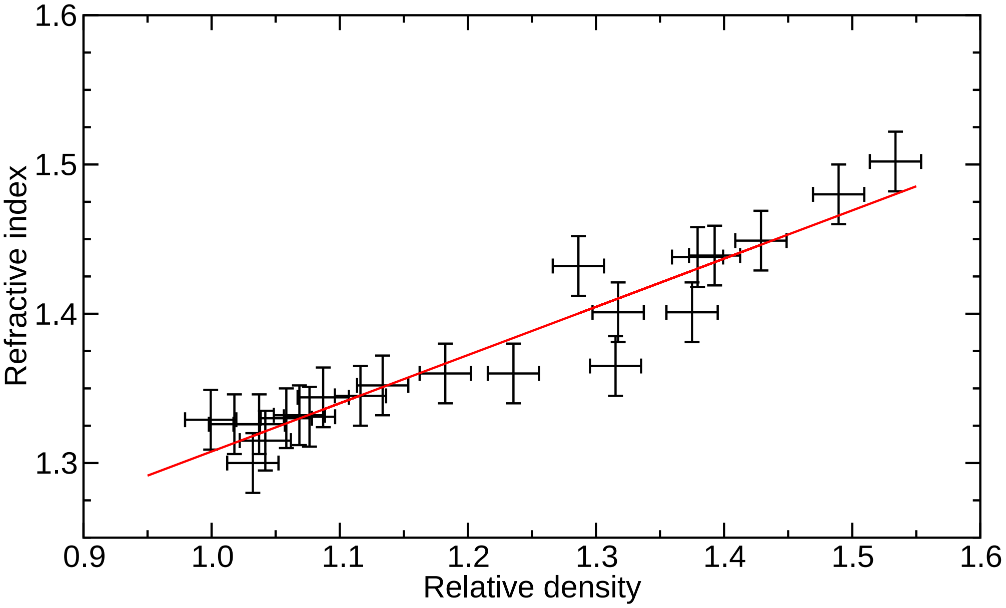

Figure E.2: Index of refraction as a function of density for water at 300 K [1]. “Relative density” is scaled by the volume of the first measured point. Red: linear fit to our data.

Reference	Slope	Intercept
Yadav et al. [5]	0.322	1.332
Hanna and McCluskey [1]	0.34(2)	1.308(7)

Table E.1: Linear fit of refractive index toas a function of density for water at 300 K.

data, using the volume at zero pressure, $V_0 = 9.06(5) \times 10^{-3}$ mm^3, as a fitting parameter.

Because for many substances refractive index is approximately a linear function of density, we fitted it to a straight line. The results are shown in table E.1.

E.1 Bibliography

[1] G. J. Hanna and M. D. McCluskey. Measuring the volume of a fluid in a diamond anvil cell using a confocal microscope. *Applied Optics*, 48:1758–1763, 2009.

[2] M. Choukron and O. Grasset. Thermodynamic model for water and high-pressure ices up to 2 2GPa and down to the metastable domain. *Journal of Chemical Physics*, 111:124506–1–124506–9, 2007.

[3] E. Noya, C. Menduina, J. Aragones, and C. Vega. Equation of state, thermal expansion coefficient, and isothermal compressibility for ices Ih, II,III,V and VI as obtained from computer simulation. *Journal of Physical Chemistry C*, 67:15877–15888, 2007.

[4] E. Wolanin, Ph. Pruzan, J. Chervin, B. Canny, and M. Gauthier. Equation of state of ice VI up to 106GPa. *Physical Review B*, 56:5781–5785, 1997.

[5] H. Yadav, D. Murty, S. Verma, K. Sinha, B. Gupta, and D. Chand. Measurement of refractive index of water under high dynamic pressures. *Journal of Applied Physics*, 44:2197–2200, 1973.

Appendix F

X-ray diffraction experiments

We assisted Kirill Zhuravlev in collecting powder X-ray diffraction data at Lawrence Berkely National Laboratory for doped zinc oxide crystals. The crystals were placed in a DAC with argon for a hydrostatic medium. A byproduct of the experiment was measurements of the molar volume of solid argon as a function of pressure, at ambient temperature (about 297 K). Only one or two measurements were taken at fluid argon pressures. Kirill Zhuravlev was kind enough to process the X-ray data into pressure-volume data for argon, which we present here with his permission (figure F.1).

We fit the data to a polynomial equation of state, chosen for ease of inversion and convenience of fitting:

$$P = a(\rho - b)^3, \tag{F.1}$$

with $a = 6.056(46) \times 10^5 \quad \mathrm{GPa\,mm^9\,mmol^{-9}}$ and $b = 0.0210(12)\,\mathrm{mmol\,mm^{-3}}$.

F.1 Bibliography

[1] M. Grimsditch, P. Loubeyre, and A. Polian. Brillouin scattering and three-body forces in argon at high pressure. *Physical Review B*, 33:7192–7200, 1986.

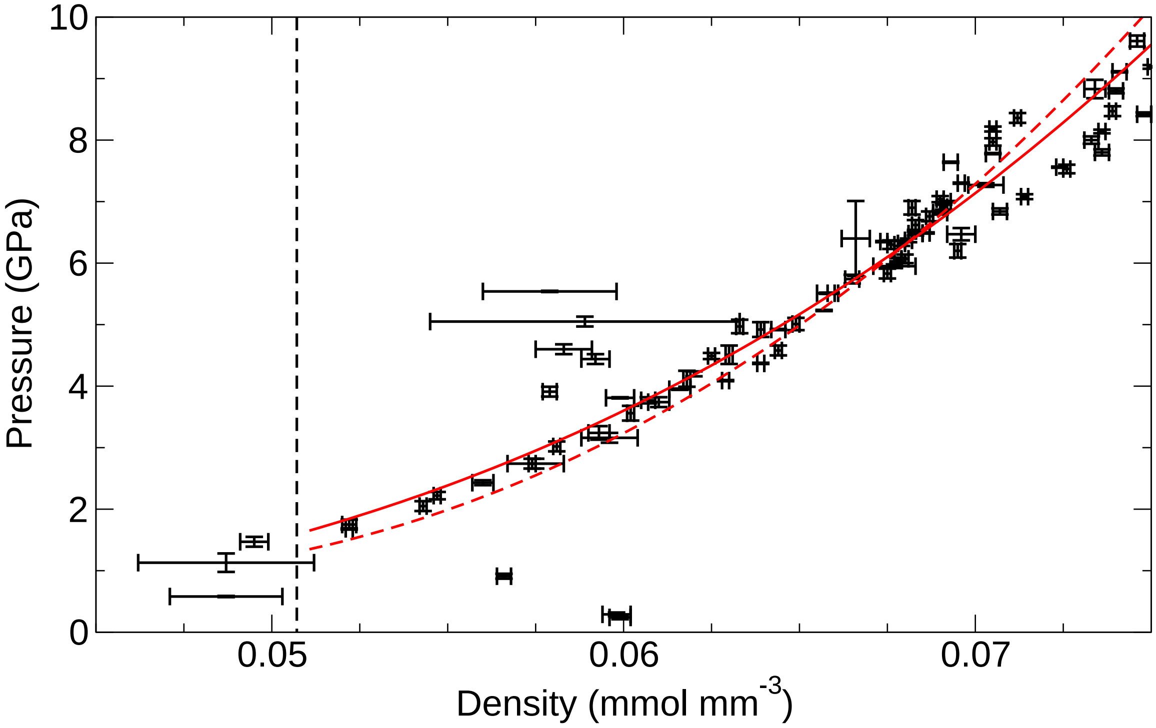

Figure F.1: Equation of state for solid argon. Solid line (red): our fit. Dashed line (red): equation of state from the literature [1]. Dashed line (black): boundary of solid phase. Our fit excludes points not in the solid phase, and the outliers between $0.055\,\mathrm{mmol\,mm^{-3}}$ and $0.060\,\mathrm{mmol\,mm^{-3}}$.

Appendix G

IR absorption of Ge:O

We measured the frequency of the IR absorption peak of interstitial oxygen in germanium at 10 K. Interstitial oxygen is predicted to be delocalized about an axis determined by two germanium atoms [1], and has IR modes near 860 cm^{-1} and 1270 cm^{-1}.

In this experiment we measured the mode near 860 cm^{-1}, using liquid helium to keep the temperature near 10 K. Pressure was determined by the frequency of the carbon dioxide and nitrogen IR absorption peaks according to the calibration by McCluskey and Zhuravlev [2]. The results are plotted in figure G.1.

G.1 Bibliography

[1] E. Artacho, F. Yndurain, B. Pajot, R. Ramirez, C. Herrero, L. Khirunenko, K. Itoh, and E. Haller. Interstitial oxygen in germanium and silicon. *Physical Review B*, 56:3820–3833, 1997.

[2] M. McCluskey and K. Zhuravlev. N_2 and CO_2 vibrational modes in solid nitrogen under pressure. *Journal of Chemical Physics*, 116:1607–1612, 2002.

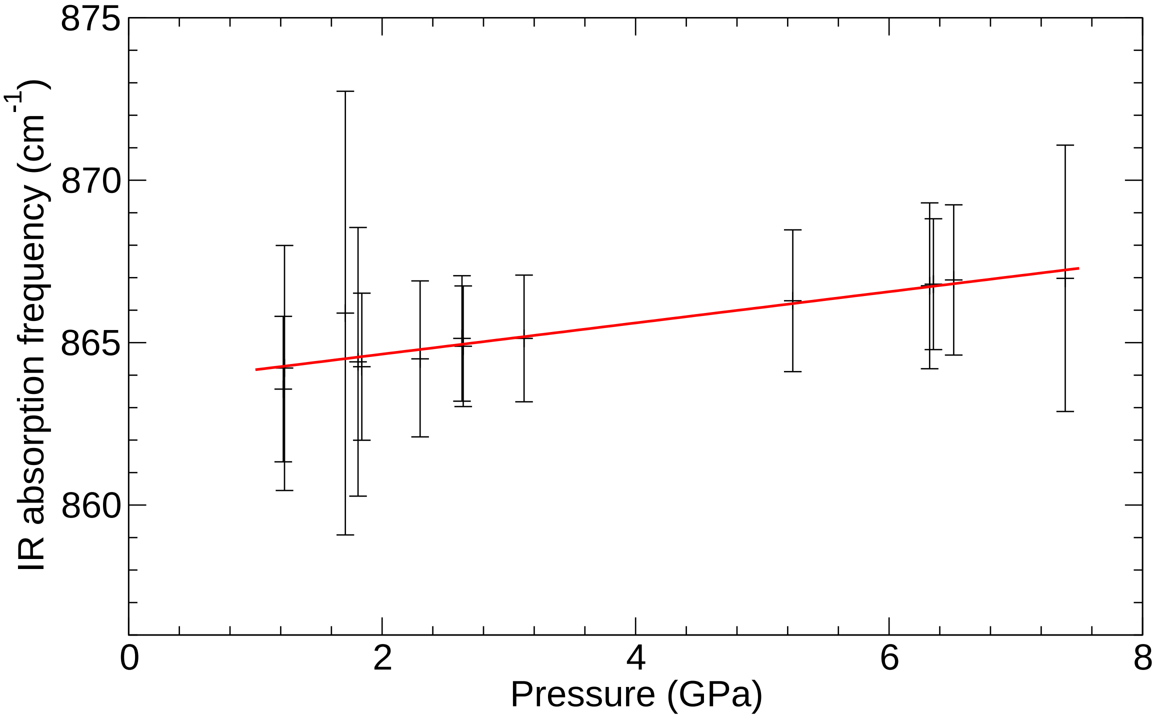

Figure G.1: IR absorption of Ge:O at 10 K. Red line: linear fit (slope = $0.48\,\mathrm{cm}^{-1}\,\mathrm{GPa}^{-1}$, intercept = $863.7\,\mathrm{cm}^{-1}$). The error bars are the peak widths.